國立臺灣大學理學院地質科學研究所

博士論文

Institute of Geosciences

College of Science

National Taiwan University

Doctor Thesis

臺灣-琉球間之隱沒-碰撞複和帶
隱沒板塊與弧前地幔之力學性質與結構

The Taiwan-Ryukyu subduction-collision complex: Mechanics and structure of the slab and the forearc mantle

周漢強

Han-Chiang Chou

指導教授：郭本垣 博士

洪淑蕙 博士

Advisor: Ban-Yuan Kuo, Ph.D.

Shu-Huei Hung, Ph.D.

中華民國 99 年 3 月

Mar, 2010

國立臺灣大學博士學位論文
口試委員會審定書

臺灣-琉球間之隱沒-碰撞複和帶
隱沒板塊與弧前地幔之力學性質與結構

The Taiwan-Ryukyu subduction-collision complex:
Mechanics and structure of the slab and the forearc mantle

本論文係周漢強君（D92224001）在國立臺灣大學地質科學所完成之博士學位論文，於民國九十九年一月二十六日承下列考試委員審查通過及口試及格，特此證明

口試委員：

_____（簽名）
（指導教授）

_____（簽名）
（指導教授）

_____　_____
_____　_____

誌謝

要感謝的人太多，那就感謝老天吧！

目　錄

圖　目　錄

中文摘要

頂著歐亞板塊的琉球海溝末端，也是菲律賓海板塊斜向隱沒進入歐亞板塊下方的地點，在台灣外海形成了複雜的隱沒—碰撞複和帶，迄今仍未被詳盡解釋的一個區域。我們結合了來自台灣與日本兩個地區的地震觀測網資料，以期闡明琉球隱沒板塊如何在這個隱沒—碰撞地區隱沒與變形。我們使用同時被兩個地震網所記錄到超過五千個以上的地震資料，並以最佳化的區域一維速度模型及二次差分法進行重新定位。外海的地震分布結果顯示，在隱沒板塊伸至 40 至 80 公里深處，有存在間隔約 15 至 20 公里寬的雙層地震帶。根據震源機制解的結果顯示，雙層地震帶是肇因於斜向聚合所導致的東西向壓縮。

精確定位後的地震分布也第一次呈現在深度 50 至 100 公里處，隱沒板塊水平方向褶皺的曲率大到與整個琉球海溝的曲率異號。這個異常的曲率加上震源機制解的結果，顯示隱沒板塊因為頂住歐亞岩石圈而變形，且這個變形很顯然並非完全彈性。我們針對此變形建立了一個模式，推導出一個不穩定的麥斯威爾黏彈性層，夾在黏滯性介質中的結果。這個不穩定性的構造其特徵波長約為 250 公里，這個結果符合褶曲的隱沒板塊其黏滯性約為周圍地幔物質的 100 倍大，且沿著海溝方向的表面彈性應變為 0.01；或是隱沒板塊其黏滯性約為周圍地幔物質的 1000 倍，則表面彈性應變可以大到 5%。

本研究中亦同時建構了琉球最西側隱沒的菲律賓海板塊以及臺灣東北部地底下的弧前地幔的三維地震層析影像，反演 V_P、V_S、和 V_P/V_S 的變化。藉由分析資料的變異量降低對模型變異間的取捨，可以幫助我們建立合適嚴謹程度的正則化，以避免對資料過度解釋或解釋不足。正則化參數的選擇是為了確保人為的 V_P/V_S 異常可以被壓制住。隱沒板塊的特徵為高 V_P、高 V_S 以及中等到低的 V_P/V_S。　值得注意的是在緊鄰隱沒板塊表面，深度約 30-80 公里處的地幔楔則為高 V_P/V_S 異常。過去曾被發現存在有高 V_P/V_S 通道連結隱沒板塊與島弧火山之間，因而被解釋作熔融的通道，但在本研究中並未發現。

我們將 V_S 和 V_P/V_S 轉換為溫度變化以及地幔中的蛇紋岩化。隱沒板塊的溫度比周圍地幔低約 200-400^{o}C，與隱沒帶理論模型的估計一致。在 50 公里深的地幔，其蛇紋岩化的程度達到約 15%，或含水量達 2%。我們將此蛇紋岩化的峰值，解釋為由於菲律賓海板塊隱沒，其表面之海洋地殼產生玄武岩—榴輝岩變質反應所釋放的水，與地幔反應所導致。由於本區域現有地震網相對於隱沒帶地震的分佈，存在有空間上的限制，因此限制了完整描述大部分地幔楔產生熔融的型態。層析影像反演的解析度測試則提供了對於解釋較佳解析區域的基本指引。

英文摘要

The termination of the Ryukyu trench against Eurasia and the oblique subduction of the Philippine Sea Plate create a subduction-collision complex offshore Taiwan, which has not previously been elucidated in detail. We combine traveltime data from the seismic networks in Taiwan and Japan to better illuminate how the subducting Ryukyu slab deforms in this subduction-collision zone. More than 5000 events recorded by both networks were relocated with the double-difference method using an optimal regional 1-D velocity model. The offshore seismicity indicates that the double seismic zone, with a gap of 15-20 km, exists in the subducting slab in the depth range of 40-80 km. Focal mechanisms suggest that the double seismic zone is caused by east-west compression resulting from oblique convergence.

The improved hypocentral locations for the first time reveal folding of the slab into a horizontal curvature larger in magnitude than and opposite in sign to that of the Ryukyu trench in the depth range 50-100 km. The anomalous curvature, together with the focal mechanisms, suggests that the slab folds against the Eurasian lithosphere and that this deformation cannot be fully elastic. We model this deformation mode as the developing instability of a viscoelastic Maxwell layer embedded in a viscous medium. The characteristic wavelength of the instability, i.e., ~250 km, is consistent with folding of a slab whose viscosity is 100 times higher than that of the surrounding mantle for an along-strike elastic membrane strain as small as 0.01, or more than 3 orders of magnitude higher if 5% elastic strain is allowed.

Three dimensional tomographic images of the subducting Philippine Sea slab and the forearc mantle beneath NE Taiwan and the westernmost Ryukyu were generated in this study. More than 5600 events recorded simultaneously by seismic networks in Taiwan and Japan were relocated for the inversion for variations in V_P, V_S, and V_P/V_S. Analysis of the tradeoff between the data variance-reduction and model-variance helps to determine the appropriate strictness for regularization to avoid either over- or under-interpretation of data. The regularization parameters were also chosen to ensure suppression of artificial V_P/V_S anomalies. The

subducting slab is characterized by high V_P, high V_S, and intermediate to low V_P/V_S. Notable in the mantle wedge is the high V_P/V_S anomalies that abut the surface of the subducting slab at depths of 30-80 km. The previously identified positive V_P/V_S channel connecting the slab and the arc volcano interpreted to be a melt pathway is not reproduced in this study.

We convert V_S and V_P/V_S to perturbations of temperature and serpentinization of the mantle. The slab is cooled by 200-400^{o}C relative to the mantle, in accord with the estimates from theoretical modeling of subduction. The serpentinization reaches ~15%, or 2% water content, at 50 km depth in the forearc mantle. We interpret the peak serpentinization as hydrated by the water released from the basalt-eclogite metamorphic reaction in the oceanic crust of the subducting Philippine Sea plate. The spatial limitation of the present seismic networks in this region with respect to subduction zone events hinders a full description of the pattern of melting in much of the mantle wedge. Resolution tests of the tomographic inversion provide a basis to guide our interpretation to better resolved regions.

第一章　簡介

在 1997 年的當時，S. P. Grand 以及 van der Hilst 等人（Grand et al, 1997; van der Hilst et al, 1997），分別根據 P 波及 S 波的走時資料，發表了北美洲底下的震波層析影像（seismic tomography）。代表隱沒板塊的高速異常，從地表一路向下延伸至核幔邊界的影像（圖一），不僅讓我印象深刻，也完全顛覆了我過去對於板塊隱沒的認知。因此，建立一幅震波層析影像以探索地球內部構造，就成為我對後續研究工作的發想。

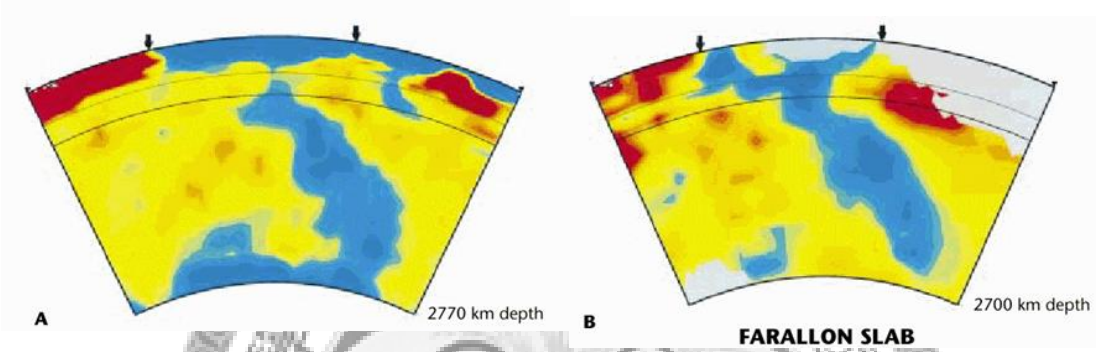

圖一　北美洲底下的震波層析影像。左圖 A 為 Grand et al, 1997 根據 P 波走時所建立的震波層析影像，右圖 B 則為 van der Hilst et al, 1997 根據 S 波走時所建立的震波層析影像。

1.1 震波層析影像的發展與演進

由於大量現代化地震測站的陸續建置，使得數位化地震資料的數量也被快速累積，因此地球物理學家對於地球內部結構的研究，也開始由一維的均向構造轉向了三維的不均向結構。三維震波層析影像的結果第一次被發表，是在 1974 年的美國地球物理聯合會秋季大會（Fall meeting of the American Geophysical Union）上（Aki et al., 1974）。只不過要一直到 1980 年代中葉，藉由引進醫學上所使用的 X 光層析影像技術中，以迭代方式解析矩陣的方法，改進震波層析影像的技術後，才獲得了大家對於這個方法的信任。同時也借用了醫學上「層析影像」這個名詞，作為往後此一研究方法的代稱。改進之後的全球地震層析影像結果（例如：Dziewonski and Anderson, 1984），相對於地球內部的其他研究結果（例如大地水準 Geoid），都可以得到相當好的解釋與相關性。因此，震波層析影像的方法開始被廣泛地應用在全球各地，用以探索地球內部構造的特徵。

震波層析影像方法在 1980 年代中葉之後，除了改進以迭代方式解析矩陣外，也改進了格點設置的方式、射線追蹤的方式、以及震波速度不連續面的設置等等。最早被廣泛使用的震波層析影像方法是由 Thurber 在 1983 年所提出，並

在 1993 及 1999 做了程式內容的部分修改（Thurber,1983, 1993; Thurber and Eberhart-Phillips, 1999），目前程式的版本為 SIMUL2000。此一程式的特點在於同時反演P波速度異常及P波與S波速度比值，但對於走時殘差（travel time residual）的分配權重以及壓抑係數（damping factor）和取捨曲線（trade-off curve）的建立上仍有值得討論的地方（詳見 5.1）。

另外，Zhao 在 1992 年所提出的震波層析影像程式（Zhao, 1992）中，最大的特點在於不連續面的射線追蹤及速度模型建立，藉由先驗的不連續面三維分布，可以相當程度地消除震波層析影像反演過程中的誤差。除此之外，與 Thurber 方法的最大不同之處在於，Zhao 的方法是獨立解析 P 波與 S 波的震波速度異常，因此 P 波與 S 波資料的品質與分布都不會互相影響，其壓抑係數與取捨曲線則可輕易建立，以決定矩陣反演的結果。但也因為 P 波及 S 波速度的反演為獨立過程，因此若要獲得 P 波與 S 波速度的比值，則需進一步檢驗，以確定其結果的可信度及誤差範圍（詳見 5.1）。

近幾年來，已有更多對於震波層析影像方法所做的修正與改進，包括地震波射線採樣區域的修正（sensitivity kernel）、多尺度小波計算（multi-scale wavelet）等等。以及利用體波走時之外的其他觀測，包括表面波層析影像、波形層析影像、自由震盪（normal mode）層析影像等等。這些不同面向的研究方法所提供不同的控制，對於研究地球內部構造來說，助益將更是不可同日而語。

1.2 從震波層析影像看隱沒帶的構造活動

藉由震波層析影像的建立，過去僅能藉由班尼奧夫帶地震分布所勾勒出概略的隱沒板塊幾何型態，現在已經可以非常清楚地在震波層析影像中看見隱沒板塊由於低溫所造成地震波速度的高速異常（例如：Zhao et al., 1997）。甚至在部分已經沒有班尼奧夫帶地震分佈的深度與地區，還可以透過震波層析影像的方法來獲得隱沒板塊的分佈，藉此進行相關力學與地球動力之分析，是相當重要的一個資訊來源。

除此之外，由於岩石部分熔融產生岩漿時所造成地震波速度的變化，使得震波層析影像成為探測隱沒帶地區的火山島弧或弧後盆地張裂岩漿活動的重要工具（例如：Zhao et al., 1997）。藉由 P 波與 S 波速度的低速異常以及 P 波與 S 波速度比值變大的異常分佈，可以分析岩漿活動的來源深度與上湧過程。搭配地球化學針對地表噴出火成岩的元素分析，將可更進一步探討岩漿形成過程以及地幔的成分與演變。

由於震波層析影像的解析度日益提高，搭配反射震測及實驗岩石學的理論模式，使得近年來有更多針對隱沒板塊表面及地幔楔之間交互作用的研究結果被提出來。包括隱沒板塊脫水、地幔楔蛇紋岩化以及部分熔融形成岩漿等等（例如：

Zhao et al., 1997），更進一步地將研究範圍深入隱沒帶的核心，以期獲得更完整的認知。

但是，由於隱沒帶的分佈區域大多位在海陸交界，受限於地震測站主要分佈在陸地地區的緣故，要建立隱沒帶地區完整的震波層析影像其實相當困難。因此近年來陸陸續續有深海地震儀的佈置，補足了許多原本缺少波線通過的區域，建立起更臻完善的震波層析影像。

1.3 地震定位與參考速度模型

區域性地震定位與參考速度模型的建立，同時都是根據震波走時記錄而來，因此兩者之間在反演過程存在有相互取捨的關係。部分地震定位的工作還建議將測站修正納入反演過程，但原本可能屬於地震定位與速度模型的走時殘差，亦會因此被歸入測站修正之中，不見得能夠真正反應出測站本身的特性。

區域性地震定位的特點之一，就是側向速度差異的變化對地震定位結果影響較為明顯，因而衍生出兩種對應的解決之道。一是利用地震與地震間相對位置的差異，以消除震波速度在側向上的變化，例如：聯合震源解析（Joint Hypocenter Determine, JHD）或二次差分法（Double Difference）。第二種方法則是利用三維速度構造進行射線追蹤與定位，將側向上的速度變化納入地震定位。但第二種方法同樣存在震源位置與速度模型實為互相取捨的問題，若是無法將兩者區隔開來，則永遠無法獲得可信的地震定位或速度模型結果。

因此本研究特別採用參數分離的方法，先將震源與速度模型效應分離，先求得一維速度模型；然後再利用二次差分法進行定位，最小化側向速度差異可能的影響，以獲得較佳的地震定位；最後再以此一維速度模型及地震定位，進行三維速度構造的反演，得到震波層析影像的結果（詳細過程請見第三章）。

1.4 從震源分佈看隱沒板塊的力學特性

藉由全球地震分佈的資料，我們可以清楚描述在世界各地的隱沒帶中，每個隱沒板塊在地幔中的三維型態（例如： *Chiu et al.*, 1991; *Engdahl et al.*, 1998）。結果顯示隱沒板塊的幾何型態大多與地表尚未隱沒的海洋岩石圈相同，並且少有額外的延展或平面變形存在（*Burbach and Frohlich,* 1986*; Yamaoka et al.,* 1986）。這表示側向延伸數千公里，厚度卻僅有數十公里的隱沒板塊，比較傾向於撓曲變形的模式而非平面變形。然而，也有一些研究結果顯示，隱沒板塊在進行撓曲的同時，也會發生區域性表面變形的現象（例如： *Bevis*, 1988）。相對來說，撓曲模式的變形，會造成隱沒角度的改變以及隱沒板塊流場的變化（*Chiao*, 1993）；

而外加於隱沒板塊邊緣的力量改變、海溝遷移、以及過渡帶對於板塊向深處隱沒所造成的阻力，則會造成隱沒板塊在三維方向上的變形，並增加幾何構造上的曲度 （例如： *van der Hilst and Seno*, 1993; *Chen and Brudzinski*, 2001; *Pysklywec et al.*, 2003）。由於這些變形的結構可以沿著海溝走向延伸數百至數千公里，因此即使以全球地震網的地震定位（*Gudmundsson and Sambridge*, 1998; *Engdahl et al.*, 1998），亦應可明確地描述出來。

但若是針對在地幔淺部，變形尺度（沿著隱沒方向）數百公里以下的隱沒板塊進行探討時，就必須考慮下列幾個特性，包括：討論地幔中外加的力時，僅止於考慮地區性所造成的力，或是造成隱沒板塊小尺度撓曲的力量；隱沒板塊的剛性，則會設定撓曲波長的下限，因此較薄、較熱的的隱沒板塊，其變形會比較強、較老的板塊明顯；屈服包絡面會受到摩擦力與冪次定律所主控（例如：*Kohlstedt et al.*, 1995），限定隱沒板塊中的應力大小，並在同樣的彎矩之下，允許產生更大的曲度；最後，地震資料則必須足以準確地描述出板塊在數百公里大小尺度內的變形。而全球地震定位資料由於受限於地震規模大小的門檻，以及全球平均速度模型的使用，使其結果可能不足以應用在描述具有：區域性、小尺度變形的隱沒板塊區域之研究。

第二章　臺灣-琉球間的構造活動

琉球隱沒帶與臺灣北段褶皺造山帶的板塊構造演化之間（圖二），關連性相當密切（例如： *Teng*, 1990; *Sibuet et al.*, 1998）。像是臺灣北部及北部外海的火山活動與演化，其成因雖然相當複雜，但主要仍是源自於琉球島弧後方的弧後張裂及地幔楔上湧（*Wang et al.*, 2004a）。由於地震觀測站分佈的侷限，西琉球的地幔楔一直未能清楚地被觀測，僅有臺灣島下方一小部分，可藉由臺灣島上測站進行觀測（*Lin et al.*, 2004）。一般認為，沖繩海槽源自於隱沒系統中的弧後盆地，延伸進入臺灣東北角落，於是在台灣碰撞—造山的環境中引發區域性張裂的構造活動。

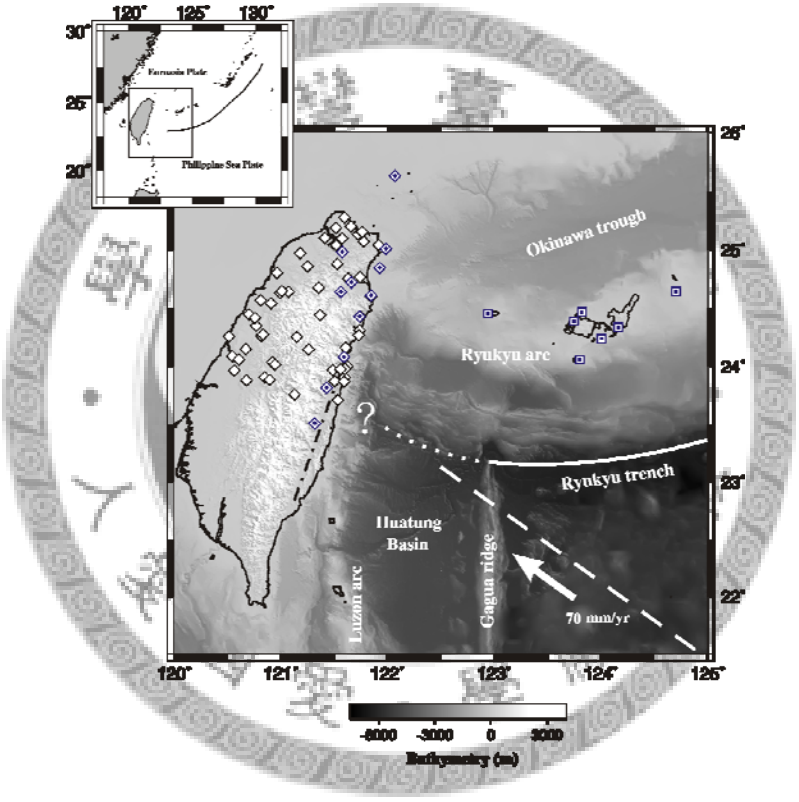

圖二　地圖顯示臺灣—琉球間的隱沒—碰撞區域之板塊構造架構，以及本研究進行地震重定位所使用之地震測站。主要的板塊構造特徵都有加以標示。中央氣象局的 11 個地震測站（實心菱形）以及日本氣象廳的 7 個地震測站（實心方塊）形成一個覆蓋隱沒—碰撞附近區域的網路。對於發生在海岸內的地震，除了利用中央氣象局的 11 個地震測站，還加入了其他中央氣象局的地震測站（空心菱形），以建立另一個可以覆蓋整個北臺灣的網路。琉球海溝一般的趨勢為向南突出（圖中的白色實線和點線，以及小圖中的黑線），但在靠近臺灣附近時難以辨識。虛線表示菲律賓海板塊未來會隱沒進海溝的部分其邊界位置。這個邊界是平行板塊運動方向（箭頭），根據 *Seno et al.*（1993）所提出。穿過臺灣東岸的點虛線代表菲律賓海板塊與歐亞板塊的交界。

2.1 菲律賓海板塊的隱沒

西菲律賓海板塊在琉球海溝向西北方向隱沒，琉球海溝的曲度在中段達到最大值，0.002 km^{-1}，與馬里亞那海溝的曲度，0.001 km^{-1} 相當。琉球海溝大部分區域的曲度都更小，表現出大尺度的二維結構，而沒有明顯的變形發生在海溝走向上。菲律賓板塊以每年七公分的速度，北偏西 50 度的方向，與歐亞板塊聚合（*Seno et al.*, 1993）。聚合角度在東半側的琉球海溝較大，然後漸漸往西減小。在到達臺灣外海數百公里的範圍時，隱沒角度減少到 20°以下，這表示隱沒板塊所受到區域性的應立場也在此發生明顯改變。根據地震斷層機制解的結果（*Kao et al.*, 1998），顯示在這個地區主要受到側向壓縮的應力，且碰撞作用成為改變隱沒板塊形貌的力量。

在這個約一百公里寬的隱沒—碰撞帶地區，仍有幾個關鍵又令人費解的問題。例如加瓜海脊很明顯地在東經 123 度位置侵入琉球海溝，而隱沒板塊在加瓜海脊西側，是以較陡的角度在隱沒，東側則較緩（例如： *Deschamps et al.*, 2000）。海脊的起源以及它與上覆板塊之間的交互作用，則曾經有過相關的探討（*Deschamps et al.*, 1998; *Schnurle et al.*, 1998）。過去不論是利用遠震資料（*Engdahl et al.*, 1998），或是本地的中央氣象局定位資料（*Kao and Rau*, 1999; *Font et al.*, 1999），都曾經被用為描述隱沒板塊幾何形狀的依據。中央氣象局的地震定位資料顯示，隱沒板塊由東向西的變化相當平滑，沒有明顯差異（例如：*Kao et al.*, 1998）。而 *Font et al.* （1999）呈現了利用中央氣象局資料所重新定位的隱沒板塊等深線，反應出若非地震定位的不準確，則是地形的特徵，而非岩石圈的機械性撓曲。如同先前所提到，為了結合臺灣與日本地震觀測資料進行定位，曾經由 *Hsu* （2001）進行嘗試，利用日本氣象廳有限的地震資料，呈現了兩個觀測網資料整合的第一步研究結果。

2.2 菲律賓海板塊西緣的構造與力學性質

琉球隱沒帶最西側一百公里，位在海溝末端與臺灣島交會邊界，與歐亞岩石圈相接處。由於斜向隱沒角度的增加以及與一旁歐亞岩石圈的相接，此處的隱沒作用也持續在碰撞疊加。在台灣東北海域的這個交界區域，複雜的海床型態與沈積物分佈，將海溝向西延伸的曲度變化給掩蓋，使得我們無法藉由隱沒板塊在

地表分佈的型態，瞭解板塊隱沒後的模樣。時至今日，要描述這個區域的隱沒板塊，仍有相當大的限制。像是利用全球地震資料（*Engdahl et al.*, 1998）所能獲得平滑、沒有特徵的構造（例如： *Lin et al.*, 2004）。由於這個區域幾乎完全位於島外，因此若僅使用島內的地震測站，可能會造成地震定位上系統性誤差的風險。根據地理分佈的觀點，位於琉球島弧最西側的數個日本觀測網測站，可以提供這個區域地震定位重要的控制。但可惜過去兩方在地震研究的合作上，一直未能清楚認知到這件工作的重要性，導致我們對於隱沒板塊在此區域的幾何型態、與歐亞板塊的交界狀況，迄今仍瞭解得相當有限。

Wang et al.（2004b）曾經針對琉球海溝以北的弧前盆地，進行多頻道海底反射震測研究，觀察菲律賓海板塊的地殼構造。其研究結果所得到的速度模型，提供了一窺岩石圈在開始隱沒階段的物理狀態。而三維的速度影像顯示在弧前盆地底部，平行島弧的方向上，產生了變形。這個變形被認為是菲律賓海板塊在台灣地區與大陸邊緣作用，因而造成褶曲的證據（*Wang et al.*, 2004b）。但這個現象仍不確定為地殼的表徵，亦或是整個菲律賓海板塊的力學行為。除此之外，在他們的模式中，弧前盆地之下的海洋地殼就有大約十公里厚，只不過在更深的深度時，就沒有相關證據的控制性了。不論是隱沒板塊褶曲或地殼增厚，都是緣於歐亞板塊這一側阻擋了深處斜向隱沒的進行，以及隱沒板塊如何機械性地將撓曲向下傳遞的問題。

對於分析琉球隱沒板塊的機械性強度與溫度結構來說，瞭解西菲律賓海盆的形成年代亦是個重要條件，只不過這個議題迄今仍無定論。根據 *Seno and Maruyama*（1984）的板塊重建模式，海盆的年紀估計約為 40 百萬年；根據 *Deschamps et al.*（2000）利用輝長岩的定年結果，認為菲律賓海板塊位於臺灣與加瓜海脊間的部分，年齡相當老（大於 100 百萬年）。不過，由於隱沒方向並非直接往北，因此大部分的花東海盆正在往撞向臺灣的路程上前進，而不會隱沒至琉球海溝之下，除非板塊運動方向在未來發生戲劇性地轉向。

2.3 雙層地震帶

Kao and Rau（1999）曾經利用中央氣象局的地震定位結果，探討清楚出現在台灣東緣的雙層地震帶剖面，並辨識出由於構造應力所造成水平向壓縮乃至於

雙層地震面的形成。作者藉由類比海洋隱沒板塊與大陸岩石圈的岩相結構，將塑性的下部海洋地殼夾在脆性的上部地殼及上部地幔之間，用以解釋雙層地震帶的間隔（約 10-20 公里）。作者將此標示為第二型的雙層地震帶，以區別一般被認為彎曲—反彎曲隱沒板塊，並在較深處所形成的第一型的雙層地震帶。在這篇報告中，我們將檢驗大部分位於外海的雙層地震帶，並分析「果醬三明治」以及變質反應系列正反之間的理論。

我們於是結合了臺灣與日本的地震觀測資料，重新將隱沒—碰撞帶內 150 公里寬的鄰近區域地震重新定位。重定位的過程包含一些必要的步驟，降低對兩方觀測網中任一方的偏頗，以及減低三維構造不均向性所造成的效應。藉由較佳的地震定位，可以在外海區域的中層深度，發現雙層地震帶的存在。顯示 *Kao and Rau* （1999）所發現臺灣北部地底的雙層地震帶現象，向東延伸至少一百公里。除此之外，相較於過去利用臺灣地區地震資料或全球地震資料的研究中（*Kao et al.*, 1998; *Hsu*, 2001），觀察到隱沒板塊自琉球海溝所投影出的幾何形狀，我們發現一個細微、但具系統性的變化，顯示這個區域可能存在一個不同模式的變形構造。若考慮動力機制方面的解釋， *Chiao et al.* （2001）曾提出隱沒流場向東旋轉以釋放延島弧方向之應變的說法。雖然這個旋轉模式或許存在，但我們藉由高解析度的隱沒板塊幾何形狀，建立了褶皺模式的理論來解釋。我們將這個不穩定狀態的問題，推導出一個黏彈性層受到壓縮時的反應，以解釋在不同岩相構造下，根據地震定位結果顯示之褶皺所表現的形狀。

2.4 琉球隱沒帶火成活動與震波層析影像

在隱沒帶地幔楔系統中，最重要的元素之一就是直接與隱沒作用進行相連結的活動火山前緣。在琉球島弧的東北端，現今的活動火山前緣可以藉由追蹤日本九州以南的活動火山而清楚地定義，其下的瓦達地班尼奧夫帶則深達 100 公里。這些火山空間分佈的特性吻合地幔楔動力與岩石學的範例（*Tatsumi and Eggins*, 1995）。然而，要定義琉球島弧最西側的活動火山前緣就不那麼顯而易見了。日本氣象廳所位處的西表島與石垣島已不再活躍，且僅位在瓦達地班尼奧夫帶上方 60 公里處（例如：*Shinjo*, 1999）。現今的活動火山前緣或許已經沿著這些島嶼的北邊，成為一群一群排列的海底火山，其下的琉球隱沒板塊約有 100 公里深，且其地球化學特徵與隱沒作用關係密切（*Chung et al.*, 2000; *Shinjo*, 1999）（圖

二)。這些活動火山前緣大多分佈在沖繩海槽軸線以南，但若是向西追蹤到龜山島（一座七千年前噴發的火山島，位在宜蘭平原外海約 10 公里處）時，兩者卻又互相聚合至一處（例如：*Chung et al.*, 2000; *Chu*, 2005）。活動火山前緣的位置，將是我們在探討琉球地幔楔時的關鍵參考。

不同於日本地區，有數百個地震測站位於隱沒帶上方；台灣的高密度地震地震觀測網卻是位在琉球隱沒板塊以西，僅有少數幾個沿著琉球島弧排列的日本氣象廳地震測站，是位在隱沒帶上方。因此地震與測站的幾何分布並無法完全涵蓋到整個島弧以北的地幔楔。但是就研究台灣外海地區來說，相對於僅單獨利用中央氣象局的資料，結合日本觀測網還是提供了顯著的助益。台灣北部下方的琉球隱沒帶，是由 *Rau and Wu* （1996）第一次忠實地揭露。最近 *Lin et al.*（2004）則利用中央氣象局的資料，提供了台灣東北區域一個新的模型；本研究則是另外結合日本觀測網的資料，縱使這些資料越往東邊覆蓋範圍越窄，但仍舊可以對於只有台灣觀測網所建立模型提供更好的控制。在後續的努力中，*Lin et al.*（2007）亦延伸了他們的模型到達外海 124°E 的區域，並結合日本氣象廳以及 12 天的海底地震儀資料。本研究與 *Lin et al.* （2004; 2007）除了利用不同的資料組之外，反演的策略與解釋亦不相同。

第三章　資料與研究方法

我們首先針對規模大於四，發生於 1991-2003 年間，原始定位在東經 121.5 度至 124 度，北緯 23.5 度至 26 度間，超過六千個的地震。並選擇靠近臺灣東北海岸的 11 個中央氣象局測站，以及七個日本氣象廳最西邊的測站，在幾何分佈上圍起一個棚架區域（圖二）。選用的地震必須至少同時被兩個以上的中央氣象局測站及兩個以上的日本氣象廳測站接收到訊號，以確保最低程度的測站記錄平均分配。由兩個觀測網所各自提供的絕對到時，包括有 74403 個 *P* 波到時以及 60952 個 *S* 波到時作為初始定位資料。地震層析影像的反演，則會根據重新定位後的地震資料來進行。

3.1 地震測站的選用

即使中央氣象局的地震測站遍布整個臺灣地區，但我們只選用了 11 個臺灣東北沿海的地震測站（圖二）資料，原因有二。第一是日本氣象廳在琉球地區的地震測站數目僅有 7 個，若是我們將所有的中央氣象局測站資料均加入反演，在最小誤差總和的計算原理之下，日本氣象廳測站的資料將顯得無足輕重，而無法對地震定位及速度構造的模型做出顯著貢獻。除非我們人為加重日本氣象廳觀測資料在反演過程中的權重。

第二個原因是，臺灣東北外海的地震震波在抵達臺灣西部、西南部測站之前，必須經過臺灣地區複雜的地殼結構，如此一來會導致我們無法準確建立臺灣東北外海的一維速度構造。基於以上兩個理由，我們於是大致選取了數量相當，且位於臺灣東北沿海的這 11 個中央氣象局測站。並挑選同時被兩個觀測網、各兩個以上地震測站所記錄到的地震資料，作為本次研究的觀測數據。

3.2 一維速度模型的建立與參數投影法

首先從地震目錄中，選用中央氣象局根據臺灣一維平均速度構造模型（*Chen,* 1995）所進行定位的結果。然後我們結合中央氣象局與日本氣象廳的資料，並採用 *Chen*'s （1995）臺灣東北區域一維速度模型進行重新定位。為了獲得外海區域更好的一維速度模型，我們在前半段採用 *Kissling et al.*（1994）針對一維速度

構造及震源參數同時進行反演的程式，但在後半段採用 *Pavlis and Booker*（1980）的參數投射操作法，僅反演一維速度構造。

在求得震源參數以及震波層析影像結果之前，我們必須要先有區域性的一維速度構造。但震源參數的獲得，又不得不倚靠其發生地區之速度構造。因此如何將震波到時資料中所包含震源參數及速度構造兩者的影響分離開來，我們採取了 *Pavlis and Booker*（1980）所提出的參數投影分離法。首先，我們利用 *Kissling et al.*（1994）先建立起震波走時與震源參數模型及速度構造模型間的關係如下：

$$t_{res} \equiv t_{obs} - t_{cal} = \sum_{k=1}^{4} \frac{\partial t}{\partial h_k} \Delta h_k + \sum_{i=1}^{n} \frac{\partial t}{\partial v_i} \Delta v_i \quad \text{.....(1)}$$

上式中 *t* 為走時，*h* 為震源參數，*v* 為速度構造參數。上式可簡寫為：

$$r = H\Delta h + M\Delta v \quad \text{.....(2)}$$

並以 *r* 表示為走時差的資料，*H* 為震源參數部分的資料核（data kernel），*M* 為速度構造參數部分的資料核。

然後我們將 *H* 進行奇異數值分解（singular value decomposition），得到：

$$H = U\Lambda V^T \quad \text{.....(3)}$$

其中 $U = \left[U_p, U_0\right]$，$U_p$ 代表資料中對模型具有影響力的部分，U_0 則代表資料中部會對模型造成影響的部分。由於 U 矩陣中所有的列（column）都為彼此正交（orthogonal），因此 $U_0^T U_p = 0$，且 $U_0^T H = U_0^T \left(U\Lambda V^T\right) = U_0^T \left(U_p \Lambda_p V_p^T\right) = 0$。於是我們將 U_0^T 作用於（2）得到：

$$U_0^T r = U_0^T H\Delta h + U_0^T M\Delta v$$

$$\Rightarrow r^* = M^*\Delta v \quad \text{.....(4)}$$

則被 U_0^T 作用過後的關係式（4）中，就不再有震源參數的影響，可供我們求得一維速度構造的結果。

這個方法可以分離震源參數所造成速度結構的影響，加強後者的獨立性。最後呈現的一維速度構造顯示在圖三。*Chen*（1995）同樣使用 *Kissling et al.*（1994）的方法分析中央氣象局資料，但他並未將震源效應自參數中分離。圖三中則比較了我們此次陸地—外海模型，以及他的東北臺灣模型。兩者之間的差異之處並不

明顯，顯示兩個速度模型的深部結構，主要均受到隱沒的菲律賓海板塊所主控。儘管如此，在這個研究中我們還是要強調，將震源效應獨立出來的重要性，特別是當我們要距焦在一個不顯著的隱沒板塊構造時，更應該加以注意。圖三中的速度結構在深於 150 公里以下處，兩個模型的資料控制都不再顯著。

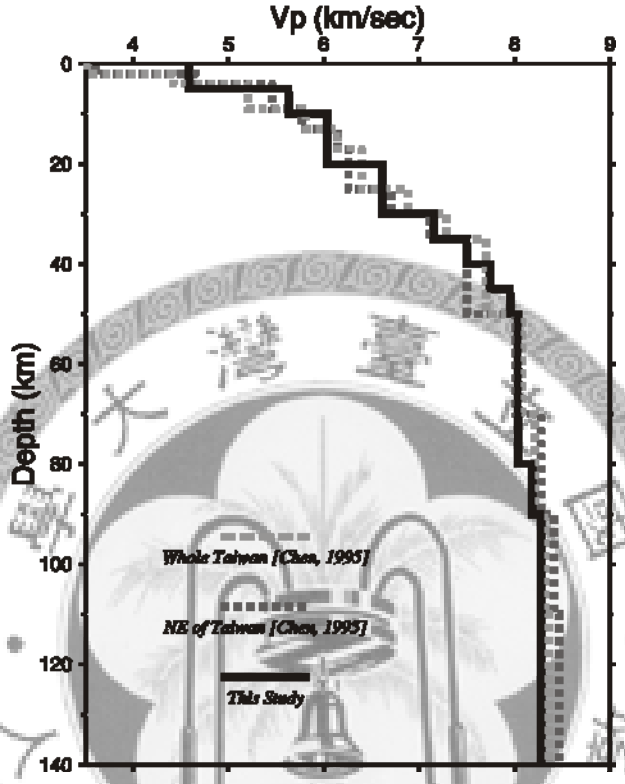

圖三　一維速度模型（實線），由本研究結合中央氣象局與日本氣象廳資料組，並運用投影技術消除震源效應，所得到的速度結果。這個模型並被用在後續的二次差分重新定位中。比較 *Chen*'s（1995）所發表臺灣東北的子區域速度模型（點線）。兩者的相似性顯示隱沒板塊的結構仍為此區主要的影響。

3.3 地震定位與兩次差分法

我們接著使用 *Waldhauser and Ellsworth* （2000）的兩次差分法，使用前述利用 11 個中央氣象局測站及 7 個日本氣象廳測站所得到的一維速度構造，重新定位東經 121.5 度以東的地震。然後，我們掃瞄所有中央氣象局所記錄到介於東經 120.5 度到 122 度間的地震，將尚未被重新定位的地震挑選出來。這些地震主要是在第一輪重新定位的過程中，由於缺少日本氣象聽的觀測數據而被剔除，部分則是因為落在選擇區域之外而未被選入，但這些地震大多位在中央氣象局的觀測網內，足以被準確定位。因此我們選用北臺灣的 30 個中央氣象局地震測站（包

含第一輪的 11 個中央氣象局測站，圖二)，針對這些地震進行重定位。在第二輪的地震定位中，雖然大部分的地震震源位置在島內，但我們仍採用第一輪所建立起的外海地震速度構造，以期在後續進行合併解釋時能具有一致性。除此之外，由於本次研究所關注的重點在於隱沒帶區域而非臺灣陸地地區的地殼結構，且兩次差分法的計算特性具有抵銷測站下方構造不均向性的特色，因此地表附近的速度結構對定位結果影響不大。經過兩次差分法的重新定位之後，變異數縮減可以達到百分之七十。

兩次差分演算法可以將地震對的到時差最小化，這個方法對於地震重複發生的地區較有效率，並可淡化對於測站修正的需求。本研究採用這個方法作為區域地震的重新定位，可以將地殼及地幔的不均向性效應最小化，藉由成對路徑抵達同一測站的走時相減，可以降低三維速度異常經過夫瑞奈帶所造成的效應。因此，在這裡最關鍵的參數便是半徑 r_0，在這個半徑之內，我們搜尋所有鄰近的地震來配對，計算時間差分。在區域性的研究中，r_0必須相對於震波的夫瑞奈帶及不均向性的尺度大小而定。因此若 r_0設得太大，則速度構造的不均向性就有較高的危險性可能會混染地震定位的結果。較小的 r_0可以確定壓抑不均向性效應，但也會因此僅能挑選到少數成對的地震，限制了地震定位的數目。對較深的地震來說，成對地震在測站下方的夫瑞奈帶差異較小（較淺的地震則差異較大），應此可以允許設定較大的 r_0。我們距焦於隱沒板塊的結構，並採用 r_0=30 km 的值。由於成對地震間的距離遠小於 r_0，因此若採用 r_0=20 km 並不會得到太大差異的結果。在深度範圍 50-150km 間，成對地震的數目約為 100 左右，但在大於 150km 深之後，成對地震數目就降到了 10 左右。我們於是設定本研究中最大及最小的地震配對數目分別為 100 和 8。某些深部地震由於距離其他地震太遠而無法配對，只好在重新定位的過程將之捨去。經過兩次差分法重新定位之後的地震數目為 5667，相對 *P* 波與 *S* 波的到時記錄則分別為 69760 及 57412。

由於「單次」差分法（一般的地震定位）在區域性地震與遠震的研究上都受到了爭議，因此選用雙次差分法與一維速度模型，相對於三維修正的方式要值得信任。在這兩者間的選擇，是建立在我們對三維層析模式所建立起的三維修正沒有信心。由於要在層析反演的結果中呈現隱沒板塊並非難事，因此反演過程中往往大幅度地壓抑並平滑化其速度結構（例如： *Ma et al.*, 1996; *Rau and Wu*, 1995）。除此之外，這些層析模式的淺層速度結構往往也都沒有很好的資料控制。

最近 *Kim et al.,*（2005）在建立台灣地區地殼層析影像的過程中，系統性地演算出站位效應。這個模式提出了對於淺層結構(包含地殼以下)比較好的控制能力，也因此成為一個足以提供三維地震定位的初始模型，只不過這個研究的研究區域並未包含外海的地殼與上部地幔，而無法對本研究提供幫助。根據我們的經驗，目前本區由三維層析影像所建立的三維速度構造，尚未達到足夠成熟的地步，足以讓我們在這個地區結合中央氣象局與日本氣象廳的地震資料，進行精密的地震定位工作。*Wu et al.*（2004）同樣使用兩次差分法針對台灣地區的地震進行定位，探討台灣的內部結構與造山帶。

3.4 震波走時記錄的時間延遲

為了結合兩個不同地震觀測網的震波走時，我們還必須考慮兩個地震網不同的時間記錄系統，是否會影響地震定位結果。日本氣象廳的測站記錄，是在每一個測站當地附加上時間碼；而中央氣象局則是在資料中心才將時間碼附加至每個測站地震資料內（時間碼都是根據全球衛星定位系統的訊號）。基於最樂觀的假設，過去一直認為地震資料遠距傳遞所造成的延遲微小到可以忽略，因此台灣地區（至少是北台灣地區）地震測站資料的時間延遲，均未被正式地定量描述。為了檢驗這種現象會對我們的研究結果造成甚麼影響，我們分析了中央氣象局 NWF 測站與寬頻地震網 WFSB 共站的資料（WFSB 測站記錄的時間碼附加方式為原地附加），比較 1999 年至 2004 年間，地震 P 波到時記錄的差異。統計結果顯示，兩者間 P 波到時差距的平均值為 0.03 秒，標準差為 0.02 秒。由於 NWF 與 WFSB 測站為北台灣地區唯一的共站，因此我們假設這樣的統計結果是具有代表性的。

為了衡量這樣的差異是否會造成我們在結合兩個地震網的觀測資料時，造成嚴重的地震定位偏差。於是我們將中央氣象局的震波到時記錄均提前一個亂數值，亂數的平均值為 0.03 秒，標準差為 0.02 秒，然後才結合日本氣象廳的地震資料。然後我們再利用這一組測試資料進行二次差分法重新定位，並觀察新得到的地震定位分布結果。新的地震分布結果非常類似原始資料的定位結果，因此隱沒板塊的幾何形狀與主要地震分布結構(下一段我們將會進行討論的特徵)也都仍舊一致。我們認為中央氣象局地震資料附加時間碼的過程，並不會影響到本研究中所討論到的特徵現象。

但其後我們分析了更多其他地區共站的紀錄，並分析這個延遲現象與時間序列之間的關係之後發現，全臺灣地區中央氣象局的觀測記錄延遲平均可以達到 0.09±0.14 秒，遠大於北部（離中央氣象局中心較近的地區）的延遲。且若將延遲現象對應時間序列繪圖（圖四）之後可以發現，這個延遲現象在 2003 年前後有明顯落差。

圖四　中央氣象局與中研院寬頻地震測站共站之震波記錄延遲隨時間變化。橫軸代表時間，縱軸代表中央氣象局短週期測站記錄與寬頻地震測站記錄相減的時間差，單位為秒。

在 2003 年之後，全臺灣地區中央氣象局的觀測記錄延遲平均可以高達 0.14±0.09 秒；在 2003 年之前，卻是異常地-0.07±0.17 秒，表示震波記錄的時間反而提早了？！因此我們初步利用 1999-2004 的資料計算時間延遲時，由於跨過 2003 年前後，正負延遲異常的平均值互相抵銷，才會得到誤差結果較小的結果。這也是未來我們要使用中央氣象局走時資料時，需加以注意的地方。

3.5 震波層析影像的反演

本研究採用 *Zhao et al.*（1992）的區域走時層析影像計算方法。在研究範圍：緯度 23.0 到 26.0°N 間，經度 120.4 到 124.0°E 間（圖五），我們建構了水平方向間隔為 0.2°，垂直方向在深度 100 公里範圍內，間隔為 10 公里，深度 100 到 200 公里範圍內，間隔為 20 公里的網格。然後我們反演 *P* 和 *S* 的走時，求出相對於一維速度參考模型的 V_P 和 V_S 差異。

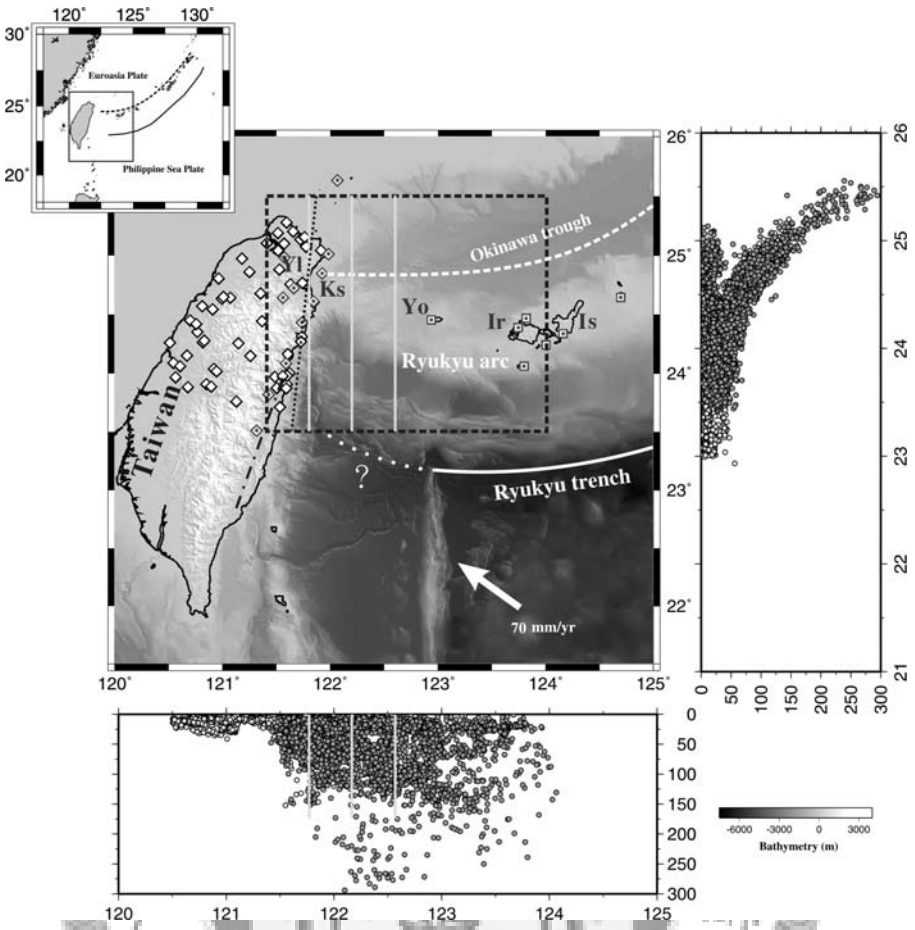

圖五　研究區域的索引地圖，包含區域海底地形、測站與地震分布，圖中以黑色虛線框起來的範圍是本次研究區域。中央氣象局地震測站（菱形）與日本氣象廳地震測站（正方形）觀測網互補涵蓋這個區域。箭頭表示菲律賓海板塊與歐亞板塊是以 70 mm/yr 的速度聚合。實線與點線的結合標示了琉球海溝及其往西未知的延伸。沖繩海槽中的白點線指出今日活躍火山前緣的位置（*Chung et al.*, 2000）。剖面所在的位置在上方及底下的圖中，以南北向白色實線表示。*Lin et al.*（2004）的剖面 2 斜切過本研究的經度 121.8E 剖面，以黑色虛線表示。**Ks** 代表龜山島；**Yl** 代表宜蘭平原；**Yo** 代表與那國島； **Ir** 代表西表島； **Is** 代表石垣島。

我們更進一步從資料組中，建立同一組地震與測站間，同時記錄了 P 與 S 到時的資料。這組資料包含了原始資料中 80%和 98%的 P 以及 S 到時，根據這組資料，我們於是建立起 V_P/V_S 模型。注意：

$$\frac{\delta(V_P/V_S)}{(V_P/V_S)} = \frac{V_S\delta V_P - V_P\delta V_S}{V_S^2}\cdot\frac{V_S}{V_P} = \frac{\delta V_P}{V_P} - \frac{\delta V_S}{V_S} \tag{5}$$

我們將 V_P/V_S 的異常簡單寫成 V_P 和 V_S 異常比例相減的形式。換句話說，顯著的 $\delta(V_P/V_S)$ 變化形式，僅受到 $\delta V_P/V_P$ 和 $\delta V_S/V_S$ 的反演所控制。不同於利用 P 和 S-P 走時差以反演 $\delta(V_P/V_S)$ 及 V_P 的方程式（例如：*Walck*, 1988），需要在最後讓兩個反演結果相除。對我們來說，方程式（5）可以更直覺地被掌握，並根據兩個反演結果進行代數的加總，換言之 $\delta V_P/V_P$ 和 $\delta V_S/V_S$ 各自所存在的誤差（我們不想要的東西），就不會因為兩者需要相除而將誤差放大。在附錄中，我們根據相同的波線路徑幾何分佈，並用已知的合成結構設計實驗，以得到空間的解析能度差異。

我們利用大量的反演實驗來檢測變異量降低對模型變異量的取捨關係，並從取捨曲線決定合適的壓抑（damping）係數（圖六 a）。模型解釋資料的能力以及這種能力所必須付出的代價必須互相妥協，例如模型的不確定性是在達到圖六 a 取捨曲線中突出的一點時。下一步我們測試出一組對 V_P 和 V_S 而言是最佳的壓抑係數，且同時也是 V_P/V_S 的最佳壓抑係數。圖六秀出的輸入模型，包括隱沒板塊區域和上覆地幔區域分別針對 V_P 和 V_S 的速度給予+8%和-6%的速度異常。我們利用這個模型，以及與反演 V_P/V_S 時相同的地震—測站組合，建立合成的 P 和 S 走時，然後同樣以反演真實資料的方式進行反演。根據方程式（5），同樣比例的 V_P 和 V_S 異常，其 V_P/V_S 的異常應該為零。圖六秀出了三種壓抑係數的組合，三組係數皆符合最佳化的取捨曲線。在這三個例子之中，圖六 d 的組合看來可以較有效地壓抑地幔中的 V_P/V_S 異常，使其最符合 $\delta(V_P/V_S)$ 為零的輸入模型。對 V_P 的壓抑不足時，會造成 V_P 的變異加大，導致 $\delta(V_P/V_S)$ 為正，反之亦然。在使用相除的方式時，則會利用過大的壓抑係數，以降低 $\delta(V_P/V_S)$ 的變異。我們使用圖六 d 的參數組合作為反演之用，以確信我們不會過度解釋 V_P、V_S 和 V_P/V_S。

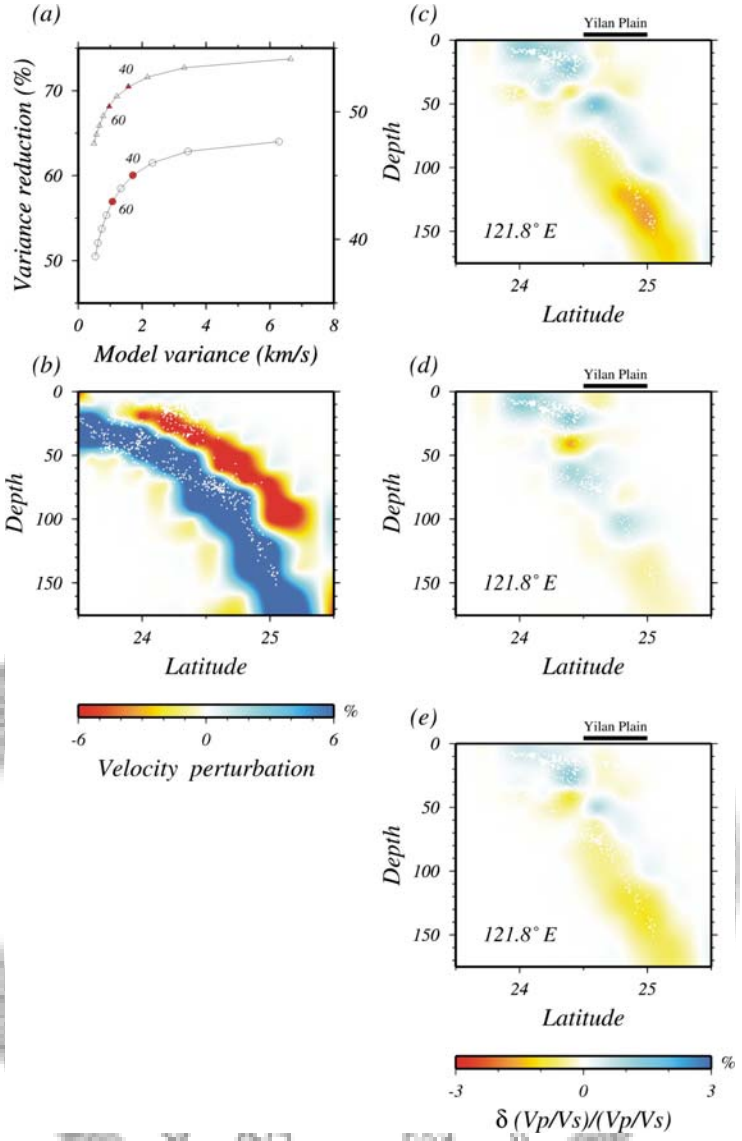

圖六　針對 V_P、V_S和 V_P/V_S所進行的取捨測試（a）V_P和 V_S的取捨曲線，顯示模型變異量與資料變異量減低間的妥協，取在曲線的凸出點。這兩個各自最佳化的壓抑係數卻可能造成人為的速度比異常。（b）輸入合成構造為模仿一個誇張的隱沒帶，且在隱沒板塊及地幔楔中的δ(V_P/V_S)為零。反演結果輸出，V_P和 V_S壓抑係數分別為（c）40-40、（d）40-60、（e）60-60。在（c）的結果中，產生人為非零的δ(V_P/V_S)異常，而（d）和（e）的組合則對隱沒板塊及地幔楔都有較好的壓抑。

3.6 棋盤檢定與解析力矩陣的建立

由於在大部分區域性的震波走時層析影像都有射線覆蓋範圍不均的問題，導致了速度變化模型在空間上採樣明顯地參差不齊。一般是藉由建立簡單的模擬構造進行還原試驗，以獲得層析影像模型在空間上不同的解析能力。以下為本研究所採用的解析力檢定方式：

一，棋盤式檢測（checker board test）。我們建立一組三維棋盤形式的模擬構造，以±6%的速度異常構造分佈在我們模型的格點上，水平方向間隔為 0.2°，垂直方向為 10 公里（深度淺於 100 公里時）與 20 公里（深度深於 100 公里時），同時我們另外還建立一組二倍格點大小的模擬構造作為比較。模擬的走時殘差中均混入隨機的誤差，該誤差的平均值為零，標準差為 0.8 秒。由於波線的路徑與真實反演的資料一致，因此我們直接取用實際反演過程中的壓抑係數。誤差和壓抑係數對棋盤檢定有相當程度的影響，但過去的研究卻常常忽略這部分的討論。

二，解析度測試（resolution test）。要解出速度構造模型 m_g，可以透過資料核的反矩陣 G_g^{-1} 與觀測資料 d 作用而獲得：

$$\vec{m}_g = G_g^{-1}\vec{d} \quad \text{.....(6)}$$

而資料 d 事實上為資料核 G 與速度構造 m 作用的結果：

$$\vec{d} = G\vec{m} \quad \text{.....(7)}$$

將（7）代入（6）可以得到：

$$\vec{m}_g = G_g^{-1}G\vec{m} \quad \text{.....(8)}$$

由上式中可以觀察得知，我們所解出的速度構造模型 m_g，其實是藉由 $G_g^{-1}G$ 作用到真實的速度構造模型 m 之上所獲得，因此 $G_g^{-1}G$ 就是真實模型的解析度矩陣。於是我們同樣利用奇異值解析可以得到：

$$\vec{m}_g = G_g^{-1}G\vec{m} = V_p\Lambda_p{}^{-1}U_p{}^TU_p\Lambda_pV_p{}^T\vec{m} = V_pV_p{}^T\vec{m} \quad \text{.....(9)}$$

則解析度矩陣即為 $R = V_pV_p^T$。藉此可以判斷我們所求得的速度構造，相對於真實構造的解析力。解析力過低的區域（本研究以 25%為門檻），縱使有任何構造存在，其真實性的必須加以懷疑。

3.7 反演隱沒板塊與地幔楔之溫度異常與蛇紋岩化程度

我們的層析影像反演輸出三種形式的異常，包括：V_P、V_S、和 V_P/V_S，其中只有兩個獨立參數。由於 V_P/V_S 對於地幔楔的水合或熔融的反應比單獨看 V_P 或 V_S 要來得明顯，但它只對 V_P 或 V_S 其中一種參數獨立，並非同時獨立於兩者。在這個段落中我們將量化由於隱沒地殼脫水所造成的地幔楔的水合效應。橄欖岩中主要的水合礦物包括蛇紋石、綠泥石（chlorite）和角閃石（amphibole）。在這之中，蛇紋石主控了橄欖岩內的水預算（*Schmidt and Poli*, 1998）。在本研究中，弧前地幔的水合現象將被參數化為橄欖岩母體中被蛇紋岩化（serpentinization）的程度Θ。其中 100%的蛇紋石（Θ=100）含有 15%重量的水（例如 *Hacker et al.*, 2003），而Θ=0 代表乾的橄欖岩。水可以藉由以下的隱沒作用所提供：（1）沈積物的壓縮，通常發生在淺層（2）海洋地殼從藍色片岩（blueschist）/綠色片岩（greenschist）變質成為榴輝岩相（eclogite facies）的變質反應（3）將已經被蛇紋岩化的的隱沒板塊地幔脫水，通常發生在較深處。

我們選擇 V_S 和 V_P/V_S 作為兩個獨立的參數。我們利用 *Christensen*（1966）和 *Horen et al.*（1996）在實驗室中測量不同程度蛇紋岩化的橄欖岩其傳遞震波速度，結合 *Christensen*（1966）在 2 kbar 壓力下的測量結果以及 *Horen et al.*（1996）在常壓下的測量結果，並以一階線性函數來表示 V_P、V_S、和 V_P/V_S 與Θ的關係。導數 $dlnV_S/d\Theta$ 的值 $-4.84\cdot10^{-3}$ 是取自 *Horen et al.*（1996）。導數 $dln(V_P/V_S)/d\Theta$ 的值 $2.254\cdot10^{-3}$ 則是結合 *Christensen*（1966）和 *Horen et al.*（1996）所提供的 V_P/V_S 資料進行回歸，相關係數> 0.8。這是本研究兩組代表蛇紋岩化程度之微分導數中的一組，指定為第一參數組。

Christensen（2004）強調在前述工作中所量得的速度，主要代表下部地殼狀況下的蜥蛇紋石（lizardite），而不同於弧前地幔環境下較穩定的葉蛇紋石（antigorite）。由於沒有實際數據可供回歸，我們於是將 *Christensen*（2004）的圖八數位化，並取得下列針對葉蛇紋石的微分導數： $dlnV_S/d\Theta = -2.59\cdot10^{-3}$ 以

及 $dln\ (V_P/V_S)\ /d\Theta = 0.636 \cdot 10^{-3}$。兩個係數都比第一參數組要降低許多，我們把這個參數組指定為第二參數組。

另一個讓速度敏感的參數是溫度。我們所採用的微分導數為 $dlnV_S/dT = -1.00 \cdot 10^{-4}\ ^{o}C^{-1}$ 以及 $dln(V_P/V_S)/dT = 2.3 \cdot 10^{-6}\ ^{o}C^{-1}$（*Lee*, 2003）。這些係數理應都是溫度與壓力的函數，但我們無法得知更高次項精確地慢數，因此我們採用他們的常數形式，來將層析影像模型轉換為地體構造上更有意義的變數。我們接著解下述的方程式以轉換 V_S 和 V_P/V_S 成為 δT 和 $\delta\Theta$：

$$\begin{bmatrix} \dfrac{\partial lnV_S}{\partial T} & \dfrac{\partial lnV_S}{\partial \Theta} \\ \dfrac{\partial ln(V_P/V_S)}{\partial T} & \dfrac{\partial ln(V_P/V_S)}{\partial \Theta} \end{bmatrix} \begin{bmatrix} \delta T \\ \delta \Theta \end{bmatrix} = \begin{bmatrix} \delta lnV_S \\ \delta ln(V_P/V_S) \end{bmatrix} \tag{10}$$

方程式（2）中假設溫度與蛇紋岩化為影響隱沒帶地區地幔楔的兩個主要之獨立因子。就其他因子來說，這是一個極度簡化的方程式，例如組成成分、破裂的存在以及熔融等因子，都可能影響速度與比例。方程式（10）可以看作參數域的旋轉，將原始的兩個參數投影成為兩個新的參數。因為（10）是個有唯一解的系統，參數的反演會將 δlnV_S 和 $\delta ln(V_P/V_S)$ 中的所有誤差，都投射到 δT 和 $\delta\Theta$ 中。

第四章　震源分佈

我們以不同深度的水平切面來呈現地震的分布位置（圖七）。最上層 20 公里內的地震，反映了菲律賓海板塊岩石圈以及上覆歐亞板塊間的應力，其分佈似乎亦與海溝系統的構造單元相關連。地震分佈與海溝平行的形式，反映了海溝在地形上的結構（圖二，*Font et al.*, 2001）。在沖繩海槽中，淺層地震分佈排列與弧後盆地的張裂軸線一致，並且明顯地指向延伸至台灣東北海岸（圖七，0-15 公里）。自深度 50 公里以下，地震的分佈可勾勒出隱沒板塊的幾何形狀。

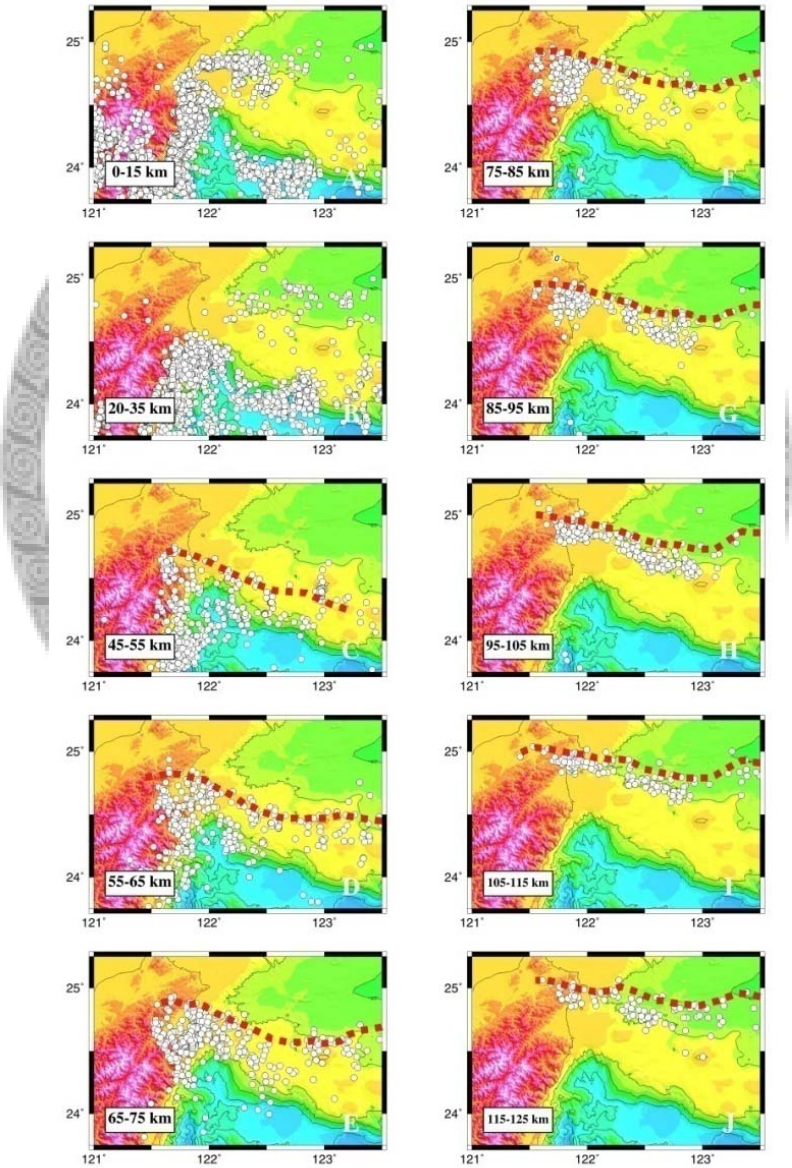

圖七　重定位後的地震深度剖面（空心點），深度間隔標示在每個圖幅上。等深線（黑點線）是取自圖四的三維隱沒板塊表面模型，選擇每個深度間隔的中間值。隱沒板塊等深線大致與琉球海溝的走向相同。然而在西側邊界，深度範圍 45-95 公里處，隱沒板塊顯示出與海溝反向的曲率（C 到 G）

4.1 建立隱沒板塊表面的三維幾何構造

為了看出隱沒板塊如何變形，我們以每隔 0.1°經度，每 10 公里深，選出分佈最北的地震，以代表隱沒板塊的上部邊界，並建立三維的資料組。明顯的偏差數據都會被剔除。以上作法的基本依據是建立在我們已經知道地震會發生在隱沒板塊表層的地殼內，這讓我們可以將之視為隱沒板塊表面的表徵。然後我們將這個資料組以 GOCAD 軟體建構一組吻合地震分佈的曲面（*Mallet*, 1989, 2002）。GOCAD 使用最小平方差的方式，在三維空間中以一個曲面去對應所有的點，並以最小曲度及最小梯度進行正則化。如果資料組中存在地震發生的間隙，那麼這樣的正則化過程將會填補這些間隙。我們同時嘗試了許多不同的方法來表現隱沒板塊的表面，包括不在一個狹窄的範圍選取最北邊的地震，反而以較大的範圍（每隔 0.25°經度），選取最北邊的 3 個地震，以及不移除明顯的偏差數據，再以 GOCAD 找出最吻合的曲面。兩種不同的方式均獲得相類似的隱沒板塊之幾何形狀，其結果是第一次以三維的表現方式呈現在圖八中。

藉由 GOCAD 所找到最佳的隱沒板塊表面之等深線，同時與震源分佈一起被繪製在圖七中 45 公里至 115 公里深的範圍，以顯示板塊如何沿著其走向褶曲。請注意在地震分佈的深度剖面中，部分深度的隱沒板塊表面與地震分佈邊界並不完全吻合，這是由於最佳曲面是以符合三度空間的地震分佈為依據，而非以每個深度間隔二維的地震分佈所求得。大約在東經 123°附近，有一群地震從隱沒板塊平均走向附近被推擠出來，似乎表現出存在地形上的特殊結構，例如海底山或是附近的加瓜海脊在此隱沒。但我們所定出的隱沒板塊表面，很明顯地略過了這些地震結構（例如圖七，45-55 公里）。隱沒板塊表面的等深線大致上平行海溝，除了彎曲在最西邊的 50 公里，介於深度 45-95 公里的範圍。這個構造相當顯著，主要是在於它彎曲的方向相對於整個琉球海溝的彎曲方向來說是相反的（圖八）。

為了檢驗這個構造是否足夠顯著，我們將每個地震的震源深度加入了 5 公里的亂數加以調整，再以同樣的步驟利用 GOCAD 將這組「受過污染」的資料組進行計算，找出最符合的曲面。結果，利用 GOCAD 所找到的新曲面，其最西側同樣顯著地可以看出板塊凸起的現象。如果這個凸起是因為地震定位錯誤所造成，那麼在最西側這 50 公里、深度數十公里範圍內所有的地震定位，都必須要系統性地向南邊移動 5-10 公里才行；但這個可能性相當小，主要是因為台灣陸地密佈的地震測站就在左近，自然對於此處的地震定位有相當嚴謹地控制。雖然

以肉眼觀察圖七與圖八的隱沒板塊凸起並不顯著，但這個凸起在沿著板塊走向的水平曲度κ_h，在彎曲的頂點可以達到 0.02 到 0.04 km^{-1}，遠大於琉球海溝西段三分之一的曲率 0 到-0.002 km^{-1}的「背景值」。相較於其他的參考值，即使是強烈彎曲的馬里亞那海溝，位於板塊走向的中點附近，其曲率的規模大小也只有 0.001 km^{-1}左右。在琉球隱沒板塊最西側所發現的這個曲率，不僅僅是它的規模大小異常，重點是它的曲率值和整個琉球海溝是異號的。根據我們在 4.3 分析，它特別短的的波長也是一項獨特的特徵。

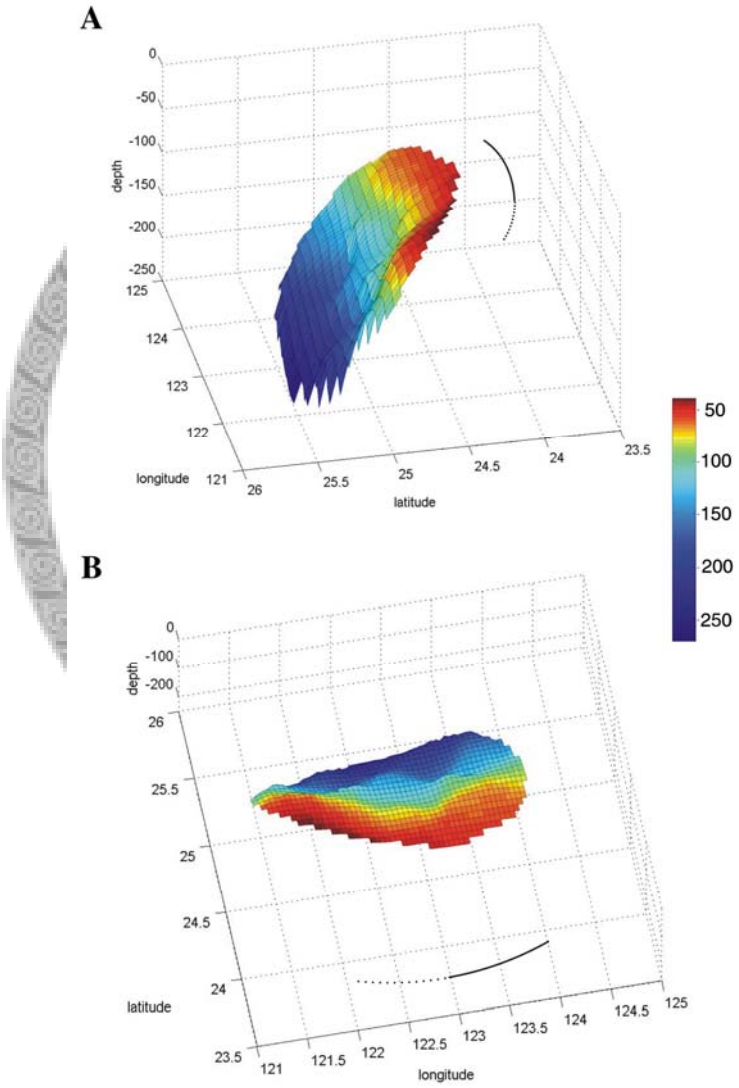

圖八　利用 GOCAD 軟體所合適出的三維隱沒板塊表面模型，顯示了兩個不同的角度。(a)從西北方看隱沒板塊表面，西側的褶皺區在中等深度造成了一個撓曲，導致其下的隱沒板塊傾角變陡。(b) 沿著隱沒板塊表面，並大致平行隱沒傾角，以南北向的方向觀看。相較於整個海溝的走向（實線與點線），兩個圖中西側邊緣的褶皺相當地明顯。

曲率與彈性彎曲應變之間的關係為$\varepsilon(z) = -(z - h/2)\cdot\kappa$，其中 z 是厚度為 h 的彈性板塊，從表面往下的位置。測量垂直於隱沒板塊傾角方向的κ平均值約 0.04 km^{-1}，並保守估計 h 為 15 公里，如此一來，板塊表層的應變$\varepsilon(0) =\sim 0.3$，對一個彈性板塊來說，這個值太大了。如果是連續的脆性破裂，可以允許比較小的彈性應變造成顯著的曲率，但是隱沒板塊上部顯示仍舊受到了水平的拉張，這與震源機制解所顯示東西方向壓縮、下隱方向拉張的結果（*Kao and Rau*, 1999; *Liang et al.*, 2004）彼此互相矛盾（詳見以下）。這暗示琉球隱沒帶最西側的隱沒板塊，其曲率所反映出的彈性性質，實際上是受到水平壓縮的影響，而非拉張。我們認為隱沒板塊的褶皺，是以黏滯性的大量延伸，所造成水平方向的凸起，其時間尺度則獨立於壓縮的脆性斷裂。我們會在第五段繼續討論這個機制，並以黏彈性方程式來探索可能的發生條件。

4.2 雙層地震帶與其力學特性

依照垂直於當地隱沒板塊的走向，我們切出了五個垂直剖面，其深度範圍介於 50-100 公里之間，呈現在圖五中。從垂直剖面上（圖九）可以清楚地看出，隱沒板塊在 A、B、C 剖面的 50 到 80 公里之間，在垂直方向上有很明顯的扭曲；同樣的扭曲在 D、E 剖面的深度卻是淺於 40 公里，以致於 50-150 公里間是一路往下隱方向直線分佈。根據圖八所呈現的三維模型可以得知，這個凸起其實就是上一段我們所討論到隱沒板塊在水平方向剖面所看到的褶皺，其三維結構的一部份。結果造成深度 80 公里以下的隱沒板塊傾角向西遞增。相對於 *Deschamps et al.*（2000）所報導加瓜海脊兩側隱沒板塊不同的平均傾角，本次研究所重新定位的震源分佈，其實是發現了加瓜海脊以西隱沒板塊的傾角變化。

在瓦達地班尼奧夫帶上的另一個主要特徵就是雙層地震帶，它出現在鄰近區域大部分的垂直剖面之中。沿著隱沒板塊的走向上，雙層地震帶的結構有一些重要的變化。相較於其他的剖面，雙層地震帶在剖面 B 當中特別不明顯，且延伸的深度也有所不同。這兩個層面看似在 C 剖面聚合，但這個聚合在每個位置都不清楚。一般來說，雙層地震帶的間隔約為 15-20 公里，深度範圍介於 40 到 80 公里。相較於日本東北底下的雙層地震帶（*Hasegawa et al.*, 1994），此處所向下延伸的深度較淺。同時也很難區別到底是雙層地震帶的上層或下層中的哪一層結束，哪一層又繼續向下延伸。根據 *Kao et al.*（1998）、 *Liang et al.*（2004）以

及哈佛中央矩張量（例如：Dziewonski et al., 1981）所定出的震源機制解，發生在雙層地震帶上下層的地震，主要都顯示出沿著隱沒板塊走向的壓縮作用，至少顯示了隱沒板塊破裂的部分是受到了一致的應力場所導致。從存在著沿走向的壓縮作用出發，例如剖面 A 和 B 的震源機制解，就同時存在與隱沒板塊平行及垂直的壓縮軸，這可能肇因於隱沒板塊變形顯著的當地應力改變。由於沿著走向的褶皺可以釋放壓縮作用，導致壓縮軸從平行隱沒板塊轉換為垂直隱沒板塊。除此之外，所有的震源機制解形式，都支持我們認定雙層地震帶以及隱沒板塊的褶皺，都是源自於相同的水平壓縮力量，且褶皺的發展主要是黏滯性的。

4.3 隱沒板塊的褶曲與麥斯威爾黏彈性板塊模型

注意在圖八中所呈現水平方向上的褶皺，相當明確地從 50 公里深向著下隱方向延伸，而非人為或偶然地在某個單一剖面及特定深度所出現的假象。其彎曲處的地震機制及規模暗示我們，隱沒板塊反應側向壓縮的方式同時具有彈性所造成的脆性破裂及黏滯性所發展出的大量彎曲。其中前者是以數秒為時間尺度，而後者則是以數十萬年至數百萬年長的時間為尺度。我們將這樣的變形狀況，以黏彈性層被置於黏滯性介質中來模擬，並透過控制層與介質間在岩相上的對比程度，以及以及彈性縮短或表面應變的大小，來觀察什麼樣特定波長的褶皺會在這樣的不穩定性中可以最有效率地生成。其中最關鍵的控制就是這個褶皺主要結構的波長 λ_d。根據對應深度的隱沒板塊等深線進行頻譜分析，可以得到 λ_d ~250 公里。我們也可以藉由測量褶皺的波峰（接近西側端點）與「背景」間的距離來估計 $\lambda_d/2$，或測量波峰與反曲點（$\kappa = 0$ 的地方）間的距離來估計 $\lambda_d/4$。所有的結果都互相吻合，顯示我們所估計的 250 公里相當明確。在附錄中，我們以麥斯威爾形式的黏彈性薄層褶曲以及相關的不穩定性問題，推導出控制方程。其褶曲方程式如下：

$$D_v \frac{\partial w''''}{\partial t} + N \cdot w'' + \tau_l \cdot N \cdot \frac{\partial w''}{\partial t} = -4k\mu_m \frac{\partial w}{\partial t} - 4k\mu_m \tau_l \frac{\partial^2 w}{\partial t^2} \qquad (11)$$

式中 w 層面撓曲程度，t 是時間，w'''' 代表 $\partial^4 w/\partial x^4$，且 x 平行層面，N 為垂直於 x 的每單位所受平行 x 方向之水平壓縮力，D_v 層面的黏滯剛度，τ_l 為麥斯威爾褶曲層的舒緩時間，μ_m 為介質或上部地幔的黏滯性，以及 k 為波數介質黏滯阻力的褶曲。其他參數請見附錄的解釋。

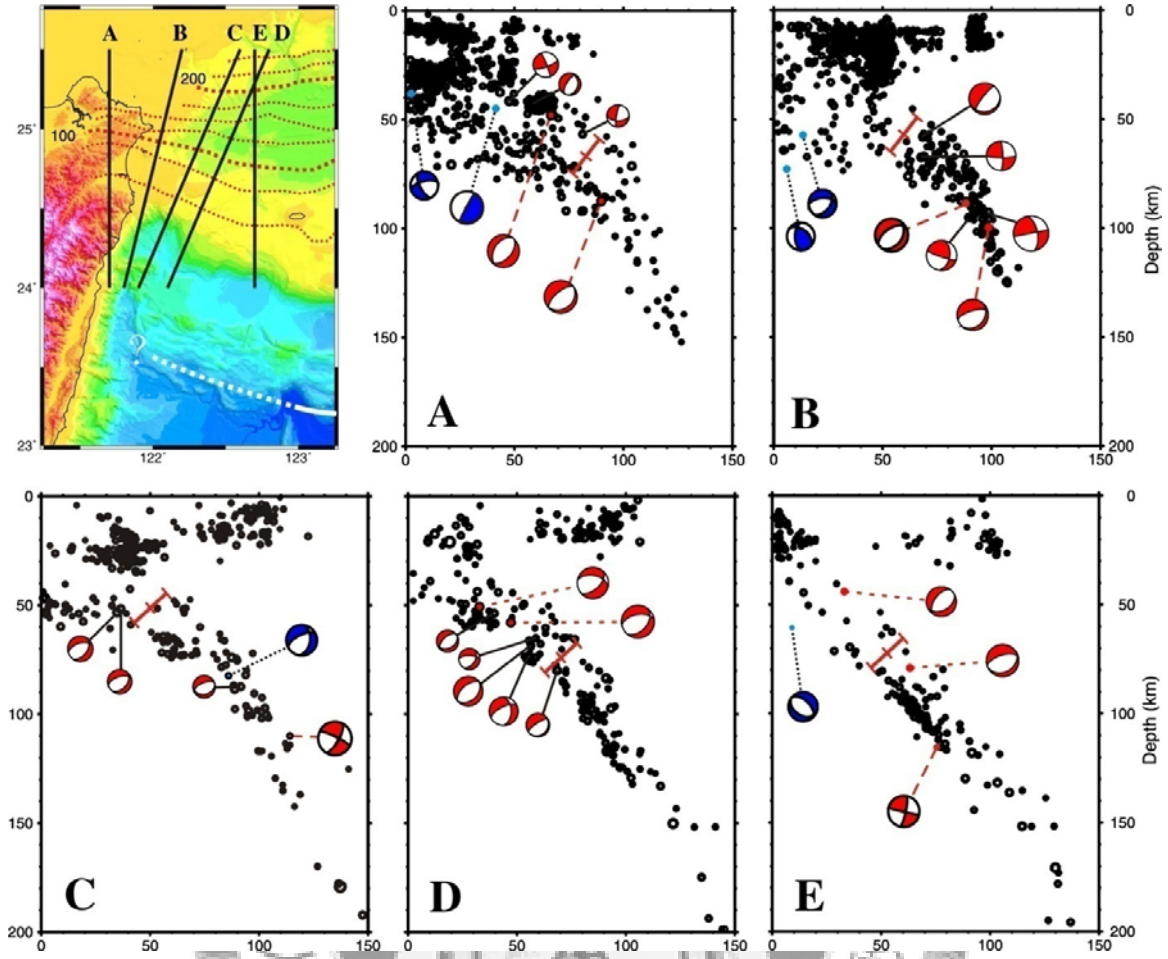

圖九　瓦達地班尼奧夫帶的垂直剖面，剖面位置畫在左上角圖中。左上角圖中的粗細黑點線代表隱沒板塊表面的等深線，取自圖八的三維模型，且每個剖面都是以垂直隱沒板塊走向的方向，並呈現淺部的地震分佈（小於 100 公里）。白色實線與點線表現琉球海溝的位置，與圖一相同。在剖面 A、B 和 C，隱沒板塊很明顯地在垂直方向上，深度 50 到 80 公里間呈現彎曲／反彎曲，在這之下的傾角相較於剖面 D、E 要來得大。雙層地震帶的型態大體上每個剖面都不盡相同，但整體來說兩個層面相距約 15-20 公里，圖中以 20 公里的比例尺與 10 公里的標示做為比對。側投影的震源機制解包括 *Liang et al.,*（2004）（實線連結）、*Kao and Rau*（1999）（虛線連結）、以及哈佛資料庫（點線連結）的結果，都一致顯示沿走向東西排列的壓縮成分，位在 50 到 100 公里深度範圍（壓縮軸位在白色的部分），只有些微的變化。雙層地震帶則是自海岸向外海延伸至少 100 公里。

隨著附錄所推導出的結果，證明麥斯威爾層在褶皺時，有兩個不穩定的組成都是時間指數的函數：當 $\omega_1 > 0$ 時，$\exp(\omega_1 \cdot t)$ 是不穩定的，且會隨著時間而放大；當 $\omega_2 < 0$ 時，$\exp(\omega_2 \cdot t)$ 則是穩定的，且會漸漸消失。放大率 $\omega_{1,2}$ 是層面的黏滯性與介質黏滯性比值 $\gamma = \mu_l / \mu_m$ 、等量的彈性表面應變 $\varepsilon_N = N/(E_l^* h)$（見附錄）、以及每個褶皺單元的波數 k （或波長 λ）的函數。因為我們假設所觀察到的大幅度褶皺是肇因於不穩定性的緣故，我們於是聚焦於 ω_1 為波長的函數。圖十 a 和 b 中呈現了在不同的 γ 和 ε_N 之下，沒有維度的放大率 $\omega_1 \cdot \tau_l$ 對比 λ/h 的結果。放大函數的峰值標示出了最傾向形成的褶皺之模型主要波長 λ_d^{mod}/h。

為了建立起主要波長 λ_d^{obs}/h 的觀察做為目標模型，我們需要估計 h。因為雙層地震帶的間隔為 15-20 公里，隱沒板塊的孕震厚度於是可能大於 20 公里（圖五）。然而 h 是代表黏彈性層的有效力學厚度，這個厚度通常小於岩石圈的孕震厚度（*Cochran*, 1979; *Wiens and Stein*, 1984）。結合過去對於海洋岩石圈的重力、地形與力學模型分析，這個厚度應介於中洋脊附近小於 10 公里（*Cochran*, 1979; *Kuo et al.*, 1986）到年老海盆的 20-30 公里（*Caldwell et al.*, 1976; *Watts*, 1978）。我們假設 h 下限為 15 公里，以部分反應相較於隱沒之前的岩石圈，隱沒板塊受到加熱的事實，並設定上限為 30 公里。因此 λ_d^{obs}/h 的範圍就是 8.3-16.7（圖十）。

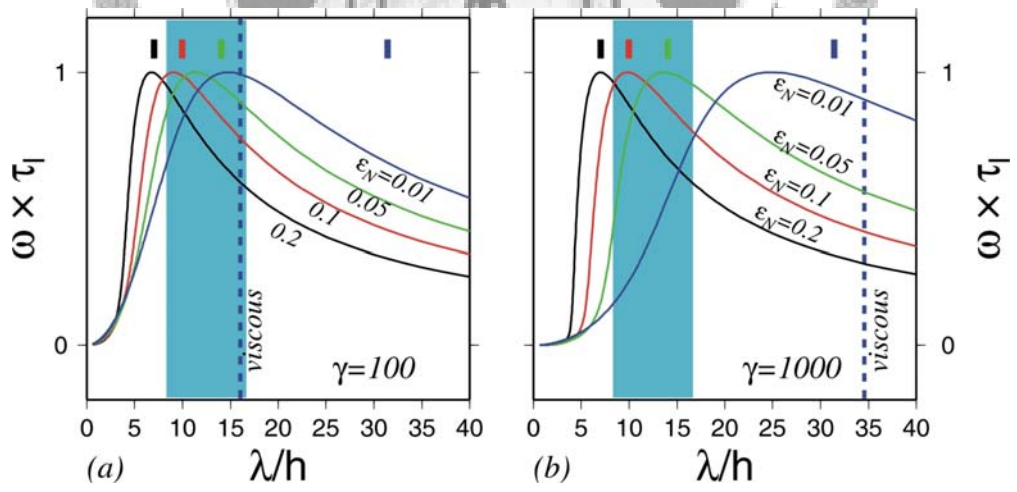

圖十　預測無維度化的放大係數 $\omega_1 \times \tau_l$ 是為波長的函數，在（a）$\gamma = 100$ 以及（b）$\gamma = 1000$ 的條件下，並考慮彈性應變 ε_N =0.01（點線）、0.05（短虛線）、0.1（長虛線）以及 0.2（實線）。放大函數以標準化為 1。黏性層的主控波長（垂直點線）只是 γ 的函數，當 ε_N 很小的時候，與黏彈性層相仿。彈性撓曲的波長為 ε_N 的函數，並以垂直短粗線從左到右分別標示 ε_N =0.2、0.1、0.05 和 0.01。在 γ = 100（或更小）的條件下，純黏滯性褶皺勉強可以解釋觀測的結果（陰影區），而純彈性隱沒板塊則需要應變>0.04。兩者都很難解釋隱沒板塊的應力狀況。

圖十比較了觀察結果的所有模式。若是層面的黏滯性較高，就需要有較強的壓縮，γ 較大 ε_N 就必須較大，反之亦然，如此才能維持 λ_d^{mod}/h 在觀察範圍內。較大的 ε_N 可以同樣由較大的 *N*、較小的 *h*、以及較低的楊氏模數獲得；但這其中任何一個參數，目前都沒有足夠的地球物理觀測控制。然而，應變是受限於隱沒板塊以地震發生所定義的屈服包絡面。因為根據海洋岩石圈在深度數十公里處的摩擦定理所推得壓縮屈服強度約是在 500 MPa 的數量級（例如：*Kohlstedt et al.*, 1995），以及一般接受的楊氏模數範圍為 $10^{10}-10^{11}$ Pa，彈性應變的範圍則從非常小到 0.05。我們特別考慮把 0.05 當作 ε_N 的最大值。由於隱沒板塊在持續插入上部地幔的淺層時，並沒有破裂或強烈褶皺，可見隱沒板塊的黏滯性沒有達到這麼大。我們假設 $\gamma \geq 10$（如下所示）是被 λ_d^{obs}/h 值的下限所排除。可被接受的模型參數組可以在 $\gamma-\varepsilon_N$ 圖中，被 λ_d^{obs}/h =8.3 和 16.7 以及 ε_N =0.05 所為起的範圍內（圖十一）。例如，一個隱沒板塊的黏滯性是其所處上部地幔的一百倍，且其水平彈性應變為 5%並褶皺成為主要波長為 250 公里時，其有效厚度則略大於 22 公里左右（ λ_d^{obs}/h~11.4）。

純粹的彈性或黏滯性褶皺是否有可能解釋我們所觀察到的主要波長呢？我們可以將麥斯威爾層的 $\tau_l \to \infty$ 而降低成為一個彈性層（詳見附錄），在此情況下主要波長會減小，而 ε_N 則增加（圖十）。對同樣的 ε_N 來說，彈性層會產生比麥斯威爾層更寬的褶皺。要將彈性板塊褶曲成為我們所觀察到的波長，ε_N 就必須是 0.04 或更大。當然這個值其實是可以被接受的，但地表上的彈性褶曲並不吸引人，主要是因為拉張的彎曲與整個隱沒板塊厚度範圍中完全是壓縮的震源機制相互矛盾的緣故。另一方面，當 τ_l=0 時，我們可以得到一個黏滯性的層面。其主要波長大約相當於在 ε_N 很小情況下的麥斯威爾層（圖十）。這表示彈性的部分協助了隱沒板塊在水平縮短過程中，較短波長的褶皺。黏滯性的褶皺傾向較小的 γ 值（圖十 a），且同樣無法以彈性來解釋隱沒板塊中的地震及其壓縮性的震源機制解。

4.4 黏彈性板塊模型中參數的不確定性

由於黏彈層的方程式是個簡化的方法，再加上我們對於模型參數的瞭解相當有限，因此我們無法更進一步地將模型參數的可能範圍縮小。取而代之的是，我們選擇畫出一個較寬的模型可接受範圍，以探索 γ 和 ε_N 間的取捨效應，並將這

個議題保持開放，直到我們可以取得更新的獨立控制結果。對於一個強硬的隱沒板塊來說，其黏滯性比地幔大三個以上的數量級，且其平面內的彈性應變ε_N至少要在 0.04 以上，才能解釋觀察到的波長（圖十一）。對於一個較軟弱、或是γ較低的板塊來說，由於我們對 *h* 的瞭解有限，因此隱沒板塊可能的應變會有較大的範圍。而一般認為γ等於 100 是為其可能性的下限（*Houseman and Gubbins*, 1997; *King*, 2001; *Billen et al.*, 2003）。有一個實用的方法是根據牛頓流體的動力模型以及冪次定律的黏滯性，推論地幔溫度每下降 100°C，就會導致 0.5-1 個數量級的黏滯性增加（例如：*Christensen*, 1989; *Lin et al.*, 2002）。若是γ等於 100，則相當於在牛頓流體內 200°C 的溫度對比，或是相當於非牛頓流體內 400°C 的溫度對比。根據 *Yamasaki and Seno*（2003）所建構琉球隱沒帶的溫度結構，僅僅 200°C 的溫度異常恐怕無法吻合其結果。雖然 400°C 看似一個可以接受的結果，但我們至今對於隱沒帶地區的非牛頓流體效應卻仍舊不甚瞭解。或許ε_N是未來最有可能有更進一步控制的參數。根據地震學的觀點，藉由估計隱沒板塊所受彈性應變的大小，應該是解答我們模型空間可能解區域的有用步驟（例如：*Bevis*, 1988）。

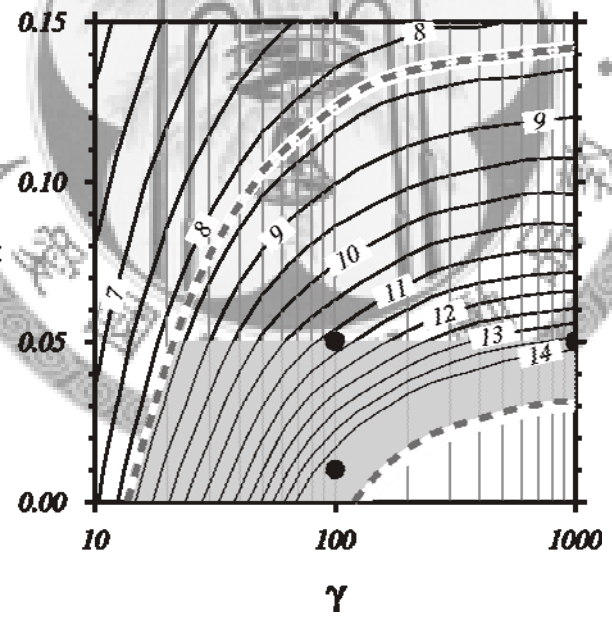

圖十一　本研究中所考慮的麥斯威爾黏彈性模型其可能的參數範圍。實線等值線是主控波長對厚度進行無維度化後的值。陰影範圍是由最大可能的彈性應變ε_N為 0.05，以及觀測波長的可能邊界 8.3 和 16.7（虛線）。隱沒板塊與周圍的地幔必須要有更大的黏滯性對比才能允許更高的應變；γ 較小時，應變的可能範圍就會很大。其解在文字中均有討論，例如：γ=100，ε_N=0.01 和 0.05 以及γ=1000，ε_N=0.05 都以實心圓圈表示。未來需要獨立的控制或參數來縮小可能的範圍。

在中等深度（40-150 公里）的雙層地震帶，也已經在好幾個隱沒帶中被觀察到（例如：*Hasegawa et al.*, 1978; *Abers*, 1992; *Kawakatsu*, 1986; *McGuire and Wiens*, 1995）。其中上層地震被認為是發生在海洋地殼之中，且已經被普遍接受的想法是由於玄武岩-榴輝岩轉換過程所造成（*Kirby et al.*, 1996; *Peacock and Wang*, 1999; *Peacock*, 2003）。有少數理論持續提出引發下層地震的機制（請見 *Yamasaki and Seno*, 2003），其中將蛇紋岩化隱沒板塊地幔脫水並脆性化的作用（*Seno and Yamanaka*, 1996; *Peacock*, 2001），則符合本研究所討論的深度。在 *Yamasaki and Seno* （2003）的研究結果中，就針對這些變質反應的空間分佈與雙層地震帶的幾何形狀進行了全球性的普查。在他們位於臺灣東北下方的剖面中，雖然計算結果中兩層脫水反應的間距約 20 公里確實符合我們的觀測，但其實雙層地震帶與預測中的脫水位置之關連性並不清楚。

有研究認為，岩石圈在隱沒時其上部大型破裂斷層（通常形成於外部隆起）所釋放的水，會向上滲透而造成地幔蛇紋岩化（例如：*Peacock*, 2001）。藉由追蹤相對的板塊運動方向，其中可能隱沒到目前雙層隱沒帶的，是鄰近東南側的菲律賓海板塊（圖二），該處在近期只發生過少數大型的外部隆起地震。唯一一個被紀錄在哈佛中央矩張量表單中的，是一個規模 5.7 的正斷層地震，標準中心深度為 15 公里，其震源深度大約在 10 公里左右。不過隱沒板塊內部的蛇紋岩化是否可以因為像這些少數的外部地震而變得容易，仍不無疑問。雖然現地的岩石圈影像可以提供是否有深切斷層存在的證據（例如： *Ranero et al.*, 2003），但在琉球海溝的外部隆起區域目前並無相關結果。意即這個區域目前仍缺少關鍵性支持的證據，來支持脫水造成脆性化的作用發生。

Kao and Rau（1999）以果醬三明治型態，類似大陸岩石圈的岩相來解釋外海地區雙層地震帶的的地震形式。雖然海洋岩石圈的岩相在未來也許有著相當的重要性（例如：*Wang and Rogers*, 1994），但以大陸岩石圈類比海洋岩石圈的繪圖，仍舊是相當冒險的。其中海洋地殼下部的柔軟性迄今仍有爭論（*Kohlstedt et al.*, 1995; *Escartin et al.*, 1997; *Hirth et al.*, 1998）。像是相似於地震的微地震，其規模可以大到 4，亦常見於沿著中洋脊的下部地殼中成群出現（例如：*Wolfe et al.*, 1995; *Bergman and Solomon*, 1990）。最重要的是，在本研究中最明顯可以辨認出雙層地震帶的深度（40-50 公里以下），如果沒有受到孔隙壓提高的幫助，高靜岩壓會阻止脆性破裂的發生（例如：*Kirby*, 1995）。在喀斯開南部岩相的解釋，原本

亦是針對隱沒板塊所提出（*Wang and Rogers*, 1994），但其雙層地震帶的分佈是在相當淺的深度（10-25 公里）。另一個不確定的因子則是海洋地殼的厚度。在本研究中，雙層地震帶 15-20 公里的間隔，若是根據 *Kao and Rau*'s （1999）的模式推論，隱沒板塊會有一大片區域其海洋地殼的厚度要比正常（約 7 公里厚）厚 2 到 3 倍。時至今日，並沒有任何地震學上的證據，足以說明菲律賓海板塊有如此的厚度（*Wang et al.* 2004b）。考慮地殼由於岩漿形式或力學形式地增加 2 到 3 倍，也被認為不大可能發生。且相較於喀斯開南部隱沒帶，其雙層地震間隔只有不到 10 公里（*Wang and Rogers*, 1994）。 推測臺灣-琉球碰撞帶的雙層地震帶發生原因，恐怕還需要更多強力的證據才行。

第五章　震波層析影像

不同於日本、阿拉斯加與喀斯開地區震波層析影像的研究，擁有較佳的地震與測站分佈。本研究即使聯合部分日本氣象廳觀測網路也只能提供有限的觀測範圍，來對隱沒帶北側的地幔楔提供控制。我們的策略是呈現一個針對資料所能提供的模型，同時不過度解釋或膨脹資料的解釋能力。V_P和 V_S的變異下降分別在 70%及 60%以下，已經低到足以壓抑模型中不確定以及次要的特徵。我們並不解釋任何位在 *R*25 限制之外的區域，並且小心不過度解釋 *R*25 限制區域內微小或尺度小於不均向性解析能力的構造。在實務上，我們對於能夠清楚解析琉球隱沒板塊的剖面較有信心，換言之，要能夠顯示連續的高 V_P和 V_S異常。例如經度 121.8°E 的剖面，就是本研究所討論的焦點所在。

根據最佳化的壓抑係數，我們所得到的層析影像模型結果顯示，這個區域中最主要的特徵就是與琉球隱沒板塊相關連的高V_P和V_S異常，並向下延伸到 150 至 200 公里深（圖三）。我們繪製的 *R*25 等值線是代表 25%解析能力的範圍，以表示我們對解析較佳區域的解釋具有信心。請注意 *R*25 並不保證這些特徵現象一定「正確」，但這對哪些特徵現象值得我們進一步檢測或可以直接忽略具有指標作用。由此可見，只有隱沒帶以及淺層的地幔楔是值得解釋的（圖三）。除此之外，根據附錄中所進行的復原測試，顯示在地幔 *R*25 的區域中，可解析的不均向性尺度約為 10-20 公里。

5.1 震波層析影像的解析能力

從棋盤檢定的結果來看，顯然我們的壓抑係數有效地去除了由於缺乏採樣之區域所造成人為結果的可能性，但我們也因此損失了部分解析能力邊緣區域的構造結果。圖十二和圖十三呈現了兩種不同格點大小的還原試驗結果。整體來說，一個格點大小的解析能力向東迅速減弱，但兩個格點大小的解析能力則相對維持較佳的水準。在鄰近臺灣的剖面，地殼的不均一性解析能力約為 10 公里，弧前地幔約為 10-20 公里，整個隱沒板塊則約為 20 公里。在不考慮深部隱沒板塊的條件下，靠東側剖面的解析力大約是在 20 公里左右。至於火山前緣底部至深部地幔楔的解析力則是介於很差到完全沒有之間。

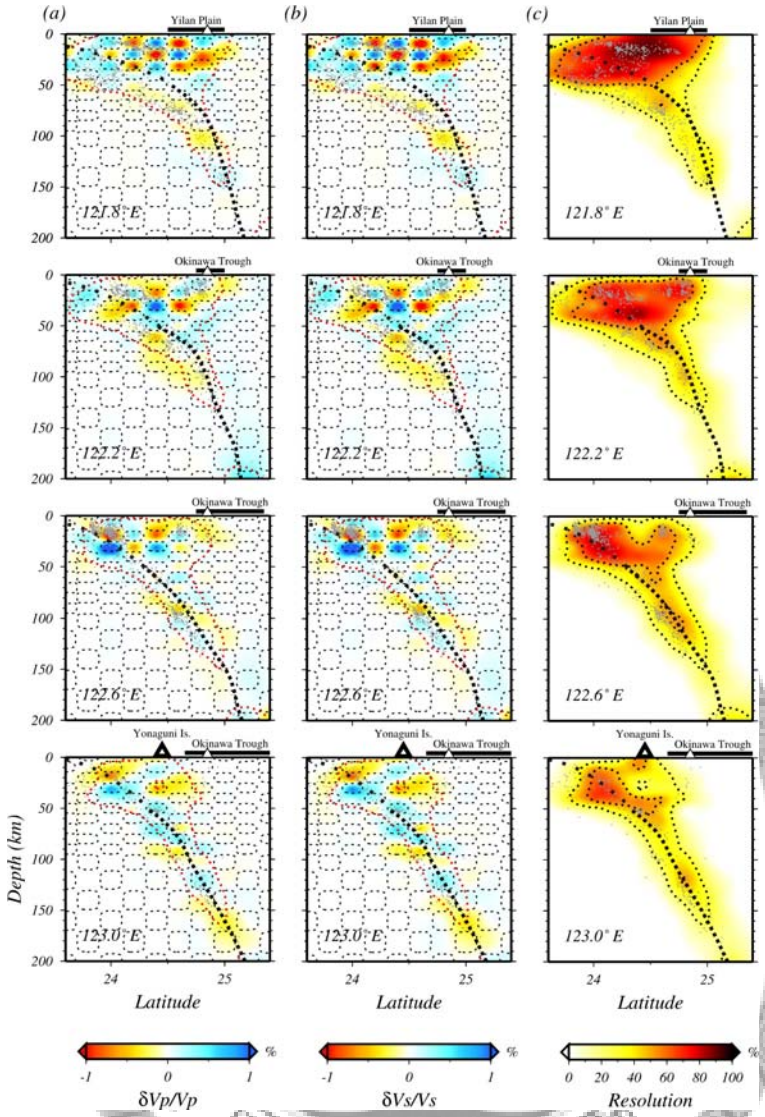

圖十二　棋盤檢定結果 I。(a) 和 (b) 為速度異常，(c) 則是 V_P 之解析力矩陣的 R 值分佈。在深度 100 公里以內，格點間隔為 0.2° 乘上 0.2° ，深度間隔為 10 公里，其外框以黑色虛線描繪。超過深度 100 公里的部分，格點間隔為 0.2° 乘上 0.2° ，深度間隔為 20 公里。在 (c) 中所繪的是 R 為 25%及 50%的等值線，並將 25% (R25) 的等值線以紅色虛線繪於 (a) 及 (b) 中。要注意的是在 R25 區域邊緣以及較東側的剖面上，比較會出現一些模糊或相反的異常結果。

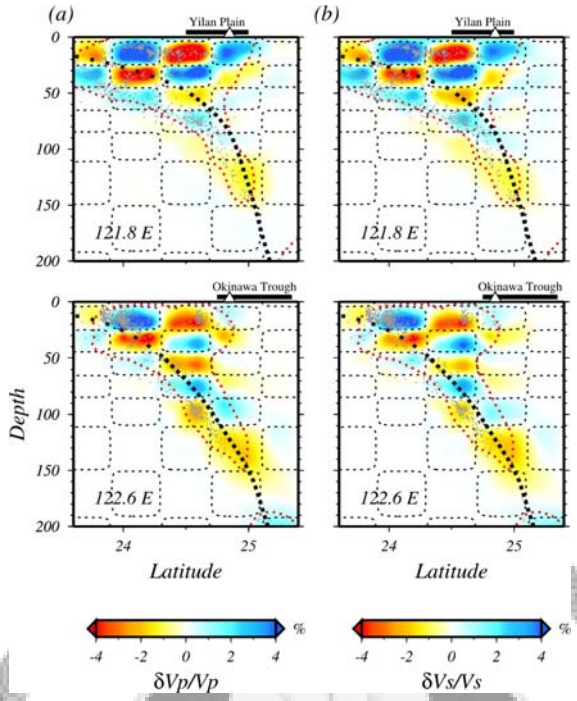

圖十三　棋盤檢定結果 II。相同於圖十二的棋盤檢定結果，但格點間隔加倍，並呈現部分剖面。大部分具有解析能力的區域均落在 R25 範圍之內，但同樣越往東側解析度越差。

在圖 A1 及 A2 中，西側剖面深度淺於 50 公里的區域，由於測站與地震資料的控制較佳，其 R 值均大於 0.5。本研究中根據弧前地區 V_S 及 V_P/V_S 異常異常而解釋為高蛇紋岩化的區域（圖十四，121.8°E 剖面），則落在 R 為 0.5 的等值線上。大部分深度淺於 100 公里，緊鄰隱沒板塊之上的地幔楔，則需要有 R 為 0.25 以上作為可信賴的標準。我們選定以 R=0.25 ($R25$) 作為模型中可解析部分的門檻，並謹慎地解釋在此區域中值得注意的速度異常構造。由於 R 值是根據反演之前的射線幾何所決定，而這些射線很可能會因為資料中的誤差而被影響，因此我們建議將 R25 視為一個微弱的門檻值。

5.2 隱沒板塊與地幔楔的構造特性

三個不同的垂直剖面中，圖十四 a 和 b 表現了我們模型中典型隱沒帶地區的影像。在最靠近海岸，沿著經度 121.8°E 的剖面，解析出隱沒板塊有 2%的速度差異，並且連續地從 50 公里向下延伸到 100 至 150 公里深。若是往東前進，則隱沒板塊的影像就漸漸變得不連續，或是以非常弱的的強度（<1%）連續。隱沒板塊的影像在 122.2°E 和 122.6°E 的剖面中，深度 100 公里之下，被沒有異常或是低速異常的區域給截斷，這可能是由於地震與測站分佈不均所導致的誤差，或者解釋為隱沒板塊在物理性質上的斷裂。深度 150 公里以下，地震變得稀少的地區，正異常值也變得微弱（圖五）。在經度 121.8°E 的剖面，在緯度 24°N 之下 40 到 50 公里深的地方，存在有一個負異常切穿淺層的隱沒板塊。這正好是位在一大片 10 公里尺度解析度較低的區域（圖十二），且最大的異常值正好出現在隱沒板塊表面，地震分佈相對較少的區域。這個異常的強度是單獨由 V_P 和 V_S 所解出來，並導致 V_P/V_S 的異常以及參數化的模型，將在下一段討論。到目前為止，我們仍未完全瞭解這個異常的由來，我們也將不會在本研究中加以解釋。

一般來說，隱沒帶地區 V_P 和 V_S 的異常，就比例大小上來說是類似的，這符合其速度異常主要是來自於溫度差異的原因。在經度 121.8°E 的剖面，有強烈的 V_P 和 V_S 負異常分佈在宜蘭平原附近的下方（圖十四 a 和 b），且這個區域的地震分佈明顯較少。若是考慮沖繩海槽目前被認為持續向西推進，並已經抵達宜蘭平原底下的情況（*Sibuet et al.*, 1987），這個負異常以及缺少地震發生的現象，或許可以解釋為相對較熱的下部地殼與最上部地幔，因而造成區域性拉張的構造活動。但若是越往東邊，沖繩海槽發育較成熟的地區，這個低速異常的構造與沖繩海槽的關連性反而變得不明顯。主要是因為沖繩海槽與活動火山前緣的分佈漸漸往北，超出了我們中央氣象局與日本氣象廳有效覆蓋區域的最北緣所致（圖五和圖十四）。

由於隱沒板塊被認為是最主要的結構，因此一個可靠的模型就應該呈現出合理的隱沒板塊影像，並且只有在隱沒板塊影像合理地被呈現，同一個剖面中的其他特徵才值得解釋。由於經度 121.8°E 剖面的隱沒板塊可以被連續地解析出來，並具有合理的速度異常，因此我們接著聚焦在這個剖面上進行討論。關於 V_P/V_S 正異常值最系統性的分佈模式，就是與隱沒板塊並列（圖十四 c）。這個主要特徵從隱沒板塊內的 V_P 和 V_S 異常，移動到隱沒板塊之外的 V_P/V_S 異常現象，

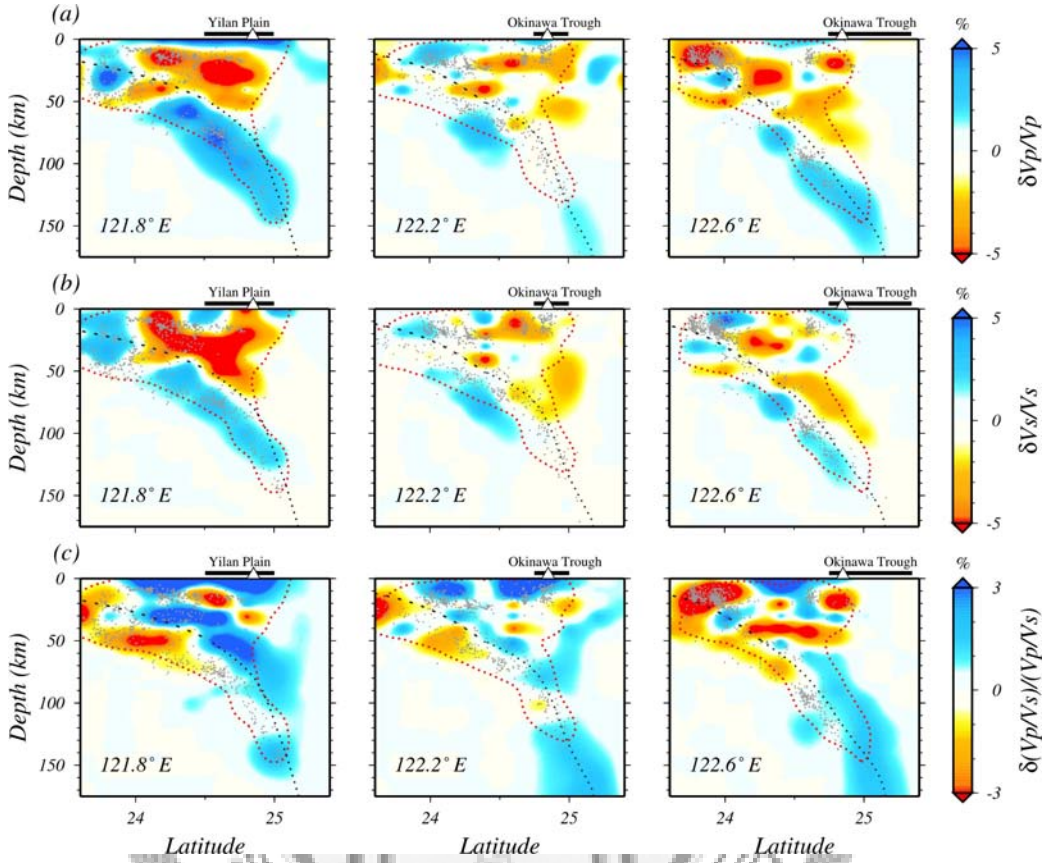

圖十四　層析影像結果（a）$\delta V_P/V_P$、（b）$\delta V_S/V_S$、以及（c）$\delta(V_P/V_S)/V_P/V_S)$ 沿著經度 121.8、122.2 和 122.6°E 秀出三個垂直剖面。V_P 的 $R25$ 繪製在每個圖上（紅色點線），指明反演結果可接受的極限範圍。黑色點線是平滑過的隱沒板塊表面 *Chou et al.*（2006），短虛線則是將介面延伸至地表面的琉球海溝。相關的板塊構造單元被註明在每一張圖的頂端。小三角形代表活躍火山前緣。注意只有經度 121.8°E 剖面的隱沒板塊結構可以較完整地被解析出來。

相當引人注目。根據合成測試的結果顯示（圖六），V_P和 V_S的壓抑參數選擇，可以壓制住假的 V_P/V_S特徵被放大，因此模型中所出現的這個結構應該是值得信賴的。地幔楔中發現 V_P和 V_S沒有異常到負異常的分佈，伴隨 V_P/V_S相當高的異常現象，曾經在日本隱沒帶（*Kamiya and Kobayashi*, 2000）、喀斯開隱沒帶（Cascadia subduction zone, *Zhao et al.*, 2001）以及安地斯隱沒帶（Andes subduction zone, *Graeber and Asch*, 1999）的層析影像中被報導。*Lin et al.* （2004）同樣也報導了東北臺灣底下，深度 60 公里的模型底部，存在低速及高 V_P/V_S的現象。高 V_P/V_S與相對低的 V_P和 V_S同時存在的現象，已經被廣泛地解釋為地幔水合或原地熔融的表徵。海洋地殼隱沒過程所釋放出的水，可能會被鄰近的地幔橄欖岩（peridotite）所吸收，而轉換形成蛇紋岩（serpentinite, *Hacker et al.*, 2003）。這個蛇紋岩層如果被角落流（corner flow）往下拉扯，最後又會被脫水，其水通量（water-fluxed）可能導致地幔楔的部分熔融（例如：*Hattori and Guillot*, 2003）。如果地幔楔足夠熱，隱沒地殼所釋放出來的水就可以使得地幔容易熔融，而不需要蛇紋岩化這個中間步驟（*Arcay et al.*, 2005）。

5.3 溫度異常與蛇紋岩化的程度

圖十五 a 和 b 顯示根據第一參數組所產生沿著經度 121.8°E 所得到的δT和Θ結果。由於蛇紋岩化僅應用在橄欖岩上，且溫度係數亦是針對典型淺部地幔的狀況，因此我們的討論主要集中在模型中地幔的部分（例如：＞40 公里）。首先，溫度是主要影響琉球隱沒板塊速度變化的原因，參數δT基本上與 V_S的變化模式一致。沿著隱沒板塊，δT降低到-200 到-400°C 的範圍（圖十五 a），這與一般簡單的隱沒帶溫度模型在 100-200 公里範圍內的結果相吻合。

蛇紋岩化主要發生在鄰近隱沒板塊介面的弧前地幔（圖十五 b），至於那些向下延伸超過 *R*25 範圍的部分則不在此討論。若是在方程式（2）中不考慮蛇紋岩化的參數，那麼弧前區域的低 V_P和低 V_S就會被認為是高溫。但現在這個區域就會被認為是正常或低溫的區域。雖然只有正的Θ有意義，但方程式（2）的右側還是會轉換出有正有負的Θ。例如在緯度 24°N 之下 50 公里深處，就有負的Θ （圖十四）。如上所述，我們並不確定蛇紋岩化對速度影響的顯著程度，且嚴格來說，方程式（2）只能夠將真正發生蛇紋岩化的地區的蛇紋岩化加以定量，並確實加以解析。

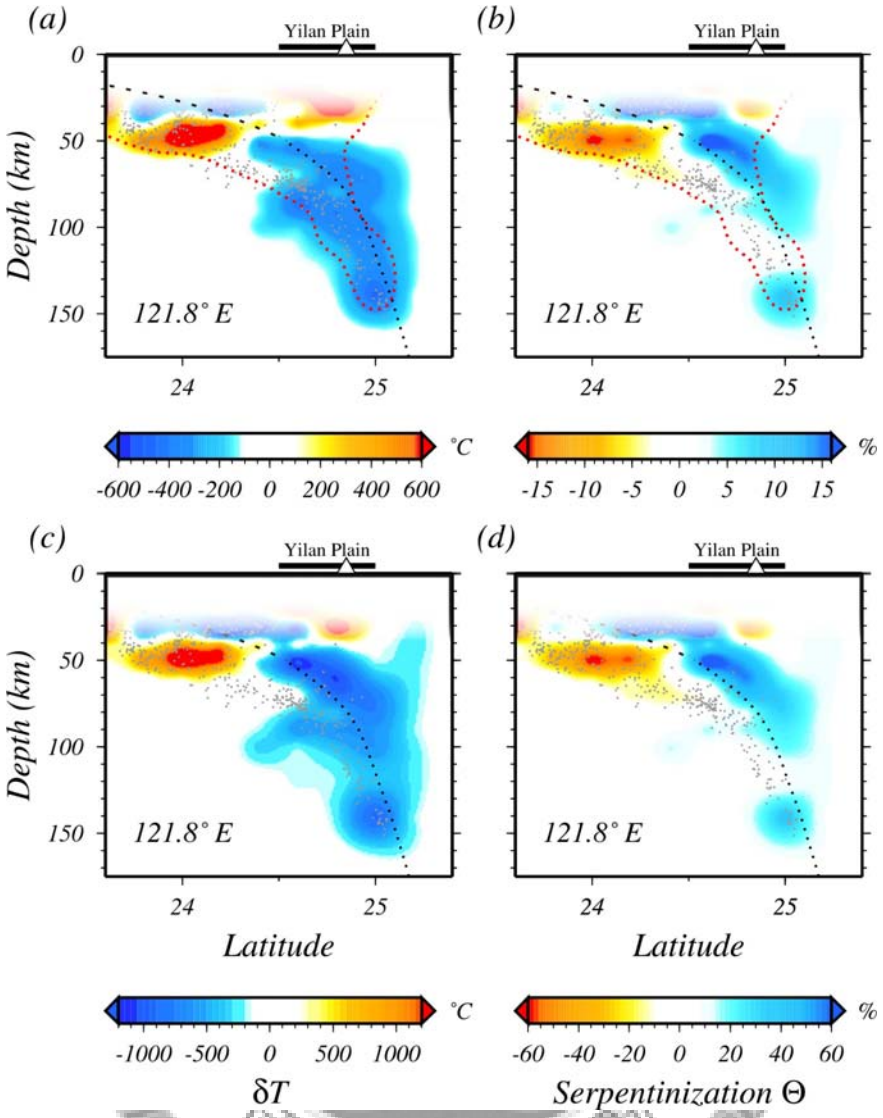

圖十五　上排為經度 121.8°E 剖面，根據第一組參數Θ的微分導數及方程式（2）所得到（a）溫度差異及（b）地幔中蛇紋岩化的程度。隱沒板塊平均比周圍冷 200-400°C。最顯著的蛇紋岩化區域是在隱沒板塊介面之上的弧前地幔。淺於 40 公里的模型並不具有意義，因此將之漸漸淡出至表面。大約在緯度 24°N 附近，淺層隱沒板塊段落出現負異常的原因仍未知。紅色細線所標示為 *R*25。下排為根據第二組參數Θ的微分導數，其餘同上排所得到（a）溫度差異及（b）地幔中蛇紋岩化的程度。溫度最小值在弧前地區達到不合理的-1000°C。

第二組參數的應用則得到了不同的溫度與蛇紋岩化模型（圖十五 c 和 d）。由於 V_P/V_S 的微分導數比第一組參數降低了四倍，因此Θ也就增加了四倍，換言之在弧前地幔達到約 60%的程度。而溫度則是在弧前地幔，Θ為最大的地方出現最小值，而非出現在隱沒板塊內。這個極端冷的弧前可能是肇因於太高的Θ就不須要太低的 V_S，於是溫度降低才能夠符合較低的 V_S。要判斷哪一組參數才是對的，這已經超過了本研究的目的，但就區別δT和Θ的能力來說，第一組參數似乎較能將隱沒板塊與弧前地幔做出區隔，並吻合我們對隱沒帶的基本知識（例如 *Van Keken et al*., 2002）。這兩組蛇紋岩化的參數應該繼續由其他層析影像的模型來進行測試（詳細討論請見 7.3）。

蛇紋岩化對地幔楔的解釋目前各地皆然。在東北日本，根據接收函數影像的結果認為，有一長串蛇紋岩層位在太平洋隱沒板塊之上，深度從 90 到 130 公里以下（*Kawakatsu and Watada*, 2007）；在日本中部，區域性較高的 V_P/V_S 在淺層緊鄰隱沒板塊的表面被發現（*Kamiya and Kobayashi*, 2000）。從活躍火山前緣的位置來判斷，正Θ在弧前分佈，沿著隱沒板塊的介面，最大可以達到 50 公里深。這也許和持續破裂的含水礦物相關，換言之，玄武岩中的硬柱石、綠泥石、黝簾石和角閃石會在玄武岩—榴輝岩變質反應中轉換並釋放出水，直接造成其上的地幔產生水合（*Van Keken et al*., 2002; *Iwamori*, 2007）。這讓人回想到喀斯開地幔楔的反射證據提供了弧前區域，深度 30-50 公里處，強烈蛇紋岩化的現象（*Bostock et al*., 2002）。地質上關於弧前蛇紋岩化的證據也在海洋與大陸聚合的邊界上被發現（*Fryer et al*., 1999; *Guillot et al*., 2000）。在本研究中，因為層析影像的解析度向東漸漸遞減的緣故，使我們無法議論蛇紋岩化是否沿著島弧分佈。

相較於其他觀察，弧前的蛇紋岩化是否能在未來被加以檢測呢？層析影像可以藉由於沖繩海槽中施放海底地震儀而改善，但同樣以震波速度為基礎的方法，可能會獲得與本研究類似的結果。一個關鍵性的檢測可以藉由震波衰減層析影像來獲得。在阿拉斯加與喀斯開地區底下的弧前地幔，藉由陣列波形的控制，得到低衰減（或是高 Q 值）的特徵結果，而被認為是低溫所造成的結果，這也吻合了地表所測得熱流值較低的觀測（*Schurr et al*., 2003; *Stachnik et al*., 2004）。目前跨越沖繩海槽的 Q 值模型與熱流測量都還付之闕如，這在未來將會是對於蛇紋岩化假說的一個關鍵檢測。

5.4 熔融現象與蛇紋岩化

如果溫度高於含水礦物在蛇紋岩中的穩定場，則蛇紋岩化就不會在第一個位置發生。自由狀態的水會使得水通量熔融發生在含水固融線溫度之上變得容易，或是向上往低溫處逃逸。這是一個錯綜複雜的動力過程，曾經有許多數值模型以此為主題的努力（例如： *van Keken et al.*, 2002; *Peacock et al.*, 2004; *Arcay et al.*, 2005）。在東北日本之下，低 V_P、V_S 和高 V_P/V_S 異常位於地幔楔中並大致平行隱沒板塊者，大多被解釋為熔融的表徵（例如：*Zhao et al.*, 2009），其熔融比例 ϕ 約在 1-2%（*Nakajima et al.*, 2005）。蛇紋岩化層隨後在同一地區被 *Kawakatsu and Watada* （2007）所仔細地描述，並被定位在熔融區與隱沒板塊之間。就技術上來說，熔融程度可以藉由 ϕ 的微分導數來取代 Θ 的微分導數而求得。檢驗 *Nakajima et al.* （2005）的熔融模式，指出 V_S 和 V_P/V_S 相對於 ϕ 的微分導數；其正負號與相對於 Θ 的微分導數一致，意味著高蛇紋岩化的結果同樣可轉換成高比例的熔融。

然而，我們克制住自己貿然解釋熔融的現象，是因為以下兩個觀察。第一，東北日本的熔融區域是位在活躍火山前緣之下的地幔楔炎熱核心，且水平距離隱沒板塊表面至少 50 到 100 公里。相對來說，在東北臺灣以及琉球最西端，能夠獲得較佳解析的高 V_P/V_S 特徵，只侷限在鄰近隱沒板塊的弧前淺層。雖然在邊緣處的地幔楔可能稍微溫暖，但並沒有任何現今的火山活動在弧前區域之上被報導過。第二，相較於東北日本的活躍火山前緣活動頻繁，此處活躍火山前緣的火山活動規模要小得許多（*Sibuet et al.*, 1998; *Chung et al.*, 2000; *Tatsumi and Eggins*, 1995; *Tamura et al.*, 2002），這意或許味著至少現今是處於較低的熔融噴發時期。就另一方面來說，觀察範圍的限制無法允許我們向北進入地幔楔核心採樣，完整描繪出熔融的分佈。在目前的工作中，我們將隱沒板塊表面之上的低 V_P、低 V_S 和高 V_P/V_S 異常現象歸因於橄欖岩質地幔的蛇紋岩化。若要定義出本區熔融的分佈與特性，恐怕只有寄望於未來大範圍在沖繩海槽施放海底地震儀才能做到了。

我們的模型顯示蛇紋岩化的程度，在琉球隱沒帶最西緣的弧前，可以達到 15%。這可以與喀斯開地區單獨利用 V_P 異常所進行的估計（*Zhao et al.*, 2001）相比，但小於反射結果所推算之區域 $\delta\Theta$ 的最大值（*Bostock et al.*, 2002）。相較於蛇紋岩（$\delta\Theta$=100）含水 15%重量（例如：*Hacker et al.*, 2003），本研究弧前地幔最大含水量約 2%，且由於層析影像的變異已經過嚴重壓抑，因此區域性水的含量可能超過這個數值。這個結晶水的含量在蛇紋石綠泥石純橄岩領域（~6%）以及

綠泥石斜輝橄欖岩領域(~1.4%)、深度 50 公里(~1.5 GPa)且溫度介於 500-800°C 的情況下，應該相當穩定（*Hacker et al.*, 2003）。根據參考文獻，這個溫度低於橄欖岩含飽和水狀態下的固融線（在淺層地幔的壓力下，約為 900-1000°C）

（*Kawamoto and Holloway*, 1997; *Grove et al.*, 2006）。

在蛇紋岩化假說中，不證自明的結果就是玄武岩地殼在 50 公里以下位置顯著地釋放出水。這需要海洋地殼所處的環境達到足以破壞含水礦物，使其釋放出大量水的溫度範圍。然而，溫度 500-800°C 的範圍，在 1.5-2 GPa （約 50-65 公里深）狀況下，大部分介於含水量較低（<1%）的榴輝岩領域（*Hacker et al.*, 2003）。合理的推論是海洋地殼跨過藍色片岩/綠色片岩—榴輝岩的交界（約 400-500°C 並介於 1.5-2 GPa 的情況下）(*Hacker et al.*, 2003)，於是有大量的水(約 5%）可以被排擠出來，並讓弧前地幔產生水合。在經過這個深度範圍時，溫度可能會從低於 400°C 上升到高於 500°C。在深度 50 公里處，含飽和水的玄武岩其固融線約為 650°C（*Lambert and Wyllie*, 1972）。較次要的脫水熔融可能會在約 700-750°C 間，因為 zoisite-out 的反應而發生，但這不會持續發生到>900°C，也就是角閃石被破壞且地殼顯著熔融的溫度（*Vielzeuf and Schmidt*, 2001; *Hacker et al.*, 2003）。因此不僅大量的熔融看似不可能發生，且即使是少量的海洋地殼熔融亦可以完全地排除。

對於琉球隱沒帶西緣，地殼熔融的地球化學證據尚未被完全地建立。高鎂安山岩（HMAs）被認為是隱沒板塊熔融的表徵，並曾經在西表島（一千三百萬年前的活躍火山前緣，目前位於弧前）上被報導，但它的地化特徵並不支持其源自於隱沒帶（*Shinjo*, 1999）。然而，最近關於龜山島（活躍火山前緣）的工作顯示，部分採集自龜山島上的岩石顯示出具有高鎂的組成，意即隱沒板塊熔融在某種程度上貢獻了島弧的火山活動（*Chu*, 2005）。這個議題目前仍是開放且仍在發展之中，且地球化學的研究前緣或許更能一窺其究竟。為了瞭解琉球最西緣底下的地幔楔或隱沒板塊熔融，未來必須結合數值模擬、地化控制、以及地震學影像等工作，才能有更明確的結果。

5.5 震波層析影像的解讀

5.5.1 次要與小尺度的構造

在近期的層析影像研究工作中，*Lin et al.*（2004）在隱沒板塊介面，距離地表 40 公里深處，得到一個高 V_P/V_S 的通道向上升起，斜向延伸至宜蘭平原（距離龜山島仍有 15 公里遠）。這個通道的呈現本身就具有一點策略性，且相對於平均地幔楔的強度來說，這個特徵亦相當微弱。藉由結合中央氣象局與日本氣象廳的資料組，並小心翼翼地調整 V_P/V_S 反演，我們檢驗這個特徵是否明顯存在並值得繼續闡明。需注意在這個區域的模型格點間隔是 10 公里，而可恢復的不均向性尺度大約亦是 10 公里，這樣的參數化尺度應足以解析 *Lin et al.*（2004）所發現的通道。

圖十六比較了本研究與 *Lin et al.*（2004）相同垂直剖面的層析影像。由於本研究能夠清楚地解析隱沒板塊，因此其他部分影像的可信亦因此較高。我們無法在結果中看見任何存在著連結隱沒板塊至地表，並切過地幔楔的通道存在。透過所有的剖面，都沒有發現類似那樣顯著的異常存在。我們同時針對 V_P 和 V_S 測試不同組合的壓抑係數，亦即選取圖六 a 中取捨曲線最佳化的周圍數值。其中一組數值所建立的模型，且其二維剖面上的變異量相同於 *Lin et al.*（2004）。但即使覆蓋在隱沒板塊上的高 V_P/V_S 層依舊存在，但就是無法重製 *Lin et al.*（2004）所宣稱存在的熔融通道之任何跡象。且此所謂熔融現象的次要構造，甚至是出現在一個連琉球隱沒板塊這個主要構造都無法解析的同一個剖面上。

在他們最近的研究成果中 *Lin et al.*（2007），結合了中央氣象局、日本氣象廳與海底地震儀的資料，以控制本區域的速度結構，與本研究類似，但僅討論深度 60 公里以內的範圍。他們的海底地震儀記錄了約 12 天的資料，也許可以提供沖繩海槽之地殼結構一些額外的控制。如果能採取適當的參數化進行反演，這個優勢將具有提供更佳的弧前與隱沒板塊影像之潛力。*Lin et al.*（2007）報導了更多熔融「通道」的存在，這些通道沿著走向在隱沒板塊的不同部分提供給活躍火山前緣或弧後軸線。然而，比較 *Lin et al.*（2007）與本研究，其結果並不直覺；由於他們的「通道」在三維結構中變異極大又太過細微，且極可能未達本研究模型的解析尺度。在本研究中，我們未試圖將零星的異常構造追蹤，並將之連結成一個表面上看似連續的構造且賦予其重要性。

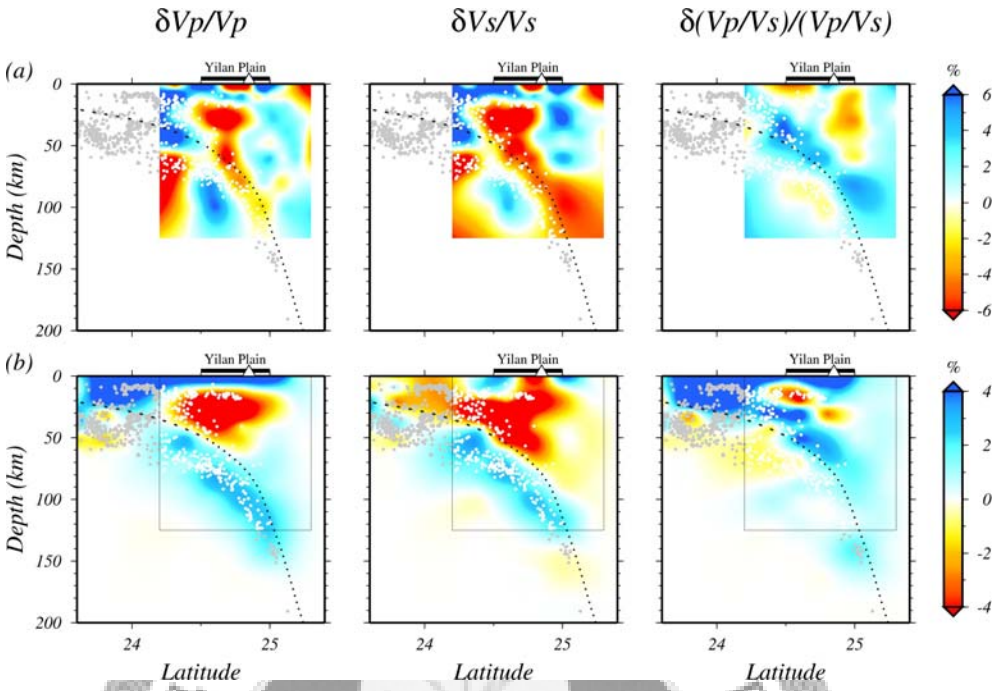

圖十六　比較 V_P、V_S 和 V_P/V_S 沿著先前研究的剖面 2 在（a）*Lin et al.*（2004）及（b）本研究中的結果。剖面位置請見圖一。注意主要的特徵例如出現在隱沒板塊表面的高 V_P/V_S 在兩個研究中均有解析出來，僅型態略有不同；至於 *Lin et al.*（2004）中次要的特徵，像是微弱的正 V_P/V_S 異常從隱沒板塊斜向延伸至表面的現象，在本研究中則沒有解析出來。而隱沒板塊是為最重要的結構，在本研究中則是比 *Lin et al.*（2004）解析得要好。

5.5.2 解析力的可信度

圖十七為 Wu et al., 2009 在與本研究相近區域所發表的震波層析影像結果，其結果中最引人注目的特徵為圖十七（c）的垂直剖面中，有一垂直的高 P 波與 S 波速度比值異常，自 120 公里深處向上延伸至 50 公里左右。根據其棋盤檢定的結果顯示（圖十七 b），此一位置的解析能力「幾近完美」，用以支持此一構造的可信度。

不過，本研究亦採用相似地震資料，但該處的解析度卻是遠低於 R25 的範圍，且由地震與測站分佈情形來看，該特徵所出現位置（圖十七 a 中的紅色圓圈），僅有少數地震及唯一測站（PCY）位在鄰近地區，為何該研究結果能夠呈現如此完美的解析能力，實在令人好奇，仍有待進一步的檢驗。

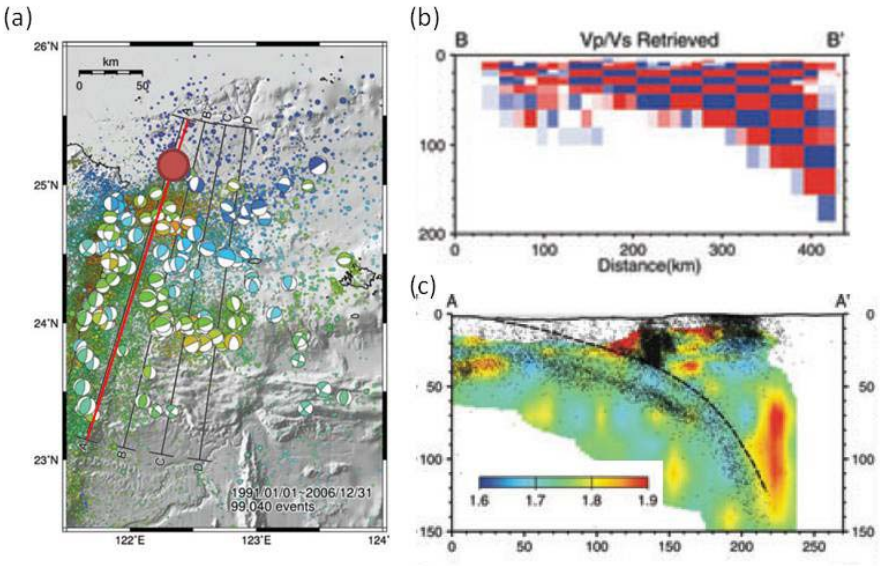

圖十七 Wu et al., 2009 所發表台灣東北外海震波層析影像。（a）索引地圖，紅線表示（b）與（c）剖面的位置，紅色圓圈表示（c）剖面中高 P 波與 S 波速度比值異常投影至地表之位置；（b）棋盤檢定結果；（c）P 波與 S 波速度比值。

第六章　結論

精確的三維地震定位結果，提醒我們要以更好的動力控制來重新解釋琉球隱沒板塊的變形。地震的分佈結果第一次揭露隱沒板塊沿著走向方向的褶皺，出現在深度 50-100 公里處。褶皺的現象在兩個方面相當顯著：他的曲率比整個琉球海溝都大，而且異號；以及他的波長相對較短，只有 250 公里左右。這暗示褶皺是肇因於加諸隱沒板塊上的水平壓縮，來自菲律賓海板塊斜向隱沒而頂住了歐亞岩石圈並受到阻擋的緣故。震源機制解與大曲率的爭議，傾向於是由黏彈性的不穩定度導致了褶皺的發生。我們想像其變形的型態，是源自於隱沒板塊同時藉由脆性破壞及黏彈性褶皺，反應因頂住歐亞岩石圈所造成的壓縮。一個麥斯威爾形式的模型被利用來模擬這個現象，並協助控制可以被接受的模型範圍。要褶皺成我們所觀察到的波長，隱沒板塊只能比周圍地幔黏滯性大約一百倍，並有很大可能範圍的平面內彈性應變；或是比周圍地幔黏滯性大約一千倍，則彈性應變可以被允許有 0.05 附近。部分是由於褶皺的原因，瓦達地班尼奧夫帶在靠近臺灣一側漸漸變陡，並達到 80 公里以下。在隱沒板塊之內，整個隱沒帶深度 40-80 公里的範圍裡，雙層地震帶則是明顯地被描繪出來。雙層地震帶間隔約 15-20 公里，主要受到與褶皺隱沒板塊相同的側向壓縮應力。

藉由結合中央氣象局與日本氣象廳的資料，我們以台灣近海最佳的解析度，建構了台灣東北與琉球最西緣底下的隱沒帶與地幔楔之層析影像模型。在觀測網分布範圍相對來說並不利於觀測的條件下，我們對於反演的正則化以及結果的解釋，都採取保守的方式進行。層析影像中最主要的現象是與隱沒琉球板塊相關的高 V_P 和 V_S 異常，隱沒板塊上方地幔楔的特徵則是高 V_P/V_S。過去在層析影像工作中曾經被描述的高 V_P/V_S 通道，且被解釋為從隱沒板塊供給宜蘭平原的熔融途徑，在本研究中無法被重製。隱沒板塊的特徵符合-200 到-400 ^{o}C 的溫度異常。顯著的低 V_P、V_S 和高 V_P/V_S 異常出現在弧前地幔楔中，也就是今日火山前緣的南方。我們將這個現象解釋為隱沒海洋地殼的玄武岩—榴輝岩變質作用釋出水後，造成地幔橄欖岩的水合，我們並利用實驗數據，將蛇紋岩化的比例參數化。在台灣東北附近的弧前地幔楔，其蛇紋岩化的峰質約可達到 15%以上，或是含水 2%。這將是從過去強調熔融所扮演角色的觀點，重新出發的的重要里程。若要完成完整的地幔楔影像以及熔融分布，增加海底地震儀以擴展觀測陣列是未來至為重要的關鍵。

第七章　附錄

7.1 黏彈性板塊性質

We follow the linear-operator approach of *Flügge* [1975]. The bending stress and strain for a 2-dimensional layer is related by the linear operators:

$$P_l(\sigma) = Q_l(\varepsilon) \tag{A1}$$

where subscript *l* denotes the operators for layer. Without introducing material properties, the balance between the bending moment, horizontal compression per unit length perpendicular to the direction of compression *N*, and vertical loading *q* leads to

$$\frac{h^3}{12} Q_l\left(\frac{\partial^4 w}{\partial x^4}\right) + P_l\left(N\frac{\partial^2 w}{\partial x^2}\right) = P_l(q) \tag{A2}$$

where *w* is the vertical deflection of the layer, *h* the thickness of the layer, and *x* measures horizontal distance in *N*-parallel direction. For a Maxwell material that responds instantaneously to external stresses followed by a viscous deformation, the contributions from the elastic and viscous parts are summed on strain rate:

$$\dot{\varepsilon} = \frac{\dot{\sigma}}{E_l^*} + \frac{\sigma}{4\mu_l} \tag{A3}$$

Here each contribution is for a thin plate, and $E_l^* = E_l/(1-\nu^2)$ with E_l the Young's modulus of the layer, and μ_l the viscosity of the layer. With these, the operators are defined as

$$P_l = 1 + \tau_l \cdot \frac{\partial}{\partial t} \ , \ Q_l = 4\mu_l \cdot \frac{\partial}{\partial t} \ , \tag{A4}$$

where $\tau_l = 4\mu_l / E_l^*$ is the relaxation time of the Maxwell material. Equation (A2) becomes

$$D_v \frac{\partial}{\partial t} \cdot \frac{\partial^4 w}{\partial x^4} + N\left(1 + \tau_l \frac{\partial}{\partial t}\right) \cdot \frac{\partial^2 w}{\partial x^2} = \left(1 + \tau_l \frac{\partial}{\partial t}\right) \cdot q \tag{A5}$$

This is the governing equation for bending of a Maxwell layer under transverse loading *q* and in-plane compression *N*; $D_v = \mu_l h^3/3$ is the flexural rigidity of a viscous plate. Equation (A5) reduces to bending of an elastic plate as $\mu_l \to \infty$ and $\tau_l \to \infty$:

$$D_e \cdot \frac{\partial^4 w}{\partial x^4} + N \cdot \frac{\partial^2 w}{\partial x^2} = q \tag{A6}$$

where $D_e = E_l^* h^3/12$ is the flexural rigidity of an elastic plate. Equation (A5) reduces to viscous plate bending as $E_l^* \to \infty$ and $\tau_l \to 0$:

$$D_v \cdot \frac{\partial^4 \dot{w}}{\partial x^4} + N \cdot \frac{\partial^2 w}{\partial x^2} = q \tag{A7}$$

Because external loading is passive in a folding problem, the medium operators link *q* with deflection *w*:

$$P_m(q) = Q_m(w) \tag{A8}$$

Assume the deflection *w* has the form of $w(x,t) = A(t) \cdot \sin(kx)$,

$$P_m = 1, \quad Q_m = -4k\mu_m \frac{\partial}{\partial t} \tag{A9}$$

for viscous medium, where μ_m is the viscosity of the medium. Equation (9) implies that the resistance is proportional to the wavelength at which the layer is folded. Insert (8) and (9) into (5) to eliminate *q*, we obtain

$$D_v \frac{\partial w''''}{\partial t} + N \cdot w'' + \tau_l \cdot N \cdot \frac{\partial w''}{\partial t} = -4k\mu_m \frac{\partial w}{\partial t} - 4k\mu_m \tau_l \frac{\partial^2 w}{\partial t^2} \tag{A10}$$

The characteristic equation for the solution of the form of $A(t) \cdot \sin(kx)$ is

$$4\mu_m \tau_l \frac{\partial^2 A}{\partial t^2} - \left[\tau_l Nk - D_v k^3 - 4\mu_m\right] \cdot \frac{\partial A}{\partial t} - Nk \cdot A = 0 \tag{A11}$$

and *A*(*t*) is composed of two terms: $\exp(\omega_1 \cdot t)$ and $\exp(\omega_2 \cdot t)$ where

$$\omega_{1,2}\tau_l = \frac{\gamma}{8}\left[-b \pm \sqrt{b^2 + c}\right] \tag{A12}$$

where

$$b = \frac{\bar{k}^3}{3} - 4\varepsilon_N \bar{k} + \frac{4}{\gamma}, \quad c = 64\varepsilon_N \frac{\bar{k}}{\gamma}, \tag{A13}$$

and $\gamma = \mu_l / \mu_m$. The normalized wavenumber $\bar{k}$ =2π/(λ/*h*), and ε_N is defined as

$$\varepsilon_N = \frac{N/h}{E_l^*}, \tag{A14}$$

which approximates the in-plane elastic strain or the membrane strain due to lateral compression. The amplification functions ω_1 >0 which promotes instability, and ω_2 <0 which stabilizes perturbations, but the total amplification rate is always greater than zero. The amplification ω_1 can be plotted as a function of normalized wavelength and the wavelength for the dominant member of folding λ_d can be found numerically. The result is consistent with that of *Schmalholz and Podladchikov* [1999].

For the case of an elastic layer embedded in a viscous medium, we start with equation (A6) to derive the dominant wavelength:

$$\frac{\lambda_d}{h} = \pi \left[\frac{1}{\varepsilon_N} \right]^{1/2} \tag{A15}$$

The instability occurs when $\lambda > (1/3)^{1/2} \lambda_d$. For a viscous layer folding in a viscous medium, λ_d can be expressed analytically too:

$$\frac{\lambda_d}{h} = 2\pi \left[\frac{\gamma}{6} \right]^{1/3}, \tag{A16}$$

The derivation of equations (A15) and (A16) can be found in *Biot* [1961].

7.2 震波層析影像其他結果

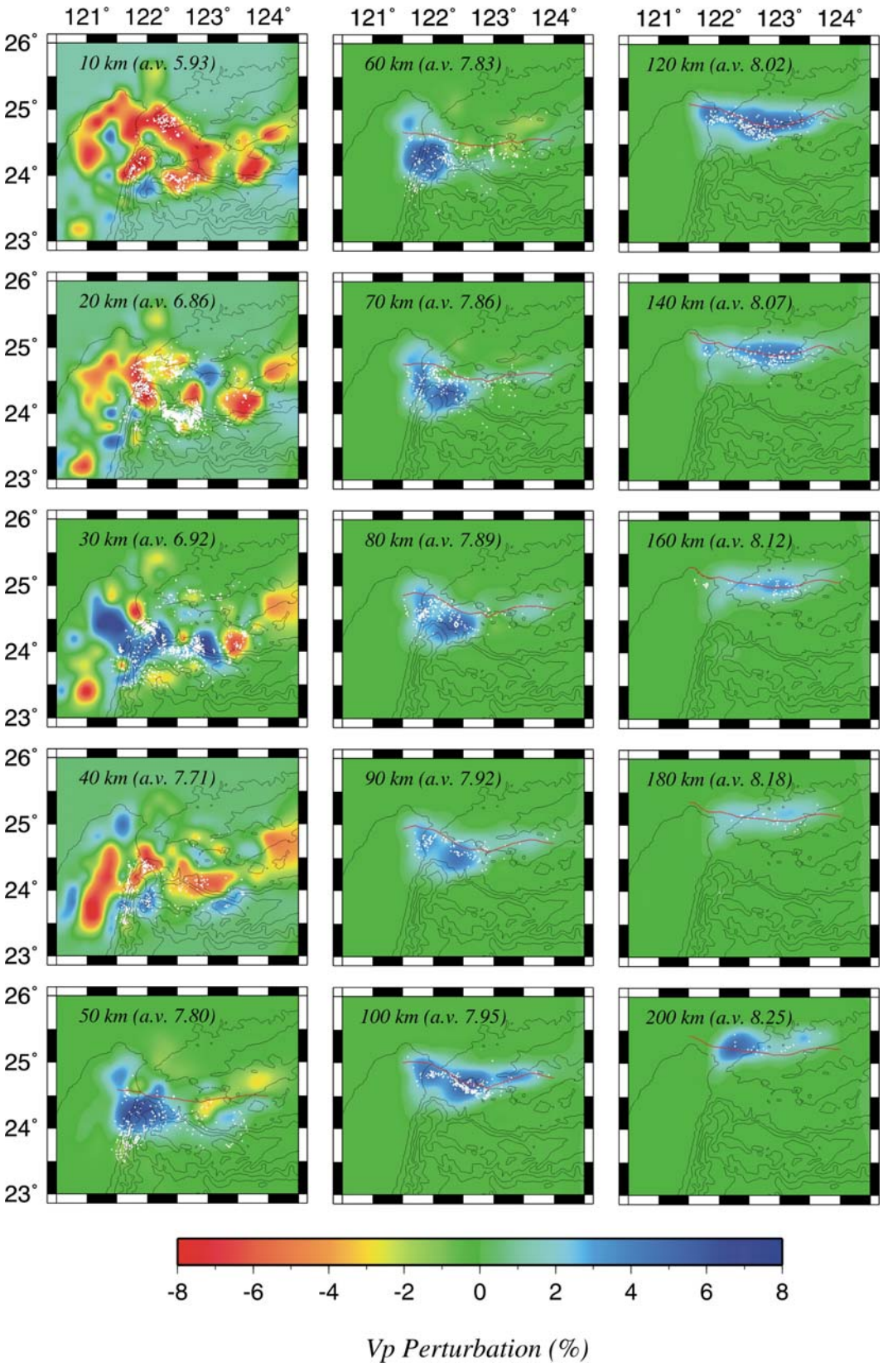

圖十八 P 波速度異常水平剖面圖

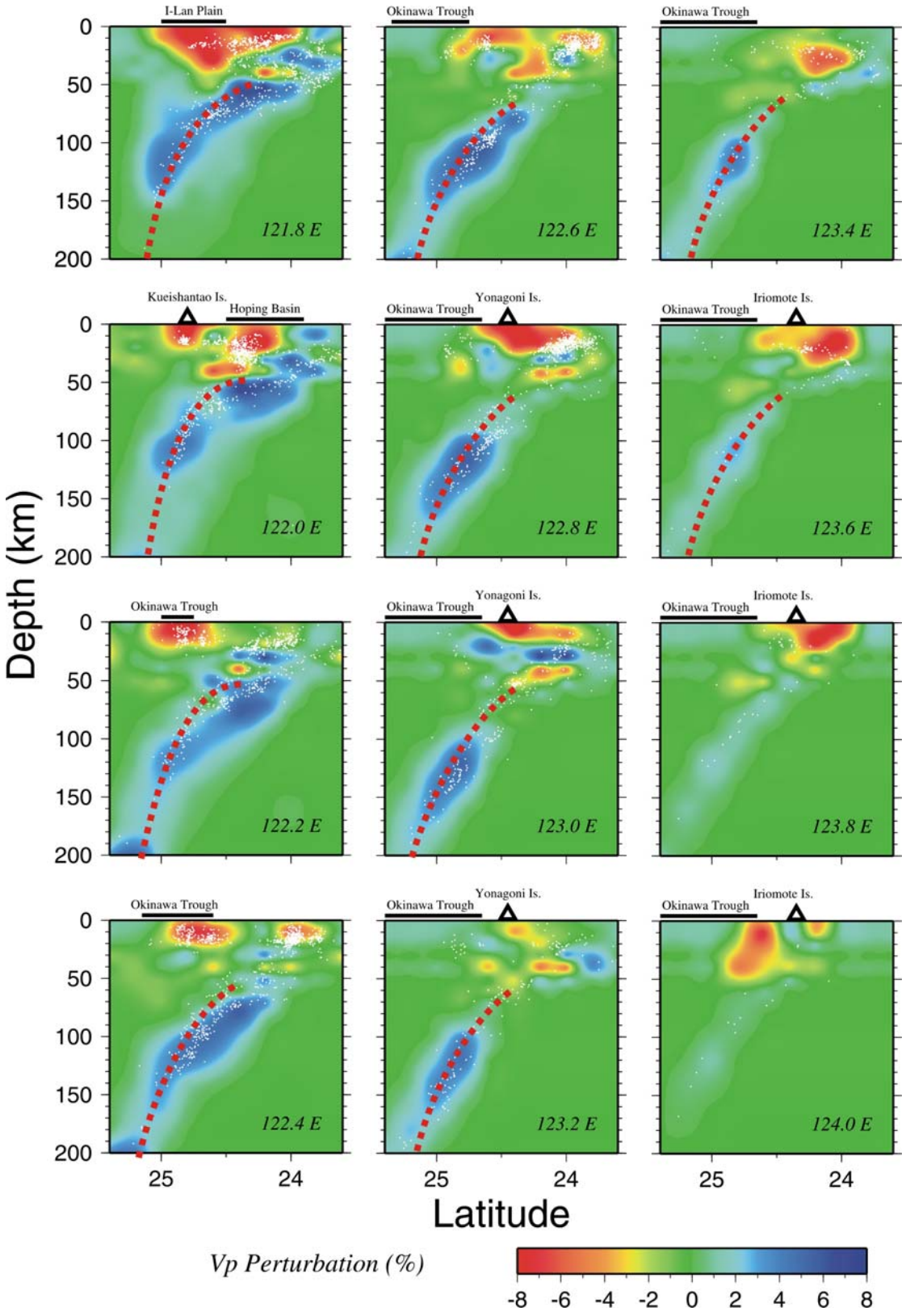

圖十九 P 波速度異常垂直剖面圖

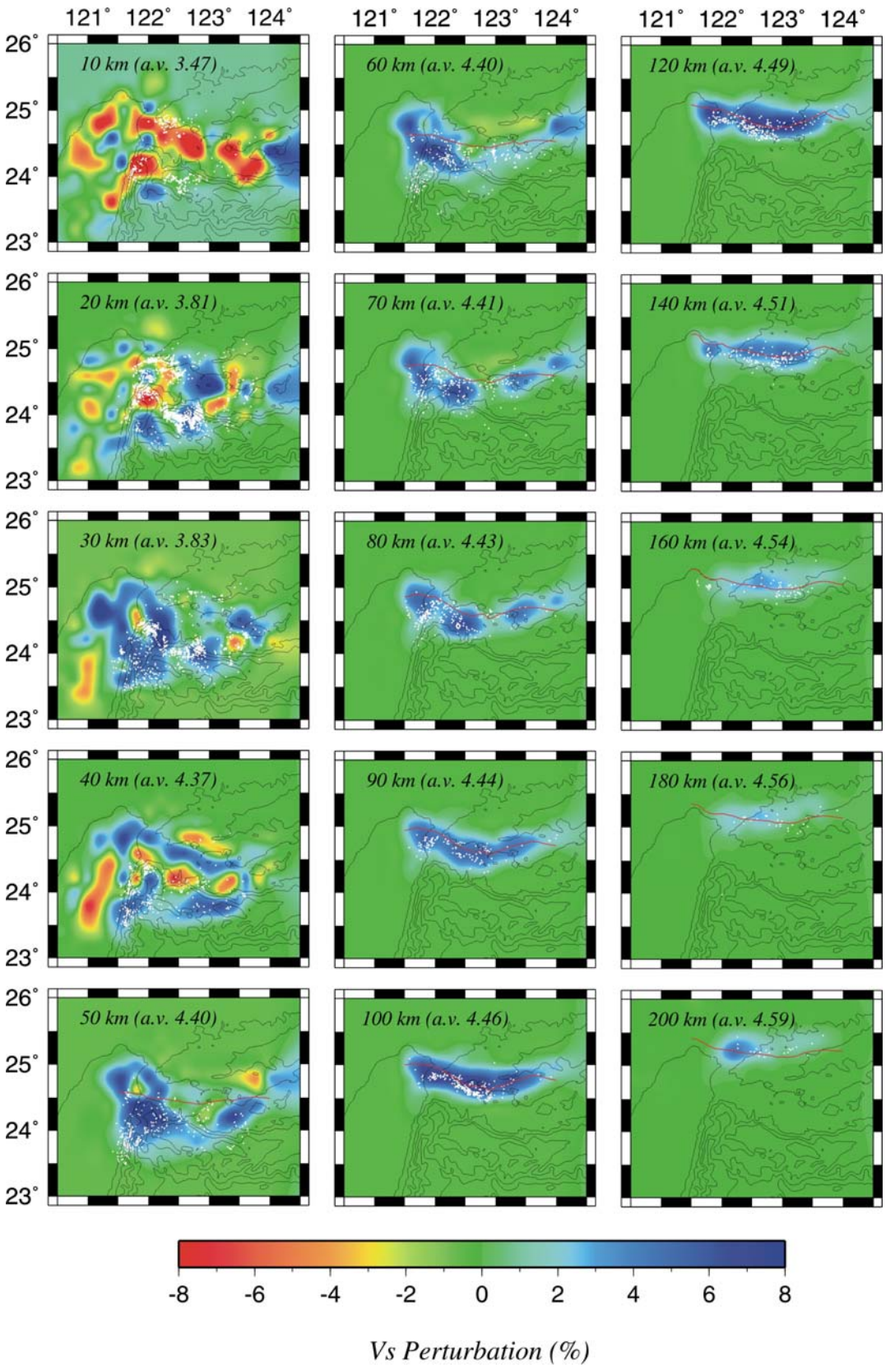

圖二十 S 波速度異常水平剖面圖

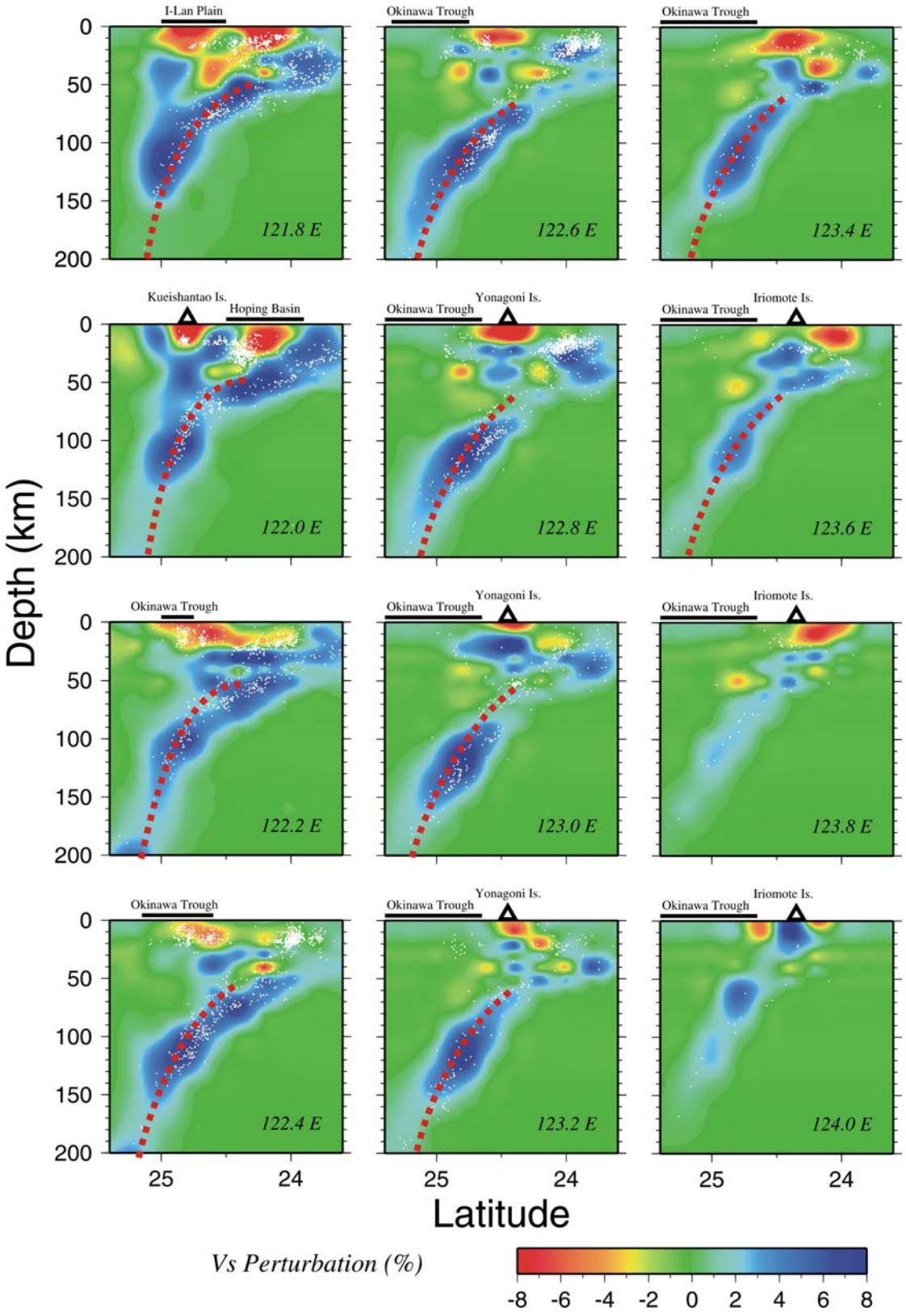

圖廿一 S 波速度異常垂直剖面圖

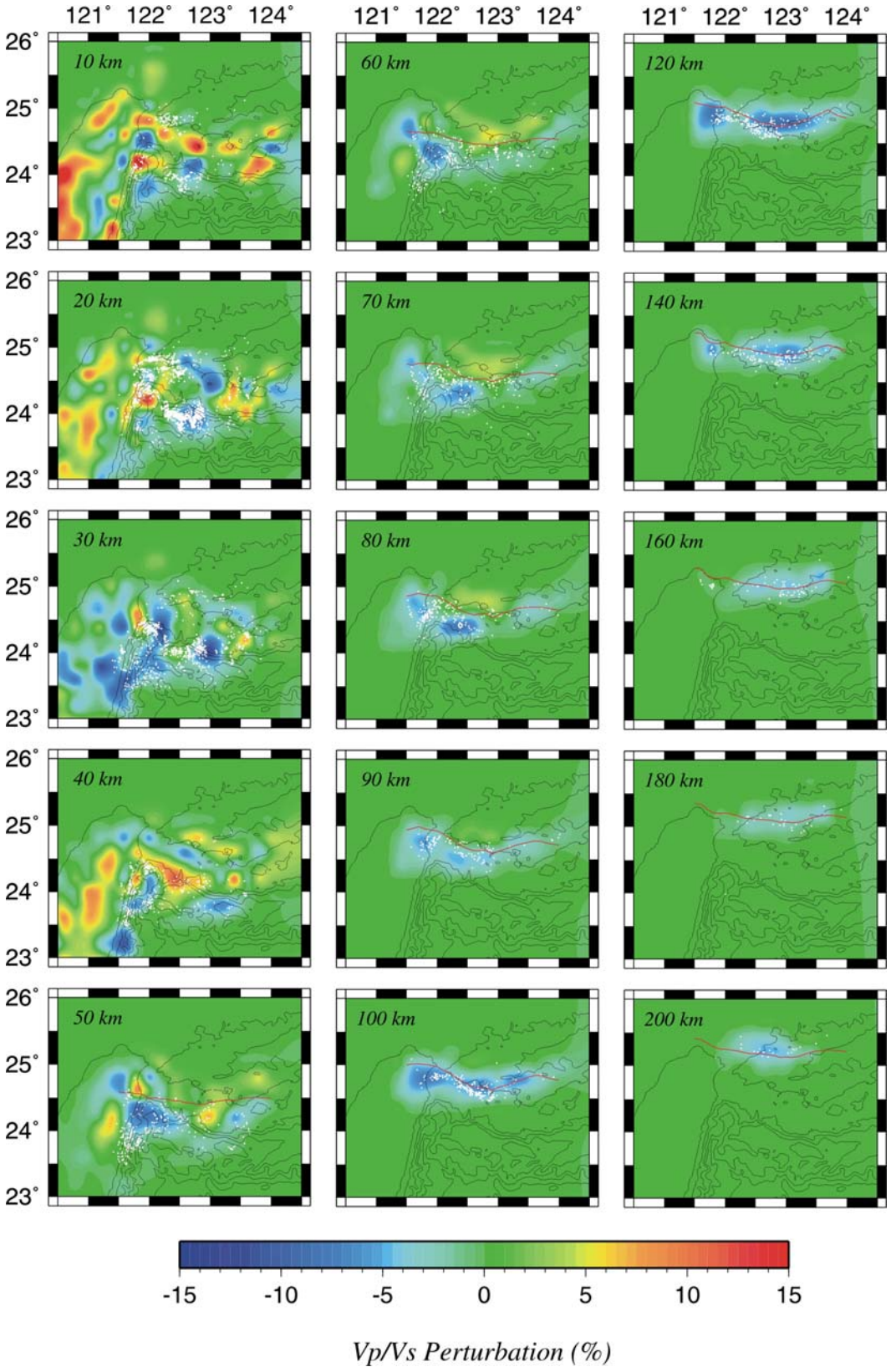

圖廿二 P 波與 S 波速度比值異常水平剖面圖

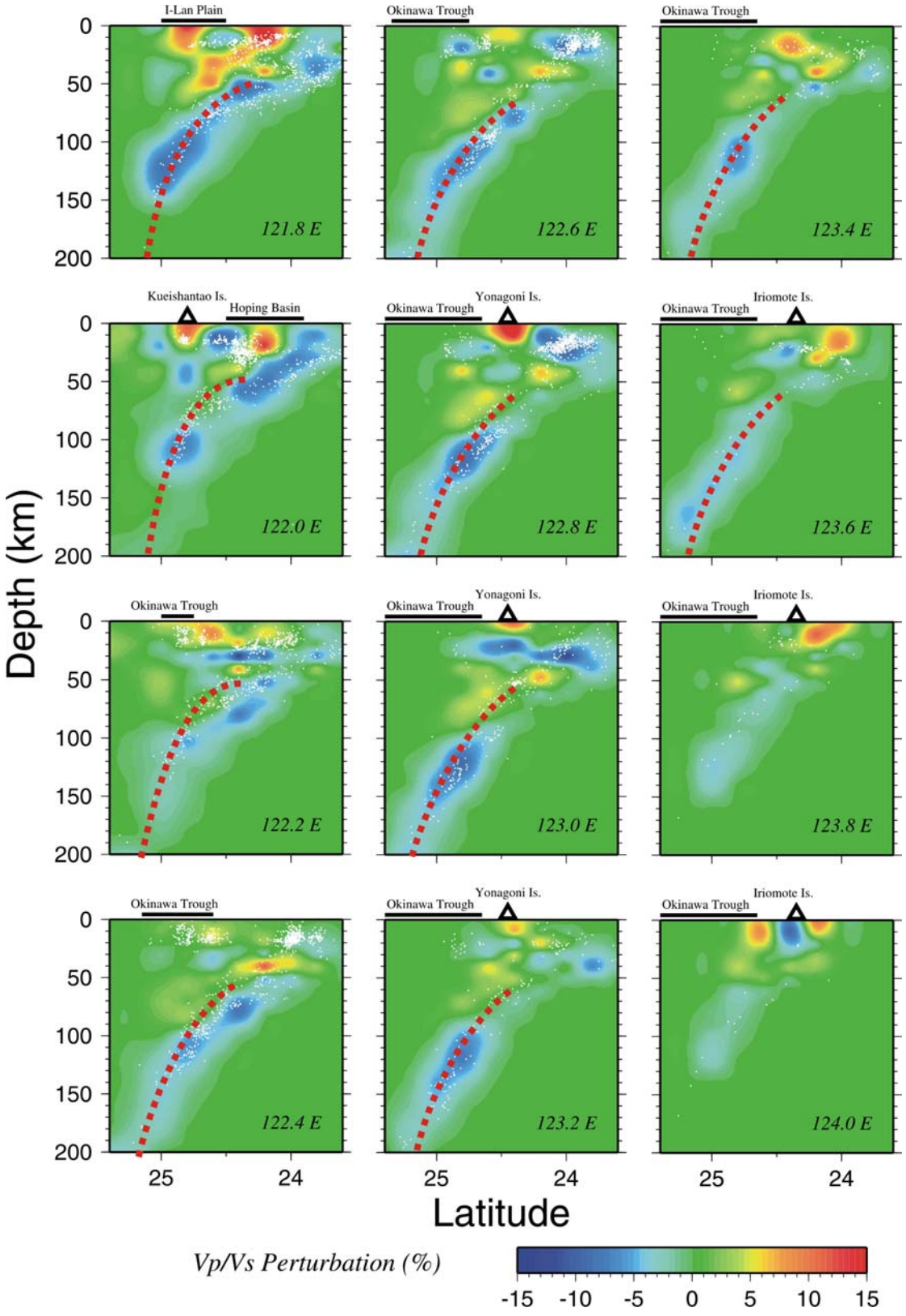

圖廿三 P 波與 S 波速度比值異常垂直剖面圖

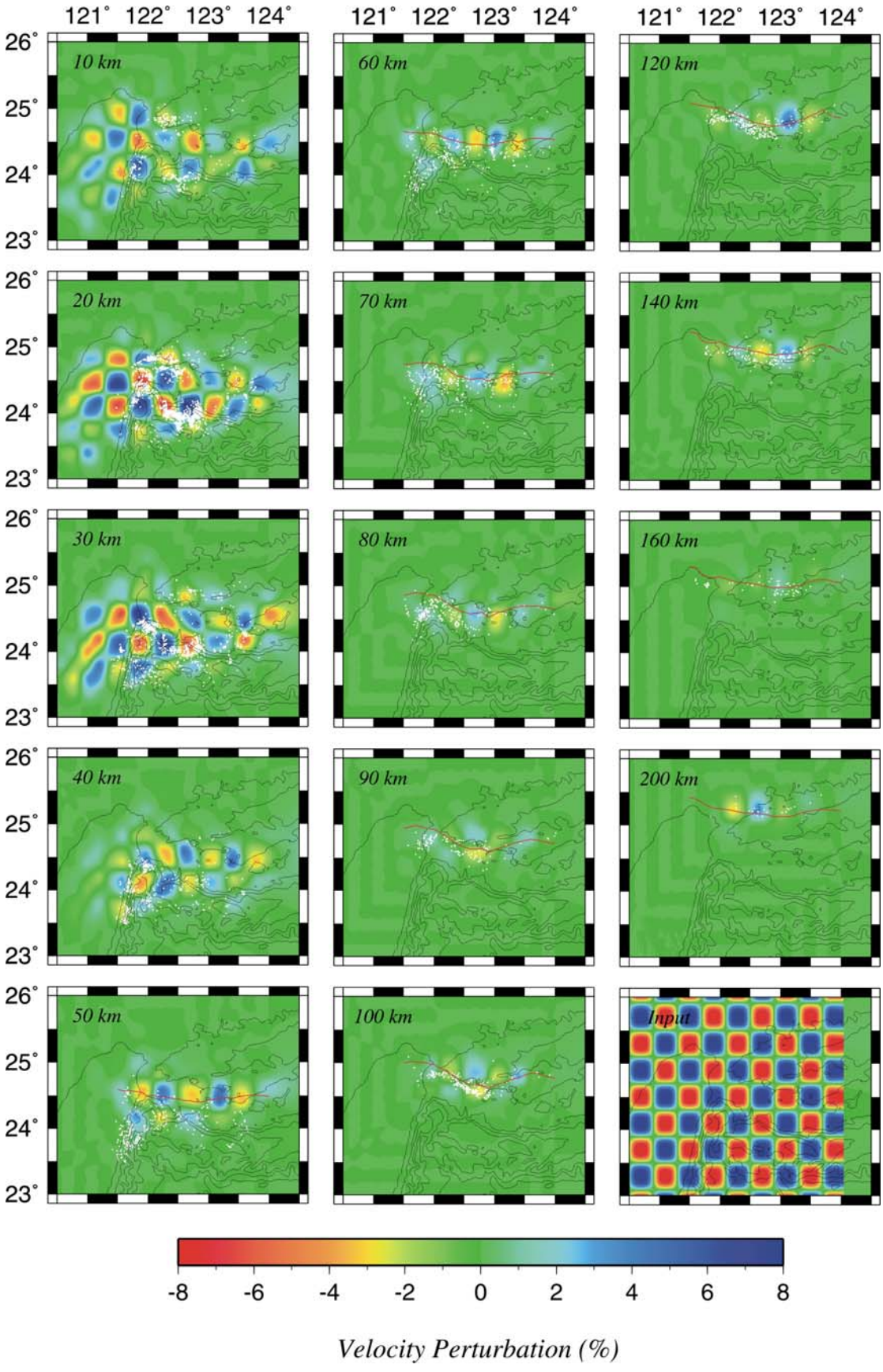

圖廿四 棋盤檢定水平剖面圖（一倍格點間隔）

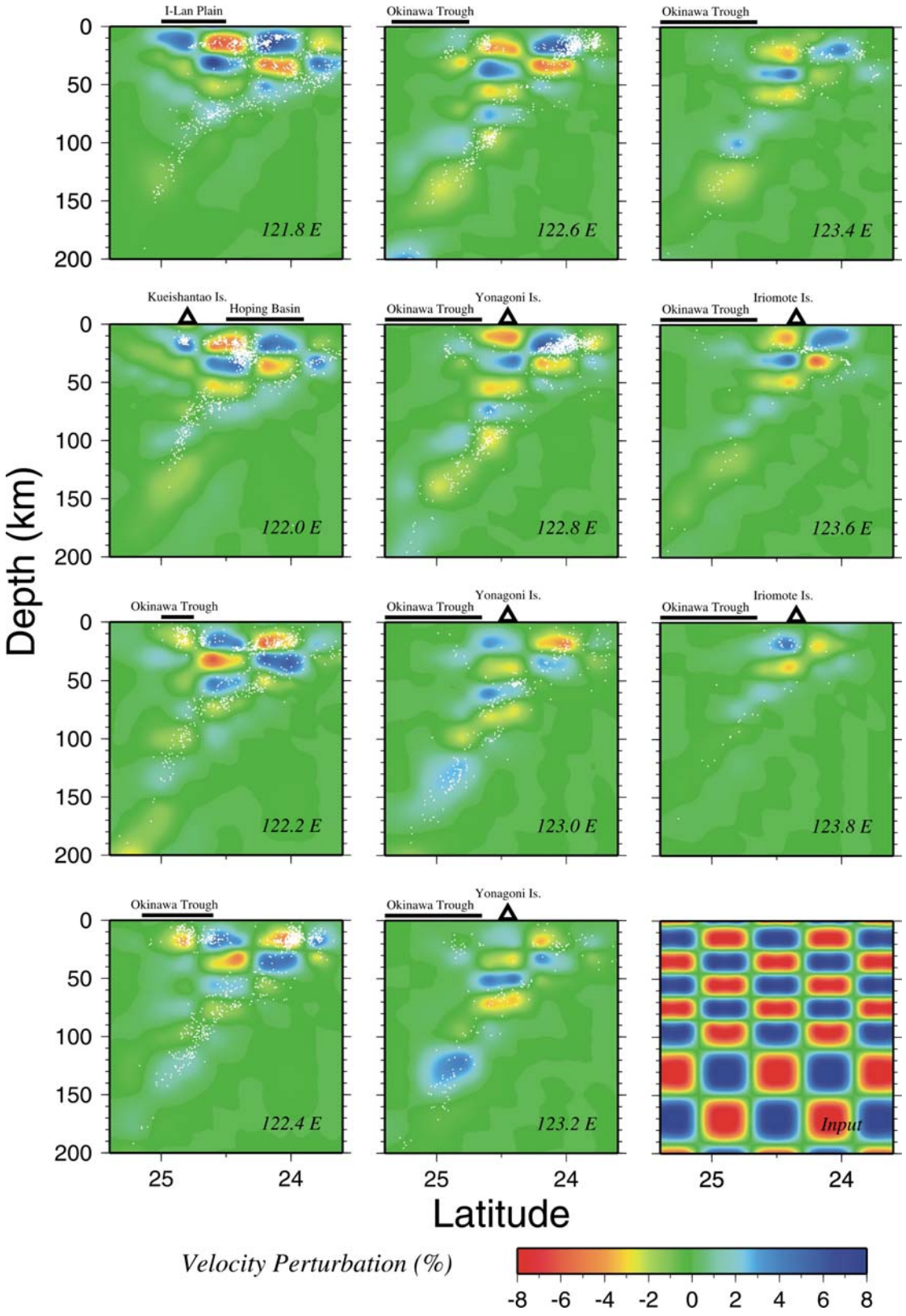

圖廿五 棋盤檢定垂直剖面圖（二倍格點間隔）

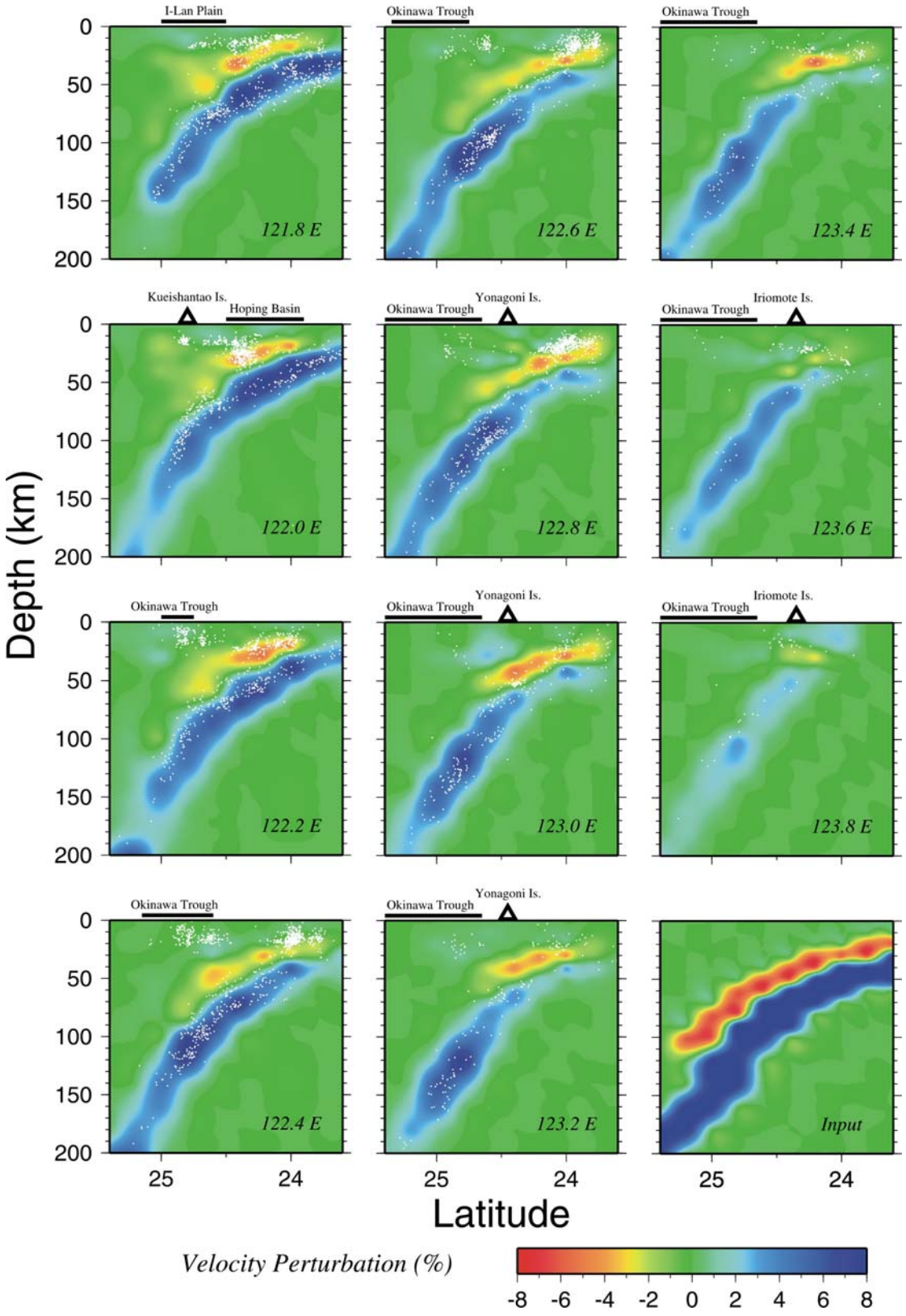

圖廿六 模擬檢定垂直剖面圖

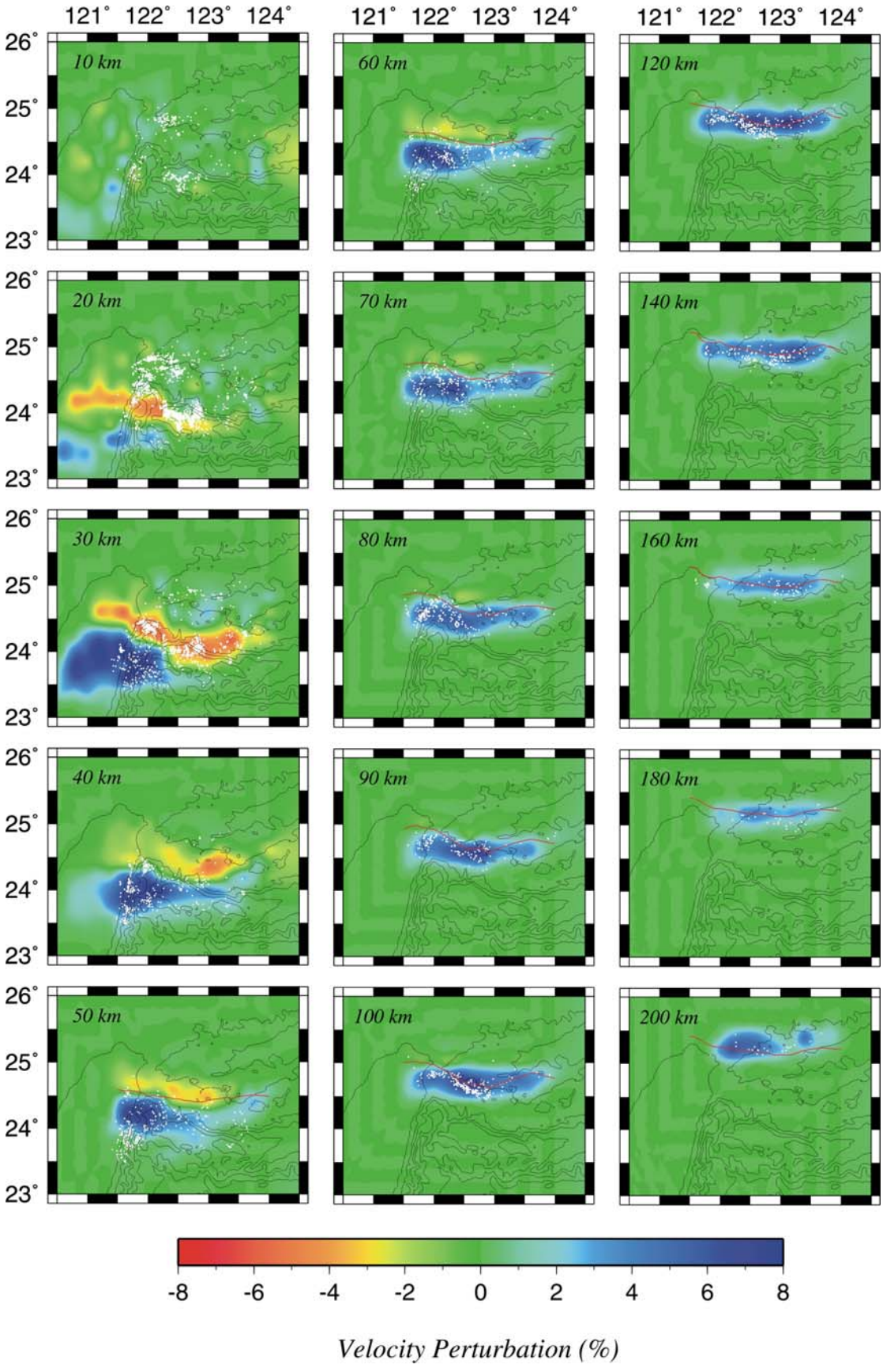

圖廿七 模擬檢定水平剖面圖

7.3 蛇紋岩化參數及反演

當依據地幔楔蛇紋岩化礦物的不同而選擇不同參數時，所得到不同的結果，可以藉由以下的計算過程中理解。首先將 3.7 中的（10）改寫成：

$$\begin{bmatrix}\delta T\\ \delta\Theta\end{bmatrix}=\begin{bmatrix}\dfrac{\partial \ln V_S}{\partial T} & \dfrac{\partial \ln V_S}{\partial \Theta}\\ \dfrac{\partial \ln(V_P/V_S)}{\partial T} & \dfrac{\partial \ln(V_P/V_S)}{\partial \Theta}\end{bmatrix}^{-1}\begin{bmatrix}\delta \ln V_S\\ \delta \ln(V_P/V_S)\end{bmatrix}.....(A17)$$

則根據 Christensen, 1966 所提出的蜥蛇紋石（Lizardite）數據，上式中$[\ ]^{-1}$內的數值為：

$$\begin{bmatrix}467 & 11\\ -23326 & -10537\end{bmatrix}$$

相較於 Christensen, 2004 所提出的葉蛇紋石(Antigorite)數據，(A17)式中$[\ ]^{-1}$內的數值為：

$$\begin{bmatrix}1735 & 40\\ -44932 & -11033\end{bmatrix}$$

可以發現，式中影響蛇紋岩化的兩個參數（467,11）放大為四倍（1735,40），因此計算出來的蛇紋岩化程度亦放大了四倍（圖十五）。而溫度異常的兩個參數（-23326,-10537）中，僅針對$\delta \ln(V_P/V_S)$的部分放大了兩倍（-44932），而$\delta \ln(V_P/V_S)$異常又主要集中在隱沒板塊之上，因此新增加了隱沒板塊之上的溫度異常結果。

因此就數學式的計算來說，這個結果是相當直覺的。但地幔楔之蛇紋岩化礦物究竟為何者，則仍待其他證據的控制。

本研究中選用了$\delta \ln(V_P/V_S)$及$\delta \ln V_S$作為反演的觀測數據，但其實若利用$\delta \ln(V_P/V_S)$及$\delta \ln V_P$或$\delta \ln V_P$及$\delta \ln V_S$，甚至以$\delta \ln(V_P/V_S)$、$\delta \ln V_P$及$\delta \ln V_S$三者同時進行反演，都可以獲得相似的結果（圖廿八）。

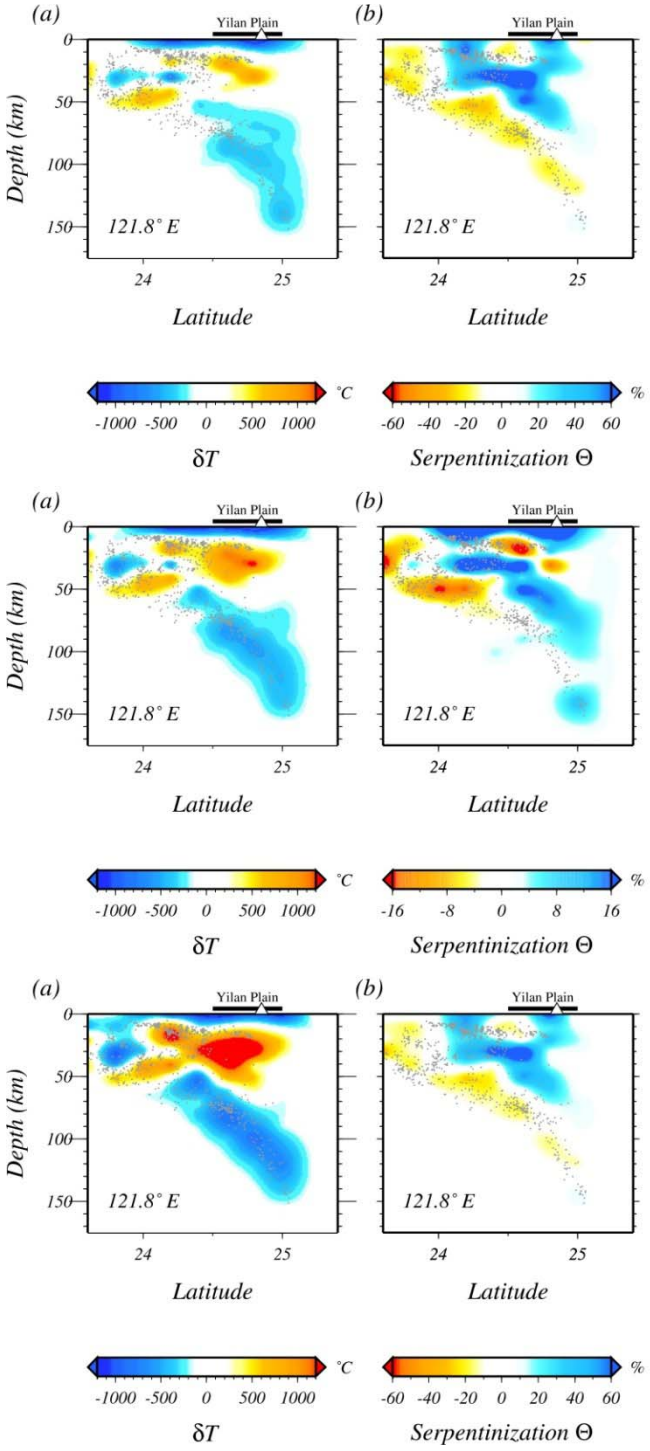

$\delta \ln V_P$ 及 $\delta \ln V_S$

$\delta \ln(V_P / V_S)$ 及 $\delta \ln V_S$

$\delta \ln(V_P / V_S)$ 、 $\delta \ln V_P$ 及 $\delta \ln V_S$

圖廿八　根據不同數據所反演得到之溫度異常與蛇紋岩化成的的結果。

第八章　參考文獻

Abers, G. A. (1992), Relationship between shallow and intermediate depth seismicity in the eastern Aleutian subduction zone, *Geophys. Res. Lett., 19*, 2019-2022.

Arcay, D., E. Tric, and M. P. Doin (2005), Numerical simulations of subduction zones: effects of slab dehydration on the mantle wedge dynamics, *Phys. Earth and Planet. Int., 149*, 133-153.

Bergman, E.A., and S.C. Solomon (1990), Earthquake awarms on the Mid-Atlantic Ridge: Products of magmatism or extensional tectonics?, *J. Geophys. Res.*, 95, 4943-4965.

Bevis, M. (1988), Seismic slip and down-dip strain rates in Wadati-Benioff zones, *Sciences, 240,* 1317-1319.

Billen, M. I., M. Gurnis, and M. Simons (2003), Multiscale dynamics of the Tonga-Kermadec subduction zone, *Geophys. J. Int., 153*, 359-388.

Biot, M. A. (1961), Theory of folding of stratified viscoelastic media and its implications in tectonics and orogenesis, *Geol. Soc. Am. Bull., 72*, 1595-1620.

Bostock, M. G., R. D. Hyndman, S. Rondenay, and S. M. Peacock (2002), An inverted continental Moho and serpentinization of the forearc mantle, *Nature, 417*, 536-538.

Burbach, G. V., and C. Frohlich (1986), Intermediate and deep seismicity and lateral structure of subducted lithosphere in the circum-Pacific region, *Rev. Geophys. Space Phys., 24,* 833-874.

Caldwell, J.G., W.F. Haxby, D.E. Karig, and D.L. Turcotte (1976), On the applicability of a universal elastic trench profile, *Earth and Planetary Science Letters*, 31, 2, 239-246.

Chen, W. P., and M. R. Brudzinski (2001), Evidence for a large-scale remnant of subducted lithosphere beneath Fiji, *Science, 292*, 2475-2479.

Chen, Y. L. (1995), A study of 3-D velocity structure of the crust and the subduction

zone in the Taiwan region, 172 pp., *master thesis* (in Chinese), National Central University.

Chiao, L. Y. (1993), Strain segmentation and lateral membrane deformation rate of the subducted Ryukyu slab, *The Island Arc*, 2, 94-103.

Chiao, L. Y., H. Kao, S. Lallemand, and C. S. Liu (2001), An alternative interpretation for slip vector residuals of subduction interface earthquakes: a case study in the westernmost Ryukyu slab, *Tectonophysics*, 333, 123-134.

Chiu, J.-M., B.L. Isacks, and R.K. Cardwell (1991), 3-D configuration of subducted lithosphere in the western Pacific, *Geophys. J. int., 106*, 99-111.

Chou, H. C., B. Y. Kuo, S. H. Hung, L. Y. Chiao, D. Zhao, and Y. M. Wu (2006), The Taiwan-Ryukyu subduction-collision complex: Folding of a viscoelastic slab and the double seismic zone, *J. Geophys. Res., 111*, B04410, doi:10.1029/2005JB003822.

Christensen, U. R. (1989), Mantle rheology, constitution and convection, in Mantle convection: plate tectonics and global dynamics, in volume 4 of *The fluid mechanics of astrophysics and geophysics*, edited by Peltier, W. R., Gordon and Breach Science Publishers, pp. 595-655, New York.

Christensen, N. I. (1966), Elasticity of ultrabasic rocks, *J. Geophys. Res., 71*, 5821-5931.

Christensen, N. I. (2004), Serpentinites, peridotites, and seismology, *International Gogy Review*, 46, 795-816.

Chu, C. H. (2005), Generation of high-Mg andesites in the Kueishantao volcano, the southernmost part of the Okinawa Trough, 99 pp., Master Thesis (in Chinese), National Taiwan University, Taipei, Taiwan.

Chung, S. L., S. L. Wang, R. Shinjo, C. S. Lee, and C. H. Chen (2000), Initiation of arc magmatism in an embryonic continental rifting zone of the southernmost part of Okinawa trough, *Terra Nova, 12*, 225-230.

Cochran, J. R., An analysis of isostasy in the world's oceans 2. midocean ridge crests (1979), *J. Geophys. Res.*, 84, 4713-4729.

Deschamps, A., S. E. Lallemand, J. Y. Collot (1998), A detailed study of the Gagua ridge: a fracture zone uplifted during a plate reorganization in the mid-Eocene, *Mar. Geophys. Res., 20*, 403-423.

Deschamps, A., P. Monié, S. Lallemand, S. K. Hsu, and K. Y. Yeh (2000), Evidence for early Cretaceous curst trapped in the Philippine Sea plate, *Earth and Planet. Sci. Lett., 179*, 503-516.

Dziewonski, M.A. and D.L. Anderson (1984) Seismic tomography of the Earth's interior, Am. Sci., pp. 483–493

Engdahl, E. R., R. D. van der Hilst, and R. P. Buland (1998), Global teleseismic earthquake relocation with improved travel times and procedures for depth determination, *Bull. Seismol. Soc. Am., 88*, 722-734.

Escartin, J., G. Hirth, and B. Evans (1997), Effects of serpentinization on the lithospheric strength and the style of normal faulting at slow-spreading ridges, *Earth and Planet. Sci. Lett., 151*, 181-189.

Flügge W. (1975), *Viscoelasticity*, 194 pp., Springer-Verlag, Berlin.

Font, Y., S. Lallemand, and J. Angelier (1999), Etude de la transition entre l'orogene actif de Taiwan et la subduction des Ryukyu apports de la sismicite, *Soc. Geol. Fr*, 170(3), 271-283.

Font, Y., C. S. Liu, P. Schnurle, and S. Lallemand (2001), Constraints on backstop geometry of the southwest Ryukyu subduction based on reflection seismic data, *Tectonophysics, 333*, 135-158.

Fryer, P., C. G. Wheat, and M. J. Mottl (1999), Mariana blueschist mud volcanism: implication for conditions within the subduction zone, Geoloty, 27, 103-106.

Graeber, F. M., and Gunter Asch (1999), Three-dimensional models of P wave velocity and P-to-S velocity ratio in the southern central Andes by simultaneous

inversion of local earthquake data, *J. Geophys. Res., 104*, 20,237-20,256.

Grand, S.P., van der Hilst, R.D. and Widiyantoro, S. (1997) Global seismic tomography: a snapshot of convection in the Earth. GSA Today 7, pp. 1–7.

Grove, T. L., N. Ghatterjee, S. W. Parman, and E. Médard (2006), The influence of H_2O on mantle wedge melting, *Earth Planet. Sci. Lett., 249*, 74-89.

Gudmundsson, O, and M. Sambridge (1998), A regionalized upper mantle (RUM) seismic model, *J. Geophys. Res., 103*, 7121-7136.

Guillot, S., K. H. Hattori, and J. de Sigoyer (2000), Mantle wedge serpentinization and exhumation of eclogites: insights from eastern Ladakh, northwest Himalaya, *Geology, 28*, 199-202.

Hacker, B. R., G. A. Abers, and S. M. Peacock (2003), Subduction factory 1. theoretical mineralogy, densities, seismic wave speeds, and H2O contents, *J. Geophys. Res., 108*(B1), 2029, doi:10.10292001JB001127.

Hasegawa, A., N. Umino, and A. Takagi (1978), Double planed structure of the deep seismic zone in northeastern Japan arc, *Tectonophys., 47*, 43-58.

Hasegawa, A., S. Horiuchi, and N. Umino (1994), Seismic structure of the northeastern Japan convergent plate margin: A synthesis, *J. Geophys. Res., 99*, 22,295-22,311.

Hattori, K. H., and S. Guillot (2003), Volcanic fronts form as a consequence of serpentinite dehydration in the forearc mantle wedge, *Geology, 31*, 525-528.

Hirth, G., J. Escartin, and J. Lin (1998), The rheology of the lower oceanic crust: Implications for lithospheric deformationi at mid-ocean ridges, 291-303, in Faulting and magmatism at mid-ocean ridges, *Geophys. Monog. 106*.

Hsu, S. K. (2001), Subduction/collision complexities in the Taiwan-Ryukyu junction area: tectonics of the northwestern corner of the Philippine Sea plate, *Terr. Atm. Ocean*, Suppl. issue, 209-230.

Horen, H., M. Zamora, and G. Dubuisson (1996), Seismic wave velocities and

anisotropy in serpentinized peridotites form Xigaze ophiolite: abundance of serpentine in slow spreading ridge, *Geophys. Res. Lett., 23*, 9-12.

Houseman, G. A., and D. Gubbins (1997), Deformation of subducted oceanic lithosphere, *Geophys. J. Int., 131*, 535-551.

Hyndman, R. D., and S. M. Peacock (2003), Serpentinization of the forearc mantle, *Earth and Planet. Sci. Lett., 212*, 417-432.

Iwamori, H. (2007), Transportation of H_2O beneath the Japan arcs and its implications for global water circulation, *Chem. Geology, 239*, 182-198.

Kamiya, S., and Y. Kobayashi (2000), Seismological evidence for the existence of serpentinized wedge mantle, *Geophys. Res. Lett., 27*, 819-822.

Kao, H., and R. J. Rau (1999), Detailed structure of the subducted Philippine Sea plate beneath northeast Taiwan: A new type of double seismic zone, *J. Geophys. Res., 104*, 1015-1033.

Kao, H., S. J. Shen, and K. F. Ma (1998), Transition from oblique subduction to collision: Earthquakes in the southernmost Ryukyu arc-Taiwan region, *J. Geophys. Res., 103*, 7211-7229.

Kawakatsu, H. (1986), Double seismic zones: Kinematics, *J. Geophys. Res.*, 91, 4811-4825.

Kawakatsu, H., and S. Watada (2007), Seismic evidence for deep-water transportation in the mantle, *Science, 316*, 1468-1471, doi:10.1126/science.1140855.

Kawamoto, T., and J. R. Holloway (1997), Melting temperature and partial melt chemistry of H_2O-saturated mantle peridotite to 11 gigapascal, *Science, 276*, 240-243.

Kim, K. H., J. M. Chiu, J. Pujol, K. C. Chen, B. S. Huang, Y. H. Yeh, and P. Shen (2005), Three-Dimensional V_P and V_S Structural Models Associated with the Active Subduction and Collision Tectonics in the Taiwan Region, *Geophys. J. Int.,* in press.

King, S. (2001), Subduction zones: observations and geodynamic models, *Physics of*

the Earth and Planet. Int., 127, 9-24.

Kirby, S. (1995), Intraslab earthquakes and phase changes in subducting lithosphere, *Rev. Geophys. 33*, 287-297.

Kirby, S. H., E. R. Engdahl, and R. Denlinger (1996), Instraslab earthquakes and arc volcanism: Dual physical expressions of crustal and uppermost mantle metamorphism in subduction slabs, in *Subduction: Top to bottom, Amer. Geophysc. Union Geophys. Monogr 96*, edited by Bebout et al., 195-214 pp..

Kissling, E., W. L. Ellsworth, D. Eberhart-Phillips, and U. Kradolfer (1994), Initial reference models in local earthquake tomography. *J. Geophys. Res.,* 99, 19635-19646.

Kohlstedt, D. L., B. Evans, and S. J. Mackwell (1995), Strength of the lithosphere: constraints imposed by laboratory experiments, *J. Geophys. Res., 100*, 17,587-17, 602.

Kuo, B. Y., D. F. Forsyth, and E. M. Parmentier (1986), Flexure and thickening of the lithosphere at the east Pacific rise, *Geophys. Res. Lett., 13*, 681-684.

Lambert, I. R. and P. J. Wyllie (1972), Melting of gabbro (quartz eclogite) with excess water to 35 kilobars, with geological applications, *J. Geology, 80*, 693-708.

Lee, C. S., G. J. Shor, L. D. Bibee, R. S. Lu, and T. W. C. Hilde (1980), Okinawa trough: origin of a back-arc basin, *Mar. Geol., 35*, 219-241.

Lee, C. T. A (2003), Compositional variation of density and seismic velocities in natural peridotites at STP conditions: implications for seismic imaging of compositional heterogeneities in the upper mantle, *J. Geophys. Res., 108*(B9), 2441, doi:10.10292003JB002413.

Liang, W.T., Y.H. Liu, and H. Kao (2004), Source Parameters of Regional Earthquakes in Taiwan: January-December, 2002, *Terr. Atm. Ocean, 15,* 727-741.

Lin, J. Y., S. K. Hsu, and J. C. Sibuet (2004), Melting features along the western Ryukyu slab edge (northeast Taiwan): Tomographic evidence, *J. Geophys. Res.,* 109, B12402, doi:10.1029/2004JB003260.

Lin, J. Y., J. C. Sibuet, C. S. Lee, S. K. Hsu, and F. Klingelhoefer (2007), Origin of the southern Okinawa trough volcanism from detailed seismic tomography, *J. Geophys. Res., 112,* B08308, doi:10.1029/2006JB004703.

Lin, S.C., L.Y. Chiao and B.Y. Kuo (2002), Dynamic interaction of cold anomalies with the mid-ocean ridge flow field and its implications for the Australian–Antarctic Discordance, *Earth and Planet. Sci. Lett.*, 203, 925-935.

Ma, K. F., J. H. Wang, and D. Zhao (1996), Three-dimensional seismic velocity structure of the crust and uppermost mantle beneath Taiwan, *J. Phys. Earth, 44*, 85-105.

Mallet, J.L. (1989), Discrete smooth interpolation, *Transactions on Graphics*, 8, 2, 121-144.

Mallet, J.L. (2002), *Geomodeling*, New York, Oxford University Press, 624 pp.

McGuire, J. J., and D. A. Wiens (1995), A double seismic zone in New Britain and the morphology of the Solomon plate at intermediate depths, *Geophys. Res. Lett., 22*, 1965-1968.

Nakajima, J., Y. Takei, and A. Hasagawa (2005), Quantitative analysis of the inclined low-velocity zone in the mantle wedge of northeastern Japan: A systematic change of melt-filled pore shapes with depth and its implications for melt migration, *Earth and Planet. Sci. Lett., 234*, 59-70.

Peacock, S. M., P. E. van Keken, S. D. Holloway, B. R. Hacker, G. A. Abers, and R L. Rergason (2004), Thermal structure of the Costa Rica-Nicaragua subduction zone, Phys. Earth and Planet. Int., 149, 187-200.

Pavlis, G. L. and J. R. Booker (1980), The mixed discrete-continuous inverse problem; application to the simultaneous determination of earthquake hypocenters and velocity structure. *J. Geophys. Res.,* 85[9], 4801-4810.

Peacock, S. M. (2003), Thermal structure and metamorphic evolution of subducting slabs, in Inside the subduction factory, *Amer. Geophys. Union Geophys. Monogr.*

138, edited by Eiler, 7-22 pp.

Peacock, S. M. (2001), Are the lower planes of double seismic zones caused by serpentine dehydration in subducting oceanic lithosphere, *Geology, 29*, 299-302.

Peacock, S.M., and K. Wang (1999), Seismic Consequences of Warm Versus Cool Subduction Metamorphism: Examples from Southwest and Northeast Japan, *Science*, 286, 937-939

Pysklywec, R. N., J. X. Mitrovica, and M. Ishii (2003), Mantle avalanche as a driving force for tectonic reorganization in the southwest Pacific, *Earth and Planet. Sci. Lett., 209*, 29-38.

Ranero, C. R., J. Phipps Morgan, K. Mcintosh, and C. Reichert (2003), Bending-related faulting and mantle serpentinization at the middle America trench, *Nature, 425*, 367-373.

Rau, R. J., and F. T. Wu (1995), Tomographic imaging of lithospheric structure under Taiwan, *Earth and Planet. Sci. Lett., 133*, 517-532.

Schmalholz, S. M., and Y. Podladchikov (1999), Buckling versus folding: importance of viscoelasticity, *Geophys. Res. Lett., 26*, 2641-2644.

Schnurle, P., C. S. Liu, S. Lallemand, D. Reed (1998), Structural insight into the south Ryukyu margin: effect of the subducting Gagua ridge, *Tectonophysics, 288*, 237-250.

Schurr, B., G. Asch, A. Rietbrock, R. Trumbull, and C. Haberland (2003), Complex patterns of fluid and melt transport in the central Andean subduction zone revealed by attenuation tomography, *Earth Planet. Sci. Lett., 215*, 105-119.

Seno, T., and S. Maruyama (1984), Paleogeographic reconstruction and origin of the Philippine Sea, *Tectonophysics, 102*, 53-84.

Seno, T., S. Stein, and A. E. Gripp (1993), A model for the motion of the Philippine Sea Plate consistent with NUVEL-1 and geological data. *J. Geophys. Res., 98*,

17,941-17,948.

Seno, T., and Y. Yamanaka (1996), Double seismic zones, compressional deep trench-outer rise events, and superplumes, *Geophysical Monograph*, 96, 347-355.

Shinjo, R., (1999), Geochemistry of high Mg andesites and the tectonic evolution of the Okinawa Trough-Ryukyu arc system, *Chem. Geol., 157,* 69-88.

Sibuet, J. C., J. Letouzey, F. Barbier, J. Charvet, J. P. Foucher, T. W. C. Hilde, M. Kimura, L. Y. Chiao, B. Marsset, C. Muller, and J. F. Stephan (1987), Back-arc extension in the Okinawa trough, *J. Geophys. Res., 92*, 14,041-14,063.

Sibuet, J. C., B. Deffontaines, S. K. Hsu, N. Thareau, J. P. Le Formal, C. S. Liu, and the ACT party (1998), Okinawa trough back-arc basin: early tectonic and magmatic evolution, *J. Geophys. Res.*, 103, 30,245-30,267.

Stachnik, J. C., G. A. Abers, and D. H. Christensen (2004), Seismic attenuation and mantle wedge temperatures in the Alaska subduction zone, *J. Geophys. Res., 109*, B10304, doi:10.1029/2004JB003018.

Tamura, Y., Y. Tatsumi, D. Zhao, Y. Kido, and H. Shunkuno (2002), Hot fingers in the mantle wedge: new insights into magma genesis in subduction zones, *Earth Planet. Sci. Lett., 197*, 105-116

Tatsumi, Y., and S. Eggins (1995), *Subduction zone magmatism*, 211 pp., Blackwell, Cambridge.

Teng, L. (1990), Geotectonic evolution of late Cenozoic arc-continent collision in Taiwan, *Tectonophys., 183*, 57-76.

Thurber, C. H. (1983), Earthquake locations and three-dimensional structure in the Coyote Lake area, central California, J. Geophys. Res., 88, 8226– 8236.

Thurber, C. H. (1993), Local earthquake tomography: Velocities and Vp/Vs-theory, in Seismic Tomography: Theory and Practice, edited by H. M. Iyer and K. Hirahara, pp. 563– 583, Chapman and Hall, New York.

Thurber, C. H., and D. Eberhart-Phillips (1999), Local earthquake tomography with flexible gridding, Comput. Geosci., 25, 809–818

van der Hilst, R., and T. Seno (1993), Effects of relative plate motion on the deep structure and penetration depth of slabs below the Izu-Bonin and Marian island arcs, *Earth and Planet. Sci. Lett., 120*, 395-407.

van der Hilst, R.D., Widiyantoro, S. and Engdahl, E.R. (1997) Evidence for deep mantle circulation from global tomography. Nature 386, pp. 578–584.

Van Keken, P. E., B. Kiefer, and S. M. Peacock (2002), High-resolution models of subduction zones: implications for mineral dehydration reactions and the transport of water into the deep mantle, *Geochem. Geophys. Geosyst., 3*(10), 1056, doi:10.1029/2001GC000256.

Vielzeuf, D., and M. W. Schmidt (2001), Melting relations in hydrous systems revisited: application to metapelites, metagreywackes and metabasalts, *Contrib. Mineral. Petrol., 141*, 251-267.

Walck, M., (1988), Three-dimensional V_P/V_S variations for the Coso region, California, *J. Geophys. Res., 93,* 2047-2052.

Waldhauser, F. and W. L. Ellsworth (2000), A double-difference earthquake location algorithm: Method and application to the northern Hayward fault. *Bulletin of the Seismological Society of America*, 90, 1353-68.

Wang, K., and G. C. Rogers (1994), An explanation for the double seismic layers north of the Mendocino triple junction, *Geophys. Res. Lett., 21*, 121-124.

Wang, K., S. L. Chung, S. Y. O'Reilly, S. S. Sun, R. Shinjo, and C. H. Chen (2004a), Geochemical constraints for the genesis of post-collisional magmatism and the geodynamic evolution of the northern Taiwan region, *J. Petrology, 45*, 975-1011.

Wang, T. K., S. F. Lin, C. S. Liu, and C. S. Wang (2004b), Crustal structure of the southernmost Ryukyu subduction zone: OBS, MCS and gravity modeling,

Geophys. J. Int., 157, 147-163.

Watts, A. B., An analysis of isostasy in the world's oceans 1. Hawaiin-Emperor seamount chain (1978), *J. Geophys. Res., 83*, 5989-6004.

Wessel, J. K., and H. F. Smith (1991), Free software helps map and display data, *EOS trans. AGU*, *72*, 441, 445-446.

Wiens, D. A., and S. Stein (1984), Intraplate seismicity and stresses in young oceanic lithosphere, *J. Geophys. Res., 89*, 11,442-11,464.

Wolfe, C., G.M. Purdy, D.R. Toomey, and S.C. Solomon (1995), Microearthquake characteristics and crustal velocity structure at 29°N of the Mid-Atlantic Ridge: The architecture of a slow spreading segment, *J. Geophys. Res.*, 100, 24449-24472.

Wu, F. T., C. S. Chang, and Y. M. Wu (2004), Precisely relocated hypocenters, focal mechanisms and active orogeny in Central Taiwan, in *Aspects of the tectonic evolution of China*, edited by Fletcher et al., special pub., 226, 333-354.

Yamaoka, K., Y. Fuako, and M. Kumazawa (1986), Spherical shell tectonics: effects of sphericity and inextensibility on the geometry of the descending lithosphere, *Rev. Geophys. Space Phys., 24,* 27-55.

Yamasaki, T., and T. Seno (2003), Double seismic zone and dehydration embrittlement of the subducting slab, *J. Geophys. Res., 108*(B4), 2212, doi:10.1029/2002JB001918.

Yeh, Y. H., C. H. Lin, and S. W. Roecker (1989), A study of upper crustal structures beneath northeastern Taiwan: Possible evidence of the western extension of Okinawa trough, *Proc. Geol. Soc. China, 32,* 139-156.

Zhao, D., A. Hasegawa, and S. Horiuchi (1992), Tomographic imaging of *P* and *S* wave velocity structure beneath northeastern Japan, *J. Geophys. Res. 97*, 19,909-19,928.

Zhao, D., K. Wang, G. C. Rogers, and S. M. Peacock (2001), Tomographic image of low *P* velocity anomalies above slab in northern Cascadia subduction zone, *Earth,*

Planet. Space, 53, 285-293.

Zhao, D., Z. Wang, N. Umino, A. Hasegawa (2009) Mapping the mantle wedge and interplate thrust zone of the northeast Japan arc. *Tectonophysics,* 467, 89-106.

Zhao, D., Y. Xu, D. A. Wiens, L. Dorman, J. Hiderbrand, and S. Webb (1997) Depth extento f the Lau back-arcs preadingc enter and its relation to subduction processes, *Science*, 278, 254-257

.

The Taiwan-Ryukyu subduction-collision complex: Folding of a viscoelastic slab and the double seismic zone

Han-Chiang Chou,[1,2] Ban-Yuan Kuo,[3] Shu-Huei Hung,[1] Ling-Yun Chiao,[4] Dapeng Zhao,[5] and Yih-Min Wu[1]

Received 5 May 2005; revised 14 October 2005; accepted 22 December 2005; published 20 April 2006.

[1] The termination of the Ryukyu trench against Eurasia and the oblique subduction of the Philippine Sea plate create a subduction-collision complex offshore Taiwan, which has not previously been elucidated in detail. We combine traveltime data from the seismic networks in Taiwan and Japan to better illuminate how the subducting Ryukyu slab deforms in this subduction-collision zone. More than 5000 events recorded by both networks were relocated with the double-difference method using an optimal regional one-dimensional velocity model. The offshore seismicity indicates that the double seismic zone, with a gap of 15–20 km, exists in the subducting slab in the depth range of 40–80 km. Focal mechanisms suggest that the double seismic zone is caused by east-west compression resulting from oblique convergence. The improved hypocentral locations for the first time reveal folding of the slab into a horizontal curvature larger in magnitude than and opposite in sign to that of the Ryukyu trench in the depth range 50–100 km. The anomalous curvature, together with the focal mechanisms, suggests that the slab folds against the Eurasian lithosphere and that this deformation cannot be fully elastic. We model this deformation mode as the developing instability of a viscoelastic Maxwell layer embedded in a viscous medium. The characteristic wavelength of the instability, i.e., ~250 km, is consistent with folding of a slab whose viscosity is 100 times higher than that of the surrounding mantle for an along-strike elastic membrane strain as small as 0.01, or more than 3 orders of magnitude higher if 5% elastic strain is allowed.

Citation: Chou, H.-C., B.-Y. Kuo, S.-H. Hung, L.-Y. Chiao, D. Zhao, and Y.-M. Wu (2006), The Taiwan-Ryukyu subduction-collision complex: Folding of a viscoelastic slab and the double seismic zone, *J. Geophys. Res.*, *111*, B04410, doi:10.1029/2005JB003822.

1. Introduction

[2] The global seismicity distribution provides a three-dimensional (3-D) portrait of each subduction zone in the mantle [e.g., *Chiu et al.*, 1991; *Engdahl et al.*, 1998]. These images demonstrate that the subducting slab largely inherits the geometric characteristics of the oceanic lithosphere formed on the surface of the Earth and tends to avoid additional extensibility or in-plane deformation [*Burbach and Frohlich*, 1986; *Yamaoka et al.*, 1986]. This implies that for a slab thousands of kilometers in lateral dimension but only tens of kilometers in thickness, the preferred mode of deformation is flexure instead of in-plane deformation. However, there are suggestions that flexure and large membrane deformation may occur simultaneously on regional to local scales in subducting slabs [e.g., *Bevis*, 1988]. In effect, the flexure mode of deformation produces changes in dip angle and/or the subducting flow field of the slab [*Chiao*, 1993]. Changes in the boundary forces that exert on the slab, such as the variations in the rates of trench migration and the impedance of the transition zone to deep penetration also distort the slab in three dimensions, introducing additional curvature to the slab geometry [e.g., *van der Hilst and Seno*, 1993; *Chen and Brudzinski*, 2001; *Pysklywec et al.*, 2003]. These deformations, however, are many hundreds to even thousands of kilometer along the strike of the trench, which can adequately be depicted using the seismicity data determined by the global network [*Gudmundsson and Sambridge*, 1998; *Engdahl et al.*, 1998].

[3] Several factors have to be in place favorably for the subducting slab to deform on scales of a few hundred km or less along its strike in the shallow mantle. The applied forces in the mantle have to be relatively localized or exerting on the slab in such a way to promote small-scale flexure. The rigidity of the slab sets a lower bound for the flexural wavelengths, so a thinner and warmer slab is prone to deflection than a stronger, older slab. The yield envelope governed by both friction and power laws [e.g., *Kohlstedt et al.*, 1995] delimits stresses in the slab, allowing for larger

[1]Institute of Geosciences, National Taiwan University, Taipei, Taiwan.
[2]National Cing Shuei Senior High School, Taichung, Taiwan.
[3]Institute of Earth Sciences, Academia Sinica, Taipei, Taiwan.
[4]Institute of Oceanography, National Taiwan University, Taipei, Taiwan.
[5]Geodynamic Research Center, Ehime University, Matsuyama, Japan.

0148-0227/06/2005JB003822$09.00

curvature for the same bending moment. Finally, the seismic data have to be accurate enough to characterize the deformation within hundreds of km in scale. Global seismicity data are likely to be aliased by limitations from the magnitude threshold of events and the global velocity model that are used, and are not up to the task. There are potential regions in which slabs are soft and subject to tectonic forces that may cause small-wavelength deformation but the global seismicity data fall short of resolving it.

[4] This study focuses on one of such potential regions: the westernmost 100 km of the Ryukyu subduction zone where the trench terminates against the Taiwan island at the surface and the slab against the Eurasian lithosphere at depths. Because of the increasingly high obliquity of subduction and the juxtaposing of the Eurasian lithosphere sideways, subduction is progressively superimposed with collision. In this relay zone northeast of Taiwan, the complex seafloor morphology and sediments obscure how the trench curves toward its western end, leaving no clue to project the shape of the slab below. Up-to-date, depiction of the slab in this region has been conducted with great limitations. Attempts based on the seismicity extracted from the global data set [*Engdahl et al.*, 1998] portray smooth, featureless structure [e.g., *Lin et al.*, 2004]. Because the zone is almost entirely offshore the island, use of the land-based network data risks systematic mislocation. From the geometrical viewpoint, several stations of the Japan network located on the westernmost islands of the Ryukyu arc provide a crucial constraint from the east of the relay zone. Unfortunately, joint seismological efforts between the two networks have not been realized to their full capacity in the past. It remains question as to whether the slab keeps intact in geometry as portrayed by previous studies when it edges toward the Eurasia.

[5] We combine data from Taiwan and Japan networks to relocate earthquakes in the 150-km-wide subduction-collision relay zone. The relocation process consists of necessary steps to assure minimum bias from either networks and to suppress the effects of three-dimensional heterogeneity. From the better determined seismicity in this study, a double seismic zone (DSZ) has been identified at intermediate depths throughout the onshore-offshore region, indicating that the DSZ imaged by *Kao and Rau* [1999] beneath the northern Taiwan extends eastward by at least 100 km. In addition, we observe a mild yet systematic deviation of slab geometry from that projected from the Ryukyu trench, and from that drawn previously based on either the global data set or the data of the Taiwan network [*Kao et al.*, 1998; *Hsu*, 2001]. Different modes of deformation in the relay zone may exist. In a kinematic consideration, *Chiao et al.* [2001] proposed an eastward rotation of subduction flow field to release the along-arc strain. While this rotation mode may exist, we establish a folding mode through the high-resolution slab geometry. We formulate an instability problem in which a viscoelastic layer is subject to compression to interpret under what rheological regime the folds take up the shape depicted by the relocated seismicity.

2. Taiwan-Ryukyu Subduction-Collision Complex

[6] The Ryukyu subduction zone has intimately engaged in the tectonic evolution of the northern segment of the Taiwan orogenic belt [e.g., *Sibuet et al.*, 1998] (Figure 1). Evolution of the volcanism both offshore and on land in the northern Taiwan is complicated but is ultimately derived from the back-arc spreading and upwelling in the mantle wedge behind the Ryukyu arc [*Wang et al.*, 2004a]. The mantle wedge beneath the western Ryukyu has not been imaged properly because of the poor coverage of seismic stations, except perhaps for the northern Taiwan where on-land seismic stations make such imaging geometrically possible [*Lin et al.*, 2004]. It is generally believed that the Okinawa Trough, the back-arc basin of the subduction system, extends into the northeastern corner of Taiwan, exerting a local extensional tectonism to the collisional regime of orogeny. The curvature of the trench has a maximum magnitude at the central segment on the order of 0.002 km^{-1}, on the same order of the magnitude of 0.001 km^{-1} of the Mariana. The small curvature throughout much of the trench favors a largely two-dimensional structure without significant along-strike deformation. The Philippine Sea plate (PSP) converges with the Eurasia at about 70 mm/yr along N50°W direction in this region (Figure 1) [*Seno et al.*, 1993]. The convergence is at high angle to trench for the eastern half of the trench, and that angle progressively decreases toward the west. Within a few hundred kilometers nearshore Taiwan, the angle becomes less than 20°, which signals a significant change of regional stress field with respect to the slab. In this zone, horizontal compression prevails as suggested by earthquake focal mechanisms [*Kao et al.*, 1998], and collision becomes the major force that could reshape the slab.

[7] In this ~100-km-wide subduction-collision relay zone, a few key problems remain perplexing. The Gagua ridge apparently intrudes into the trench at about 123°E (Figure 1), and the slab on the west of the Gagua ridge plunges more steeply than on the east [e.g., *Deschamps et al.*, 2000]. The origin of the ridge and its interaction with the overriding plate during subduction have been investigated [*Deschamps et al.*, 1998; *Schnurle et al.*, 1998]. The age of the western Philippine basin is important to the estimation of the mechanical strength and thermal structure of the Ryukyu slab, but has not yet been settled. The age of 40 Ma is estimated from the plate reconstruction model of *Seno and Maruyama* [1984]. Aided by dating of the gabbro samples, *Deschamps et al.* [2000] proposed a much older (>100 Myr) age for the Huatung basin, the portion of the PSP between Taiwan and the Gagua ridge. However, because the subduction is not straight north, most of the Huatung basin is on the course of collision with Taiwan and will never be subducted under the Ryukyu trench unless the plate motions change dramatically in the future (Figure 1). For the slab geometry, both teleseismic seismicity [*Engdahl et al.*, 1998] and the local earthquakes located by the Central Weather Bureau (CWB) Seismic Network of Taiwan have been selected to depict the Ryukyu slab in previous studies [*Kao and Rau*, 1999; *Font et al.*, 1999]. The CWB hypocenters exhibit smooth slab geometry that is no different from an extrapolation of the slab from the east [e.g., *Kao et al.*, 1998]. The slab contours shown by *Font et al.* [1999] using CWB data may reflect either inaccurate hypocenters or topographic features rather than flexure of a mechanical lithosphere. As noted above, a joint determination of seismicity from networks of Taiwan and Japan is

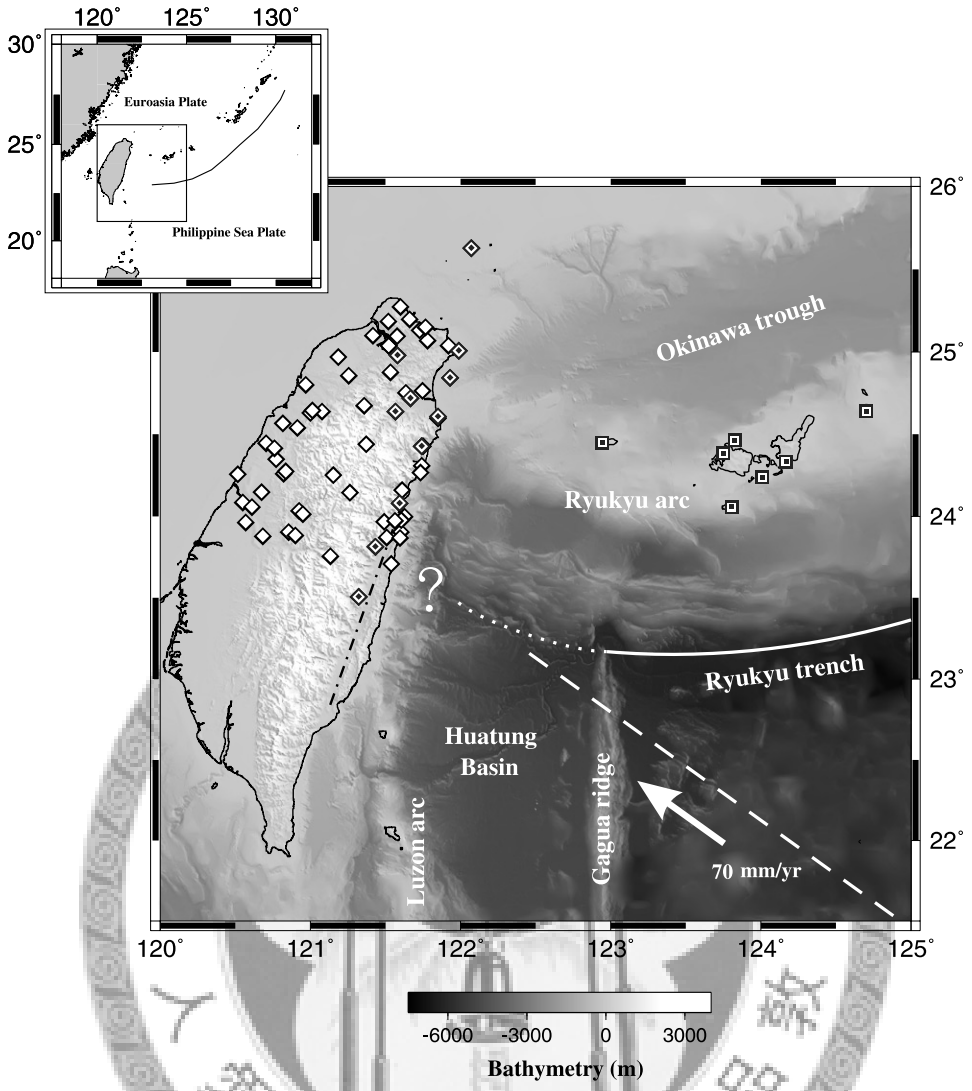

Figure 1. Map showing tectonic setting of the Taiwan-Ryukyu subduction-collision zone and the seismic stations used for relocation of earthquakes in this study. Major tectonic features are labeled. The 11 CWB stations (solid diamonds) and 7 JMA stations (solid squares) form a network covering the subduction-collision relay zone. For onshore events, the 11 CWB stations are joined by other CWB stations (open diamonds) to implement another network covering entire northern Taiwan. The Ryukyu trench has a general trend of southward convexity (white solid dotted line and black line in the inset) but loses its identification when nears Taiwan. Dashed line marks the hypothetical boundary, in the northeast of which the PSP will be subducted beneath the trench in the future. This boundary is parallel to the plate motion (arrow) [after *Seno et al.*, 1993]. The dash-dotted line running along the east coast of Taiwan marks the suture between the PSP and the Eurasia. Collision between the PSP and the Eurasian plate is taking place along this boundary and its northern extension in the upper mantle.

desirable. One of such attempt was made by *Hsu* [2001], which, with limited number of data from the Japan Meteorological Agency (JMA), represents a first step toward a comprehensive integration of data from the two networks.

[8] The crustal structure of the PSP at the forearc basin north of the trench has been investigated with multichannel/ocean bottom seismometry data by *Wang et al.* [2004b]. The resultant velocity model provides a glimpse of the physical state of the lithosphere at the onset of subduction. The 3-D velocity images show that the forearc basement warps in the arc-parallel direction, which is considered as evidence for buckling of the PSP lithosphere against the continental margin at Taiwan [*Wang et al.*, 2004b]. It is unknown whether this is a crustal signature or representative of the mechanical behavior of the entire PSP. In addition, the oceanic crust is thickened to ~10 km beneath the forearc in their model, but no further constraint exists at greater depths. Whether buckling or thickening persists in the subducting slab depends on whether the end barrier against the oblique subduction exists at greater depths and how the slab propagates flexure downward mechanically.

[9] *Kao and Rau* [1999] discussed the origin of the DSZ manifested in cross sections of CWB hypocenters onshore northern Taiwan, and recognized the horizontal compres-

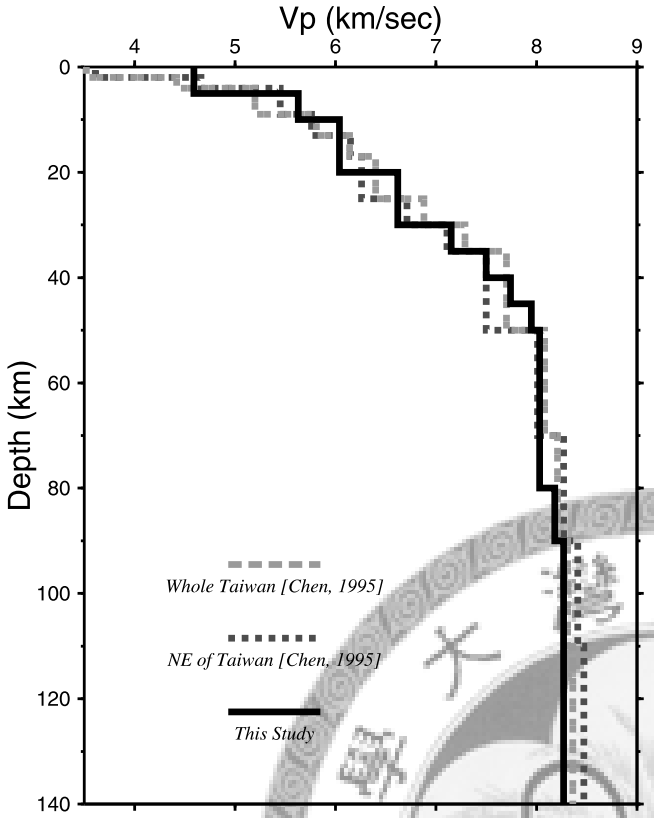

Figure 2. One-dimensional velocity model (solid line) determined by this study with the joint CWB-JMA data set and a manipulation to project the hypocenter effect away from the velocity determination. This model is used for the subsequent double-difference relocation. *Chen*'s [1995] subregional model for northeastern Taiwan is shown in comparison (dotted line). The similarity implies the dominance of slab structure in both.

sion as the tectonic stresses that are responsible for the double planed events. The authors interpret the formation of DSZ by drawing an analogy between oceanic slab and continental lithosphere, with the gap (defined to be 10–20 km) representing the ductile oceanic lower crust sandwiched between the brittle upper crust and upper mantle. The authors label it type II DSZ to distinguish it from those that have typically been associated with bending-unbending of the slab at greater depths, or type I. In this study, we identify DSZ throughout much of the offshore region, and analyze the pros and cons of both the "jelly sandwich" and the metamorphic reactions interpretations.

3. Data and Methods

[10] We first target more than 6000 earthquakes with magnitude greater than 4 that occurred during 1991–2003 initially located between 121.5 and 124.0°E and between 23.5 and 26.0°N. Eleven CWB stations near the northeast coast of Taiwan and seven westernmost stations of JMA were selected to geometrically bracket the relay zone (Figure 1). These earthquakes have been recorded by at least two CWB stations and two JMA stations to ensure a minimum level of even distribution of stations relative to events. The absolute arrival times were provided by the operators of both networks, and there are a total of 74,403 *P* and 60,952 *S* times to start with. Tomographic inversions have been conducted from the relocated events, and will be the subject of a separate report.

[11] The procedure of relocation is described below. The initial locations are taken from the CWB catalog, which is based on an average 1-D model of Taiwan determined by *Chen* [1995]. We then relocate these events using the combined CWB-JMA data and *Chen*'s [1995] subregional model for the northeastern Taiwan. To obtain a 1-D model that better represents the broader land-offshore region, we employ the technique of *Kissling et al.* [1994], which simultaneously inverts for the 1-D velocity structure and the hypocentral parameters, but to quench the latter using the projection operator method of *Pavlis and Booker* [1980] and only invert for the velocity model. The process decouples the velocity determination from the hypocentral effect, enhancing the independence of the former. The resultant 1-D model is shown in Figure 2. We do not use more in-land CWB stations for offshore events to avoid additional crustal heterogeneity in constructing our 1-D model for the relay zone. *Chen* [1995] also used the work by *Kissling et al.* [1994] for the CWB data but did not separate velocity from hypocentral effects. Her model for the northeast Taiwan is compared with our expanded land-offshore model in Figure 2. The discrepancy is not dramatic, implying that the deep structures of both models are dominated by the subducted PSP. Despite the fact that it is the case in the present study, we emphasize that it is always necessary to isolate the hypocentral effect from determination of the velocity model when secondary structures of the slab are pursued. Velocities below 150 km are relatively less well constrained in both models in Figure 2.

[12] We next use the double-difference method of *Waldhauser and Ellsworth* [2000] to relocate the hypocenters east of 121.5E using the 1-D model obtained above with the 11 CWB stations and 7 JMA stations. Then, we scan all the CWB events from 120.5 to 122°E to sort out those that are not relocated. These events include dropouts from the first round relocation due to lack of JMA constraint and new events that do not fall in the region for the first relocation, and are mostly onshore and well within the CWB network. They were then relocated using some 30 CWB stations in northern Taiwan, including the 11 stations in previous step (Figure 1). In this second round of relocation for mostly onshore events, we still use the velocity model specific for the offshore region to retain consistency in velocity model for the latter joint interpretation. Moreover, we are interested more in the subduction zone structure than the crust of Taiwan; as described below, the double-difference approach reduces the near station heterogeneity effects such that differences in shallow crustal velocity between models are not critical. Both rounds of double-difference relocation achieved greater than 70% variance reduction in differential traveltimes.

[13] The double-difference algorithm minimizes the residuals of the differential times between hypocentral pairs. It works efficiently for relative locations between multiplets, sparing the need for station corrections. We adopt it in this study to relocate regional earthquakes by minimizing the effect of crustal and mantle heterogeneities, in that the 3-D

velocity anomalies picked up by the Fresnel zone of each of the paired ray paths to a common station are suppressed by the differential times. The key parameter here is thus the radius, r_0, within which each event seeks to pair with neighboring events to form the differential times. In regional problems, r_0 should be set to correlate with the scale of heterogeneity relative to the Fresnel zone of the waves. It may risk higher chance of contamination from velocity heterogeneities if a larger value is used. Small r_0 ensures suppressed heterogeneity effect, but suffers from relocating events with limited number of differential times. For deeper events, the Fresnel zones of the paired path are less separated beneath the stations than for shallow events, allowing for a larger r_0. We focus on the slab structure and adopt $r_0 = 30$ km. Use of $r_0 = 20$ km does not produce different results because the average distance of pairing for each event is much smaller than r_0. The number of event pairing at the depth range of 50–150 km is several tens to over 100. The number drops to around 10 below 150 km. The maximum and minimum numbers of pairing in this study are set to be 100 and 8, respectively. Some deeper events are too isolated to have enough pair-wise observations, and have therefore been discarded. After the double-difference relocation, the number of events reduces to 5667 and the numbers of *P* and *S* arrivals to 69760 and 57412, respectively.

[14] The merit of the double-difference relocation in a 1-D velocity model versus the 3-D corrected, "single" difference approach for regional and teleseismic studies is debatable. The choice between the two lies in our confidence in the 3-D tomographic model used for the 3-D correction. While no difficulty in detecting the existence of the subducting slab convincingly, the tomographic inversions are usually highly underdetermined, and the result severely weighted and smoothed [e.g., *Ma et al.*, 1996; *Rau and Wu*, 1995]. Moreover, shallow structures in these tomographic models are loosely constrained. Recently, *Kim et al.* [2005] systematically evaluated the effects of station correction in imaging the crust of Taiwan. This model presents improved constraint on the shallow structure and consequently the crust below, which may serve as a starting model for 3-D earthquake locating. Offshore crust and upper mantle, however, are not covered in their study. On the basis of our experiences in earthquake relocation and 3-D tomographic inversion using the combined CWB and JMA data, we believe that the tomography-based 3-D correction is probably premature for the studied region despite it could be the ultimate goal. *Wu et al.* [2004] also used double-difference method to locate events throughout Taiwan to probe the internal structure of the orogen.

[15] In this paragraph we assess how different timing systems of the two networks may affect hypocentral locations. The records of the JMA stations used in this study are time tagged at the stations, while the CWB data are stamped with GPS times at the CWB data center after the data are telemetered from each station. It has been optimistically assumed that the delay due to telemetry is negligible, and therefore the magnitude of delay has not been quantified at least for stations in northern Taiwan. To examine its effect on our results, we analyze the differences in *P* arrival times recorded by two collocated stations, the CWB station NWF and the broadband station WFSB which employs local time tagging, for events in 1999–2004. Statistics of the *P* arrival differences shows a mean of 0.03 s and a standard deviation of 0.02 s. Because NWF and WFSB are the only collocating stations in northern Taiwan, we assume that this statistics is representative. We estimate whether delays of this amount throughout the network cause severe bias in locations when data of the two networks are merged. To do this, the CWB arrival times were shifted earlier by a random number that is characterized by a mean of 0.03 s and a standard deviation of 0.02 s before merging with the JMA times. The double-difference relocation was then performed with this test data set to obtain a new hypocenter distribution. This new distribution is very similar to the original one, and consequently both the geometry of the slab and the first-order seismogenic structures entertained in sections 4–6 remain the same. We conclude that the time-tagging process operated by CWB does not bias the hypocenters significantly with respect to the features concerned in the present study.

4. Results: Slab Geometry and Seismogenic Pattern

[16] Distribution of earthquakes is shown in a sequence of horizontal slices at various depths (Figure 3). The seismicity in the uppermost 20 km reflects stresses in the PSP lithosphere and the overriding Eurasian plate, and seems to bundle with the tectonic elements of the trench system. The trench-parallel pattern mirrors the morphological fabrics of the trench [cf. *Font et al.*, 2001, Figure 1]. In the Okinawa trough, shallow seismicity is aligned with the spreading axis of the back-arc basin that apparently juxtaposes against the northeastern coast of Taiwan (Figure 3, 0–15 km). Down from the depth of 50 km, the seismicity delineates the geometry of the subducting slab. To visualize how the slab deforms, we picked the northernmost events at each 10-km depth interval and 0.1° longitude interval to represent the upper boundary of the slab and form a 3-D data set. Obvious outliers are ruled out. The rationale behind this representation is the knowledge that events do occur in the crust of the slab, making them good proxy of the surface of the slab. We then fit this data set with a surface using the software GOCAD [*Mallet*, 1989, 2002]. GOCAD employs least squares fitting of points in 3-D to a surface under the regularization of minimum curvature and gradient. If seismic gaps exist in the data set, they will be filled by this regularization requirement. We also experimented a different way of representing the slab upper surface. Instead of taking the northernmost event in a narrow interval, the three northernmost events in each 0.25 longitude interval were averaged, and no "outliers" were removed before fitting with GOCAD. The two different approaches produce very similar slab geometry, and the result of the first is shown in 3-D perspectives in Figure 4.

[17] The depth contours of the GOCAD surface are also plotted with the epicenters in Figure 3 from 45 to 115 km depths to illustrate how plate flexes along its strike. Note the depth contour may not match exactly the seismicity boundary in each cross section because the fitting is constructed in 3-D which is a robust way to describe the slab surface compared with the 2-D fitting of earthquakes in each depth interval. At roughly 123°E, a group of events extrudes from the average strike of the slab in the vicinity, most likely

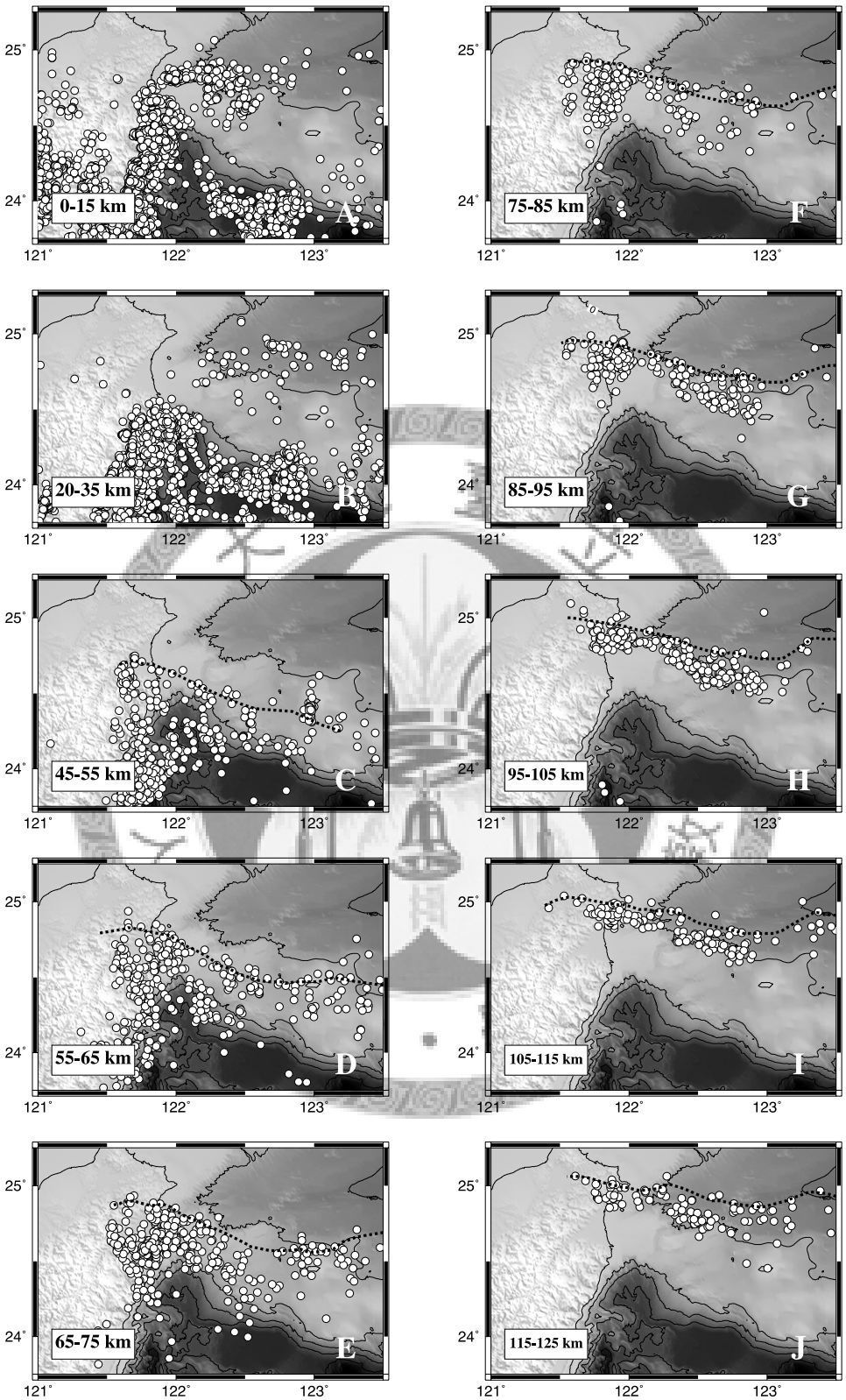

Figure 3. Depth slices showing relocated earthquakes (open dots), with the depth interval annotated. The depth contours (black dotted lines) are taken from the 3-D slab surface model in Figure 4 at the central depth of each interval. The slab contours generally follow the trend of the Ryukyu trench. Near the western boundary in the depth range 45–95 km, however, the slab shows a revered curvature with respect to the trench (C to G).

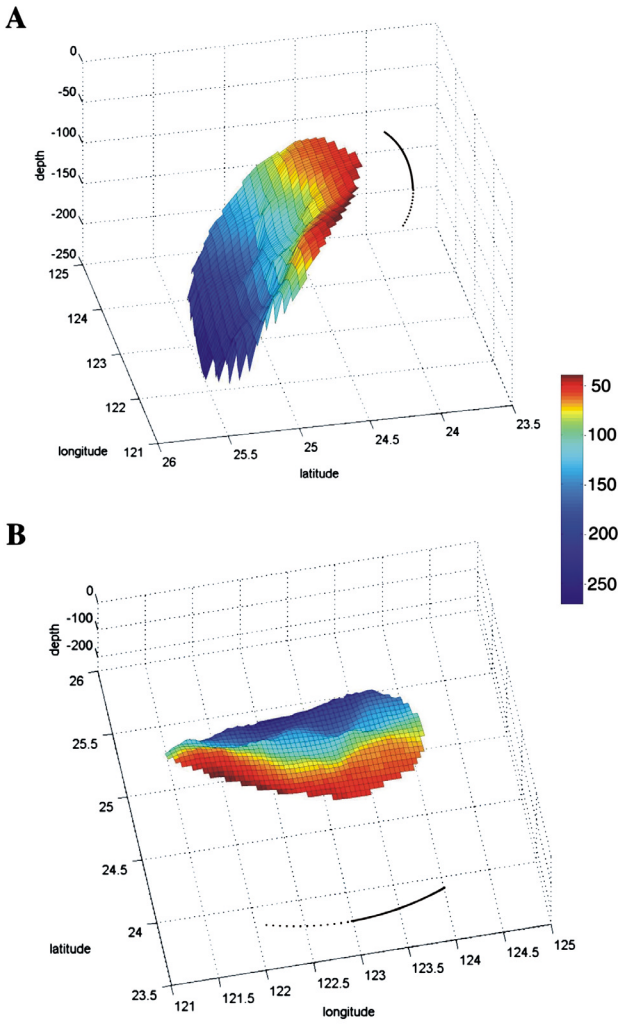

Figure 4. The 3-D slab surface model fit using GOCAD software, shown in two different perspectives. (a) From northwest to see the face of the slab. The folding over the western section creates a bulge at intermediate depths that leads to a greater dip angle of the slab below. (b) A look that grazes along the surface of the slab from south to north subparallel to the slab dip. In both Figures 4a and 4b, folding near the western boundary is evident in comparison with the trace of the trench (solid and dotted lines in Figures 4a and 4b).

representing a topographic structure such as a seamount or even part of the nearby Gagua ridge. The slab surface we determined apparently skips this seismic structure (e.g., Figure 3, 45–55 km). The contours are generally subparallel to the trench, except for the bend over in the westernmost 50 km over the 45- to 95-km depth range. This structure is significant in that it bends reversely with respect to the general trend of the Ryukyu trench (Figure 4).

[18] To examine whether this feature is robust, we add random errors of 5 km to both epicenter and focal depth of each earthquake and fit this "contaminated" data set using GOCAD with both schemes of representation. The bulge near the western end of the slab remains prominent in the new GOCAD surface. To falsely produce such bulge, the events in the westernmost 50 km over a few tens of kilometer depth range must be systematically displaced by 5–10 km toward south: a scenario considered unlikely under the tight constraint provided by the dense land stations in northern Taiwan. Although visually mild in both Figures 3 and 4, the bulge is characterized by an along-strike horizontal curvature κ_h of 0.02–0.04 km^{-1} at the peak of the bend over, much larger than the "background" curvature of 0 to -0.002 km^{-1} measured for the western 1/3 of the Ryukyu trench. As another reference, the curvature of the strongly curving Mariana trench in the vicinity of the midpoint along the strike has a magnitude of only 0.001 km^{-1}. The observed curvature for the western Ryukyu slab is significant not only for its magnitude but also for its opposite sign to that of the Ryukyu trench. As analyzed in section 5, its relatively short wavelength is also unique.

[19] The curvature is related to the elastic bending strain by $\varepsilon(z) = -(z - h/2) \cdot \kappa$, where z is depth from the top surface of the elastic plate with a thickness h. Taking the average κ measured normal to the slab dip to be 0.04 km^{-1} and a conservative h of 15 km, the strain at the upper surface of the plate $\varepsilon(0) = \sim 0.3$, which is too large for an elastic plate. Continual brittle failure allows for smaller elastic strain with apparently larger curvature, but the upper portion of the slab still experiences horizontal tension in this scenario, in contradiction with the focal mechanisms that show east-west oriented compression and a downdip tension for the slab [*Kao and Rau*, 1999; *Liang et al.*, 2004] (see below). This suggests that the slab in the westernmost Ryukyu subduction zone responds elastically only to the horizontal compression, rather than to the tension implied by the curvature. We advocate that the slab folds to a large extent viscously to form the bulge in horizontal sections, with a timescale independent of the compressional brittle failure. We return to this mechanism and explore under what condition it may work in section 5 with a viscoelastic formulation.

[20] Five vertical cross sections were taken in directions normal to the local strike of the slab in the depth range of 50–100 km and are shown in Figure 5. As far as the vertical profiles can discern (Figure 5), the slab kinks (vertically) between 50 and 80 km in profiles A, B, and C, and kinks at depths shallower than 40 km and straightens downdip from 50 to 150 km in profiles D and E. The 3-D model in Figure 4 shows that the bulging is a 3-D structure that is part of the fold of the slab seen in horizontal cross sections described in the preceding paragraphs. As a result, the dip of the slab below 80 km increases toward the west. In contrast to *Deschamps et al.* [2000], who report the average dip difference across the Gagua ridge, the relocated hypocenters resolve secondary variations in the dip of the slab west of the Gagua ridge.

[21] Another prominent feature about the Wadati-Benioff zone is the DSZ, which appears over most of the vertical sections in the relay zone. There are substantial along-strike variations in the DSZ configuration. The DSZ is more ambiguous on profile B than on other profiles where the DSZ depth extents are variable. The two planes appear to converge in profile C, but such convergence is not clear elsewhere. In general, the gap of the DSZ is 15–20 km wide from 40 to 80 km depths. The depth extend is short

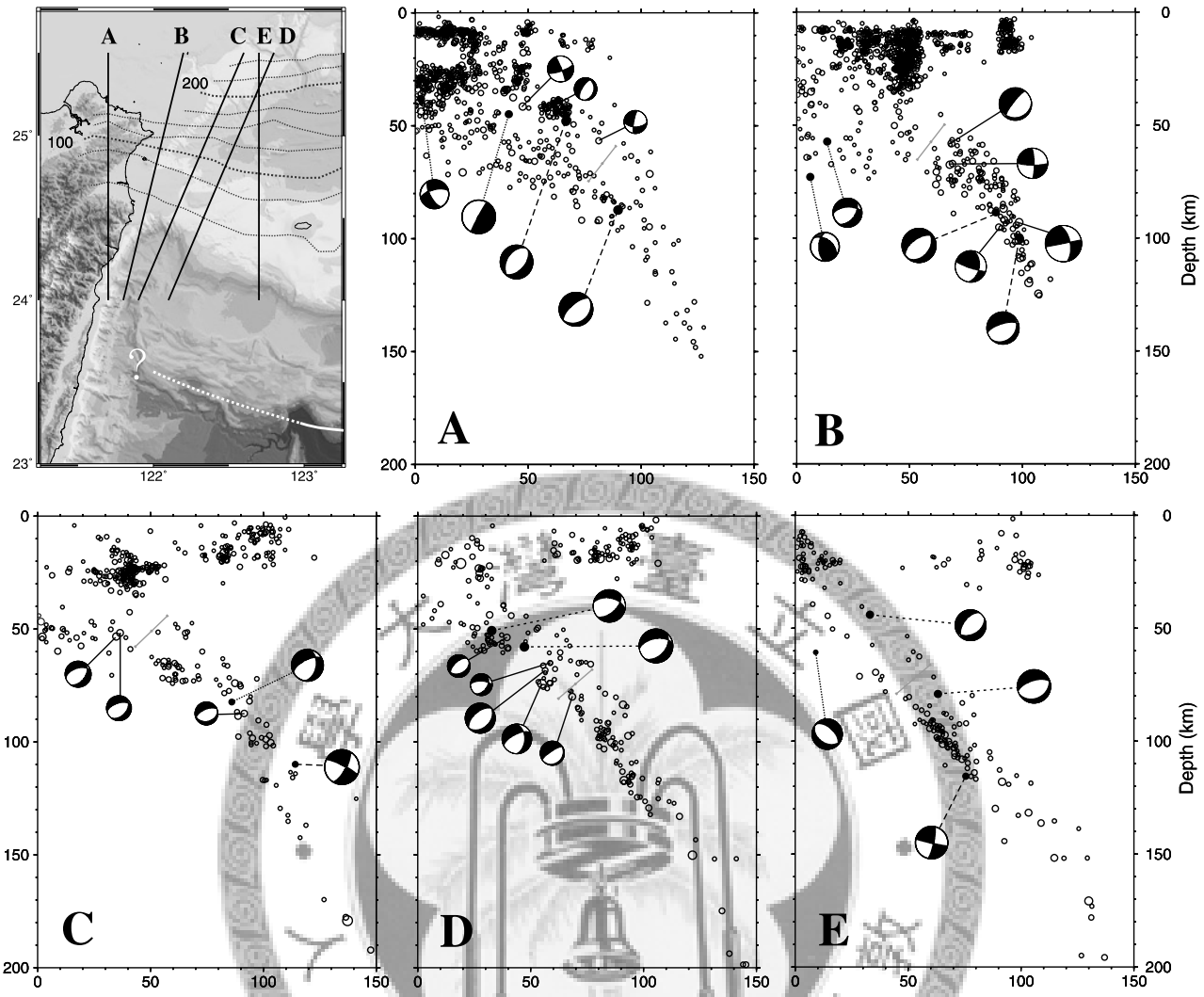

Figure 5. Wadati-Benioff zone in different vertical cross sections whose locations are shown in the upper left panel. Thin and thick dotted lines in black are depth contours of the slab surface taken from the 3-D model in Figure 4, and each profile is taken to be perpendicular to the strike of the slab at shallow depths (<100 km). White solid and dotted lines are traces of the Ryukyu trench the same as in Figure 1. In profiles A, B, and C, the slab apparently bends/unbends vertically between 50 and 80 km such that its dip below is increased relative to that in profiles D and E. The DSZ morphology varies substantially across profiles, but overall two planes are separated by 15–20 km, as indicated by the 20-km-long ruler with 10-km ticks. Side projection focal mechanisms from *Liang et al.* [2004] (solid line connection), *Kao and Rau* [1999] (dashed line), and the Harvard database (dotted line) show minor variation, with a consistent component of along-strike, east-west oriented compression between 50 and 100 km (the white quadrant contains *P* axis). The DSZ extends from onshore to offshore for at least 100 km.

compared with the DSZ in the subduction zone beneath the northeast Japan [*Hasegawa et al.*, 1994]. It is hard to distinguish which plane, the upper or the lower, terminates first and which plane continues downdip. The focal mechanisms determined by *Kao et al.* [1998], *Liang et al.* [2004], and the Harvard Centroid-Moment Tensor (CMT) [e.g., *Dziewonski et al.*, 1981] primarily show along-strike compression in both the upper and the lower plane of the DSZ, indicating that at least the brittle part of the subducting slab is subject to one consistent stress field. Departure from the along-strike compression exists, e.g., focal mechanisms in profiles A and B show coexistence of slab-parallel and slab-normal *P* axes, probably owing to local stress change where slab deforms significantly. Along-strike folding could relax the compression, causing a switch of compression axis from slab parallel to slab normal. Despite this, the overall pattern of focal mechanisms supports our assertion that the DSZ and the folding of the slab originate from the same horizontal compressive forces, and that folding develops mainly viscously.

5. Folding of the Slab

[22] Note from Figure 4 that the horizontal folding persists over about 50 km downdip, not an artifact fortuitously determined by a single profile at a particular depth.

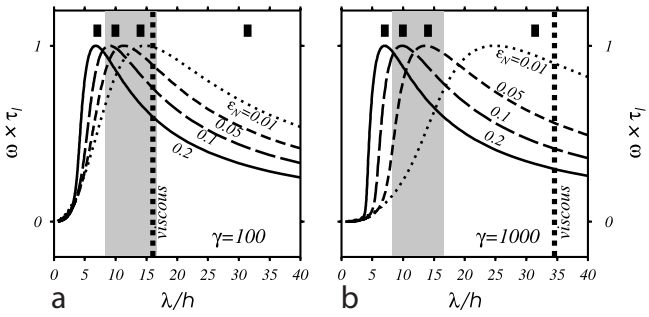

Figure 6. Predicted nondimensionalized amplification $\omega_1 \times \tau_l$ as a function of wavelength for (a) $\gamma = 100$ and (b) $\gamma = 1000$ and for the elastic strain $\varepsilon_N = 0.01$ (dotted lines), 0.05 (short dashed lines), 0.1 (long dashed lines), and 0.2 (solid lines). The amplification functions are normalized to 1. The dominant wavelength for a viscous layer (vertical dotted line) is a function of γ only, and is approximated by the viscoelastic layer at small ε_N. The dominant wavelength of an elastic buckling is a function of ε_N, indicated by the short vertical bars near the top of Figures 6a and 6b for ε_N = 0.2, 0.1, 0.05, and 0.01 from left to right. Pure viscous folding barely explains the observation (shaded region) with $\gamma = 100$ (or smaller), and a pure elastic slab requires strain >0.04. Both are inadequate in explaining the status of stress of the slab.

The earthquake mechanisms and magnitude of curvature suggest to us that the slab responds to the lateral compression elastically with brittle failure but viscously to develop large curvature. The former is characterized by a timescale of seconds and the latter by a much longer timescale on the order of hundred thousands to millions of years. We simulate this deformation scenario as a viscoelastic layer embedded in a viscous medium, in that folding results from instability that grows most efficiently at particular wavelengths controlled by the rheology contrast between the layer and the medium as well as the magnitude of the elastic shortening or membrane strain. The critical constraint is thus the wavelength of the dominant member of the fold, λ_d. A spectrum analysis of the slab contours in the corresponding depth range yields $\lambda_d \sim 250$ km. We could as well estimate $\lambda_d/2$ by measuring the distance between the peak of the fold (near the western end) and the "background," or $\lambda_d/4$ by the distance between the peak and the inflection point where $\kappa = 0$. The results are mutually consistent, indicating that the estimate of 250 km is robust. We derive the governing equation of flexure of a thin Maxwell-type viscoelastic layer and the associated instability problem in Appendix A. The flexure equation reads

$$D_v \frac{\partial w''''}{\partial t} + N w'' + \tau_l N \frac{\partial w''}{\partial t} = -4k\mu_m \frac{\partial w}{\partial t} - 4k\mu_m \tau_l \frac{\partial^2 w}{\partial t^2}, \quad (1)$$

where w is the deflection of the layer, t is the time, w'''' denotes $\partial w^4/\partial x^4$, and so forth with x parallel to the layer, N the x-parallel horizontal compressive force per unit perpendicular to x, D_v the viscous rigidity of the layer, τ_l the relaxation time of the flexure of the Maxwell layer, μ_m the viscosity of the medium or the upper mantle, and k the wave number of flexure and of the viscous resistance of the medium. Other parameters are explained in Appendix A.

[23] Following the derivations laid out in Appendix A, it is shown that a Maxwell layer has two components of instability during folding each characterized by an exponential function of time: $\exp(\omega_1 \cdot t)$ with $\omega_1 > 0$, which is unstable and will amplify with time, and $\exp(\omega_2 \cdot t)$ with $\omega_2 < 0$, which is stable and will eventually die out. The amplification $\omega_{1,2}$ is function of the ratio of the viscosity of the layer to the viscosity of the medium $\gamma = \mu_l/\mu_m$, the equivalent elastic membrane strain $\varepsilon_N = N/(E_l^* h)$ (see Appendix A), and the wave number of each fold member k (or wavelength λ). Because we assume that the observed large-amplitude folding results from instability, we focus on ω_1 as a function of wavelength. The nondimensional amplification $\omega_1 \cdot \tau_l$ versus λ/h is shown in Figures 6a and 6b for different values of γ and ε_N. The peak of the amplification function marks the model dominant wavelength λ_d^{obs}/h at which folding preferentially grows.

[24] To establish the observed dominant wavelength λ_d^{obs}/h as the target for modeling, we need to estimate h. Because the gap of the DSZ is 15–20 km, the seismogenic thickness of the slab is probably greater than 20 km (Figure 5). However, h represents the effective mechanical thickness of the viscoelastic layer, and usually is smaller than the seismogenic thickness of the lithosphere [*Cochran*, 1979; *Wiens and Stein*, 1984]. Combined analyses of gravity and topography and mechanical modeling of oceanic lithosphere in the past have indicated that the effective elastic thickness of the oceanic lithosphere ranges from <10 km near mid-ocean ridge [*Cochran*, 1979; *Kuo et al.*, 1986] to 20–30 km in old oceanic basins [*Caldwell et al.*, 1976; *Watts*, 1978]. We assume the lower bound of h to be 15 km, partially reflecting the fact that the slab is heated relative to the lithosphere before subduction, and set the upper bound at 30 km. The range of λ_d^{obs}/h is 8.3–16.7 (Figure 6).

[25] Figure 6 compares models with observations. Because stronger compression is required to fold a more viscous layer, ε_N has to be large for larger γ, and vice versa, to keep λ_d^{mod}/h within the observation domain. Larger ε_N can also be achieved with larger N, smaller h, and lower Young's modulus, but neither of these is under sufficiently tight geophysical constraints. However, the strain is limited by the yield envelope of the slab in the presence of earthquakes. For the compressional yield strength on the order of 500 MPa given by the friction law for the oceanic lithosphere at tens of km depth [e.g., *Kohlstedt et al.*, 1995] and a commonly accepted Young's modulus range of 10^{10}–10^{11} Pa, the elastic strain could range from very small to 0.05. We consider 0.05 the ad hoc maximum of ε_N. It is unlikely that the viscosity of the subducting slab approaches that of the shallow upper mantle as long as the slab continues to plunge without disintegration or strong folding. We assume $\gamma \geq 10$, which, as shown below, is overridden by the lower bound of λ_d^{obs}/h. Permissible set of model parameters may be found in the $\gamma - \varepsilon_N$ diagram

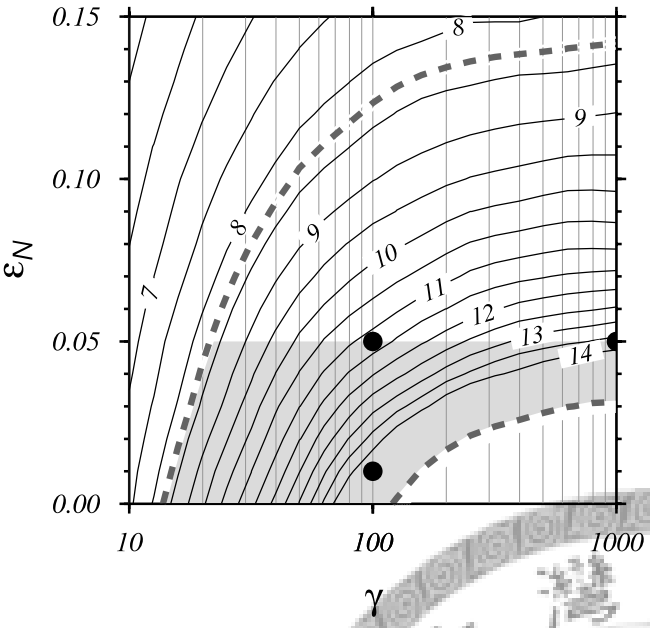

Figure 7. Possible parameter regime of the Maxwell viscoelastic model entertained in this study. Solid contours are model dominant wavelengths nondimensionalized by thickness. The regime (shaded) is delimited by the possible maximum elastic strain ε_N of 0.05 and possible bounds of the observed wavelengths at 8.3 and 16.7 (dashed lines). Higher strains allow for a wide range of viscosity contrast between slab and upper mantle, while for smaller strains only small values of γ are acceptable. Solutions discussed in the text, i.e., $\gamma = 100$, $\varepsilon_N = 0.01$ and 0.05 and $\gamma = 1000$, $\varepsilon_N = 0.05$, are marked by solid squares. Future independent constraints on either parameter will help narrow the permissible model regime.

bounded by $\lambda_d^{obs}/h = 8.3$ and 16.7 and $\varepsilon_N = 0.05$ (Figure 7). As an example, a slab with a viscosity 100 times higher than that of the upper mantle and a 5% horizontal elastic strain is able to fold into a dominant wavelength of 250 km if the effective thickness is slightly greater than ~22 km ($\lambda_d^{obs}/h \sim 11.4$).

[26] Can pure elastic or viscous folding explain the observed dominant wavelength? The Maxwell layer can be reduced to an elastic layer by setting $\tau_l \rightarrow \infty$ (see Appendix A), for which the dominant wavelength of instability decreases as ε_N increases (Figure 6). For the same ε_N, elastic layer predicts broader folds than the Maxwell layer. To buckle an elastic plate into the observed wavelength, ε_N has to be 0.04 or greater. While this is acceptable, elastic buckling is not appealing on the ground that the tensional bending strain it produces contradicts the earthquake mechanisms that show overall compression throughout the thickness of the slab. On the other hand, a viscous layer is obtained when $\tau_l = 0$. The dominant wavelengths in this case approximate the Maxwell folding with small ε_N (Figure 6). This implies that the elastic component in the form of horizontal shortening of the slab assists in developing shorter-wavelength folds. The viscous folding is favorable only for smaller values of γ (Figure 6a), and again it fails to incorporate the elasticity to properly account for the intraslab earthquakes and their compressional focal mechanisms.

6. Discussion

[27] We cannot further narrow the permissible regime of model parameters because the viscoelastic formulation is a simplified approach as well as knowledge of model parameters has been fuzzy. Instead, we choose to draw a broader acceptable model regime in order to explore the tradeoff effect between γ and ε_N and keep the issue open until new independent constraints are available. For a strong slab that is >3 order of magnitude more viscous than the mantle, the in-plane elastic strain ε_N has to be at least 0.04 to explain the observed wavelength (Figure 7). For a weaker slab or lower γ, a wide range of strain is allowed due to the poorly known h. The γ of 100 is considered near the low end of the spectrum [*Houseman and Gubbins*, 1997; *King*, 2001; *Billen et al.*, 2003]. A rule of thumb based on dynamic modeling of Newtonian fluid and power law viscosity is 100°C decrease in temperature leading to roughly 0.5–1 order of magnitude increase in viscosity at mantle temperatures [e.g., *Christensen*, 1989; *Lin et al.*, 2002]. A γ of 100 implies an average temperature contrast of 200°C for Newtonian and 400°C for non-Newtonian fluids. An average temperature anomaly of 200°C is probably hard to reconcile the thermal model for the Ryukyu subduction zone constructed by *Yamasaki and Seno* [2003]. While 400°C seems acceptable, the corresponding non-Newtonian dynamic effect for a subduction zone is not fully understood yet. Perhaps ε_N is the parameter on which constraints may be improved in the future. Estimation of the elastic strain the slab is experiencing from seismological point of view may be a useful step toward pinpointing a solution in our permissible model space [e.g., *Bevis*, 1988].

[28] The DSZ at intermediate depth range (40–150 km) have been observed in several subduction zones [e.g., *Hasegawa et al.*, 1978; *Abers*, 1992; *Kawakatsu*, 1986; *McGuire and Wiens*, 1995]. The upper plane seismicity is thought to occur in the oceanic crust and has been widely accepted to be associated with basalt-eclogite transformation [*Kirby et al.*, 1996; *Peacock and Wang*, 1999; *Peacock*, 2004]. A few hypotheses have been put forth on triggering mechanisms for the lower-plane seismicity [see *Yamasaki and Seno*, 2003], among which the dehydration embrittlement of the serpentinized slab mantle [*Seno and Yamanaka*, 1996; *Peacock*, 2001] suits the depth range discussed in this study. A global survey on the spatial correlation between these metamorphic reactions and the geometry of the DSZ is carried out by *Yamasaki and Seno* [2003]. In their cross sections beneath northern Taiwan, the correlation between the DSZ and the predicted dehydration loci is not clear, although the calculated gap of about 20 km between the two reaction loci matches our observation.

[29] It has been proposed that the serpentinization of the mantle can be made by infiltration of water along the large faults that rupture the upper portion of the lithosphere before subduction, usually on the outer rise [e.g., *Peacock*, 2001]. Tracing opposite the plate motion direction, the section of the PSP lithosphere that would be subducted to the current location of DSZ is to the southeast of the relay zone (Figure 1), where present-day large outer rise events

have been sparse. The only one documented in the Harvard CMT catalog is a M5.7 normal faulting event, which has a standardized centroid depth of 15 km and a source dimension of at most 10 km. Whether serpentinization of the slab interior can be facilitated by a few outer rise faults like this one remains in doubt. In the outer rise region of the Ryukyu trench, in situ imaging of lithosphere that could provide direct evidence for or against deep cutting faults [e.g., *Ranero et al.*, 2003] has not been conducted. Critical supportive evidence for dehydration embrittlement through faulting in this region remains lacking.

[30] *Kao and Rau* [1999] invoked a jelly-sandwich-type of rheology much like that of the continental lithosphere to explain the DSZ seismogenic pattern in the onshore region (see section 2). While rheology of oceanic lithosphere may be potentially important [e.g., *Wang and Rogers*, 1994], drawing analogy between continental and oceanic lithosphere is risky. The ductility of the oceanic lower crust has been under debate [*Kohlstedt et al.*, 1995; *Eseartin et al.*, 1997; *Hirth et al.*, 1998]. It is common that microearthquakes as well as earthquakes with magnitude up to 4 nucleate at lower crustal depths along and near mid-oceanic ridges [e.g., *Wolfe et al.*, 1995; *Bergman and Solomon*, 1990]. Most importantly, at the depth below 40–50 km, where the DSZ in this study is best identified, high lithostatic pressure prohibits brittle failure if unassisted by elevated pore pressures [e.g., *Kirby*, 1995]. In southern Cascadia where the rheology interpretation was originally put forth for subducting slab [*Wang and Rogers*, 1994], the DSZ is distributed in a much shallower depth range (10–25 km). Another uncertain factor is the thickness of the oceanic crust. In this study, the gap of 15–20 km would, in *Kao and Rau*'s [1999] scenario, represent an oceanic crust 2 or 3 times thicker than normal (~7 km) over a large area on the slab. Up-to-date seismological evidence from the PSP has not been convincing in favor of a much thickened crust of PSP [*Wang et al.*, 2004b]. Thickening the crust magmatically or mechanically by a factor of 2 or 3 is considered less likely to occur. In contrast, the two layers found in southern Cascadia subduction zone are separated by less than 10 km [*Wang and Rogers*, 1994]. Speculations over the origin of the DSZ in the Taiwan-Ryukyu collisional zone should defer until more solid evidence becomes available.

7. Conclusions

[31] Accurately determined 3-D seismicity prompts us to reinterpret the deformation of the Ryukyu slab with better kinematic constraints. The seismicity distribution for the first time reveals folding of the slab in the along-strike direction at the depth range of 50–100 km. The folding is significant in two ways: its curvature is greater in magnitude than and opposite in sign to that of the Ryukyu trench, and its wavelength is relatively short at ~250 km. It suggests that the folding results from the horizontal compression exerting on the slab by the resistance of the Eurasian lithosphere against the oblique subduction of the PSP. Both the focal mechanisms and the large curvature argue in favor of a folding generated by viscoelastic instability. We envision a deformation scenario in which the slab responds to the compression through both brittle failure and viscoelastic folding against the Eurasian lithosphere. A Maxwell-type model is employed to simulate this scenario, and to help constrain acceptable model regime. To fold to the observed wavelengths, the slab could be only ~100 times more viscous than the surrounding mantle for a wide range of in-plane elastic strain, or ≥3 orders of magnitude more viscous if an elastic strain close to 0.05 is allowed. Partly because of the folding, the Wadati-Benioff zone progressively steepens at depths below 80 km as approaching Taiwan. The double-seismic zone is clearly mapped out within the slab in the depth range of 40–80 km throughout much of the subduction-collision zone. The DSZ, with a gap of 15–20 km, is stressed by the same horizontal compression that folds the slab.

Appendix A

[32] We follow the linear operator approach of *Flügge* [1975]. The bending stress and strain for a two-dimensional layer are related by the linear operators:

$$P_l(\sigma) = Q_l(\varepsilon), \tag{A1}$$

where subscript l denotes the operators for layer. Without introducing material properties, the balance between the bending moment, horizontal compression per unit length perpendicular to the direction of compression N, and vertical loading q leads to

$$\frac{h^3}{12} Q_l\left(\frac{\partial^4 w}{\partial x^4}\right) + P_l\left(N\frac{\partial^2 w}{\partial x^2}\right) = P_l(q), \tag{A2}$$

where w is the vertical deflection of the layer, h the thickness of the layer, and x measures horizontal distance in N-parallel direction. For a Maxwell material that responds instantaneously to external stresses followed by a viscous deformation, the contributions from the elastic and viscous parts are summed on strain rate:

$$\dot{\varepsilon} = \frac{\dot{\sigma}}{E_l^*} + \frac{\sigma}{4\mu_l}. \tag{A3}$$

Here each contribution is for a thin plate, and $E_l^* = E_l/(1-\nu^2)$ with E_l the Young's modulus of the layer, and μ_l the viscosity of the layer. With these, the operators are defined as

$$P_l = 1 + \tau_l \frac{\partial}{\partial t}, \quad Q_l = 4\mu_l \frac{\partial}{\partial t}, \tag{A4}$$

where $\tau_l = 4\mu_l/E_l^*$ is the relaxation time of the Maxwell material. Equation (A2) becomes

$$D_v \frac{\partial}{\partial t}\frac{\partial^4 w}{\partial x^4} + N\left(1+\tau_l\frac{\partial}{\partial t}\right)\frac{\partial^2 w}{\partial x^2} = \left(1+\tau_l\frac{\partial}{\partial t}\right)q. \tag{A5}$$

This is the governing equation for bending of a Maxwell layer under transverse loading q and in-plane compression N; $D_v = \mu_l h^3/3$ is the flexural rigidity of a viscous plate.

Equation (A5) reduces to bending of an elastic plate as $\mu_l \rightarrow \infty$ and $\tau_l \rightarrow \infty$:

$$D_e \cdot \frac{\partial^4 w}{\partial x^4} + N \cdot \frac{\partial^2 w}{\partial x^2} = q, \tag{A6}$$

where $D_e = E_l^* h^3/12$ is the flexural rigidity of an elastic plate. Equation (A5) reduces to viscous plate bending as $E_l^* \rightarrow \infty$ and $\tau_l \rightarrow 0$:

$$D_v \cdot \frac{\partial^4 \dot{w}}{\partial x^4} + N \cdot \frac{\partial^2 w}{\partial x^2} = q. \tag{A7}$$

[33] Because external loading is passive in a folding problem, the medium operators link q with deflection w:

$$P_m(q) = Q_m(w). \tag{A8}$$

Assume the deflection w has the form of $w(x, t) = A(t)\sin(kx)$,

$$P_m = 1, \quad Q_m = -4k\mu_m \frac{\partial}{\partial t} \tag{A9}$$

for viscous medium, where μ_m is the viscosity of the medium. Equation (A9) implies that the resistance is proportional to the wavelength at which the layer is folded. Inserting (A8) and (A9) into (A5) to eliminate q, we obtain

$$D_v \frac{\partial w''''}{\partial t} + Nw'' + \tau_l N \frac{\partial w''}{\partial t} = -4k\mu_m \frac{\partial w}{\partial t} - 4k\mu_m \tau_l \frac{\partial^2 w}{\partial t^2}. \tag{A10}$$

The characteristic equation for the solution of the form of $A(t)\sin(kx)$ is

$$4\mu_m \tau_l \frac{\partial^2 A}{\partial t^2} - \left[\tau_l Nk - D_v k^3 - 4\mu_m\right]\frac{\partial A}{\partial t} - NKA = 0, \tag{A11}$$

and $A(t)$ is composed of two terms: $\exp(\omega_1 t)$ and $\exp(\omega_2 t)$ where

$$\omega_{1,2}\tau_l = \frac{\gamma}{8}\left[-b \pm \sqrt{b^2 + c}\right], \tag{A12}$$

where

$$b = \frac{\overline{k}^3}{3} - 4\varepsilon_N \overline{k} + \frac{4}{\gamma}, c = 64\varepsilon_N \frac{\overline{k}}{\gamma}, \tag{A13}$$

and $\gamma = \mu_l/\mu_m$. The normalized wave number $\overline{k} = 2\pi/(\lambda/h)$, and ε_N is defined as

$$\varepsilon_N = \frac{N/h}{E_l^*}, \tag{A14}$$

which approximates the in-plane elastic strain or the membrane strain due to lateral compression. The amplification functions $\omega_1 > 0$ which promotes instability, and $\omega_2 < 0$ which stabilizes perturbations, but the total amplification rate is always greater than zero. The amplification ω_1 can be plotted as a function of normalized wavelength and the wavelength for the dominant member of folding λ_d can be found numerically. The result is consistent with that of *Schmalholz and Podladchikov* [1999].

[34] For the case of an elastic layer embedded in a viscous medium, we start with equation (A6) to derive the dominant wavelength:

$$\frac{\lambda_d}{h} = \pi\left[\frac{1}{\varepsilon_N}\right]^{1/2} \tag{A15}$$

The instability occurs when $\lambda > (1/3)^{1/2}\lambda_d$. For a viscous layer folding in a viscous medium, λ_d can also be expressed analytically:

$$\frac{\lambda_d}{h} = 2\pi\left[\frac{\gamma}{6}\right]^{1/3}. \tag{A16}$$

The derivation of equations (A15) and (A16) is given by *Biot* [1961].

[35] **Acknowledgments.** We thank Tetsuzo Seno, Jer-Ming Chiu, and Geoffrey Abers for their critical reviews. Comments by Stefan Schmalholz, Serge Lallemand, Jean-Claude Sibuet, and Yves Font are appreciated. Discussion with Wen-Tzong Liang led to the important analysis into the CWB time tagging problem. The work is supported by the National Science Council of Taiwan, Republic of China, under grant NSC 94-2116-M-001-015.

References

Abers, G. A. (1992), Relationship between shallow and intermediate depth seismicity in the eastern Aleutian subduction zone, *Geophys. Res. Lett.*, *19*, 2019–2022.

Bergman, E. A., and S. C. Solomon (1990), Earthquake swarms on the Mid-Atlantic Ridge: Products of magmatism or extensional tectonics?, *J. Geophys. Res.*, *95*, 4943–4965.

Bevis, M. (1988), Seismic slip and down-dip strain rates in Wadati-Benioff zones, *Sciences*, *240*, 1317–1319.

Billen, M. I., M. Gurnis, and M. Simons (2003), Multiscale dynamics of the Tonga-Kermadec subduction zone, *Geophys. J. Int.*, *153*, 359–388.

Biot, M. A. (1961), Theory of folding of stratified viscoelastic media and its implications in tectonics and orogenesis, *Geol. Soc. Am. Bull.*, *72*, 1595–1620.

Burbach, G. V., and C. Frohlich (1986), Intermediate and deep seismicity and lateral structure of subducted lithosphere in the circum-Pacific region, *Rev. Geophys.*, *24*, 833–874.

Caldwell, J. G., W. F. Haxby, D. E. Karig, and D. L. Turcotte (1976), On the applicability of a universal elastic trench profile, *Earth Planet. Sci. Lett.*, *31*, 239–246.

Chen, W. P., and M. R. Brudzinski (2001), Evidence for a large-scale remnant of subducted lithosphere beneath Fiji, *Science*, *292*, 2475–2479.

Chen, Y. L. (1995), A study of 3-D velocity structure of the crust and the subduction zone in the Taiwan region (in Chinese), Master thesis, 172 pp., Natl. Cent. Univ., Jhongli City, Taiwan.

Chiao, L. Y. (1993), Strain segmentation and lateral membrane deformation rate of the subducted Ryukyu slab, *Island Arc*, *2*, 94–103.

Chiao, L. Y., H. Kao, S. Lallemand, and C. S. Liu (2001), An alternative interpretation for slip vector residuals of subduction interface earthquakes: A case study in the westernmost Ryukyu slab, *Tectonophysics*, *333*, 123–134.

Chiu, J.-M., B. L. Isacks, and R. K. Cardwell (1991), 3-D configuration of subducted lithosphere in the western Pacific, *Geophys. J. Int.*, *106*, 99–111.

Christensen, U. R. (1989), Mantle rheology, constitution and convection, in *Mantle Convection: Plate Tectonics and Global Dynamics*, *Fluid Mech. Astrophys. Geophys.*, vol. 4, edited by W. R. Peltier, pp. 595–655, Gordon and Breach, New York.

Cochran, J. R. (1979), An analysis of isostasy in the world's oceans: 2. Mid-ocean ridge crests, *J. Geophys. Res.*, *84*, 4713–4729.

Deschamps, A., S. E. Lallemand, and J.-Y. Collot (1998), A detailed study of the Gagua ridge: A fracture zone uplifted during a plate reorganization in the mid-Eocene, *Mar. Geophys. Res.*, *20*, 403–423.

Deschamps, A., P. Monié, S. Lallemand, S. K. Hsu, and K. Y. Yeh (2000), Evidence for early Cretaceous curst trapped in the Philippine Sea plate, *Earth Planet. Sci. Lett.*, *179*, 503–516.

Dziewonski, A. M., T.-A. Chou, and J. H. Woodhouse (1981), Determination of earthquake source parameters from waveform data for studies of global and regional seismicity, *J. Geophys. Res.*, *86*, 2825–2852.

Engdahl, E. R., R. D. van der Hilst, and R. P. Buland (1998), Global teleseismic earthquake relocation with improved travel times and procedures for depth determination, *Bull. Seismol. Soc. Am.*, *88*, 722–734.

Escartin, J., G. Hirth, and B. Evans (1997), Effects of serpentinization on the lithospheric strength and the style of normal faulting at slow-spreading ridges, *Earth Planet. Sci. Lett.*, *151*, 181–189.

Flügge, W. (1975), *Viscoelasticity*, 194 pp., Springer, New York.

Font, Y., S. Lallemand, and J. Angelier (1999), Etude de la transition entre l'orogene actif de Taiwan et la subduction des Ryukyu apports de la sismicite, *Bull. Soc. Geol. Fr.*, *170*(3), 271–283.

Font, Y., C. S. Liu, P. Schnurle, and S. Lallemand (2001), Constraints on backstop geometry of the southwest Ryukyu subduction based on reflection seismic data, *Tectonophysics*, *333*, 135–158.

Gudmundsson, O., and M. Sambridge (1998), A regionalized upper mantle (RUM) seismic model, *J. Geophys. Res.*, *103*, 7121–7136.

Hasegawa, A., N. Umino, and A. Takagi (1978), Double planed structure of the deep seismic zone in northeastern Japan arc, *Tectonophysics*, *47*, 43–58.

Hasegawa, A., S. Horiuchi, and N. Umino (1994), Seismic structure of the northeastern Japan convergent plate margin: A synthesis, *J. Geophys. Res.*, *99*, 22,295–22,311.

Hirth, G., J. Escartin, and J. Lin (1998), The rheology of the lower oceanic crust: Implications for lithospheric deformation at mid-ocean ridges, in *Faulting and Magmatism at Mid-ocean Ridges*, *Geophys. Monogr. Ser.*, vol. 106, edited by W. R. Buck et al., pp. 291–303, AGU, Washington, D. C.

Houseman, G. A., and D. Gubbins (1997), Deformation of subducted oceanic lithosphere, *Geophys. J. Int.*, *131*, 535–551.

Hsu, S. K. (2001), Subduction/collision complexities in the Taiwan-Ryukyu junction area: Tectonics of the northwestern corner of the Philippine Sea plate, *Terr. Atmos. Oceanic Sci.*, suppl. issue, 209–230.

Kao, H., and R. J. Rau (1999), Detailed structure of the subducted Philippine Sea plate beneath northeast Taiwan: A new type of double seismic zone, *J. Geophys. Res.*, *104*, 1015–1033.

Kao, H., S. J. Shen, and K. F. Ma (1998), Transition from oblique subduction to collision: Earthquakes in the southernmost Ryukyu arc-Taiwan region, *J. Geophys. Res.*, *103*, 7211–7229.

Kawakatsu, H. (1986), Double seismic zones: Kinematics, *J. Geophys. Res.*, *91*, 4811–4825.

Kim, K. H., J. M. Chiu, J. Pujol, K. C. Chen, B. S. Huang, Y. H. Yeh, and P. Shen (2005), Three-dimensional V_P and V_S structural models associated with the active subduction and collision tectonics in the Taiwan region, *Geophys. J. Int.*, *162*, 204–220, doi:10.1111/j.1365-246X.2005.02657.x.

King, S. (2001), Subduction zones: Observations and geodynamic models, *Phys. Earth Planet. Inter.*, *127*, 9–24.

Kirby, S. (1995), Intraslab earthquakes and phase changes in subducting lithosphere, *Rev. Geophys.*, *33*, 287–297.

Kirby, S. H., E. R. Engdahl, and R. Denlinger (1996), Instraslab earthquakes and arc volcanism: Dual physical expressions of crustal and uppermost mantle metamorphism in subduction slabs, in *Subduction: Top to Bottom, Geophys. Monogr. Ser.*, vol. 96, edited by G. E. Bebout et al., pp. 195–214, AGU, Washington, D. C.

Kissling, E., W. L. Ellsworth, and U. Kradolfer (1994), Initial reference models in local earthquake tomography, *J. Geophys. Res.*, *99*, 19,635–19,646.

Kohlstedt, D. L., B. Evans, and S. J. Mackwell (1995), Strength of the lithosphere: Constraints imposed by laboratory experiments, *J. Geophys. Res.*, *100*, 17,587–17,602.

Kuo, B. Y., D. F. Forsyth, and E. M. Parmentier (1986), Flexure and thickening of the lithosphere at the East Pacific Rise, *Geophys. Res. Lett.*, *13*, 681–684.

Liang, W. T., Y. H. Liu, and H. Kao (2004), Source parameters of regional earthquakes in Taiwan: January–December, 2002, *Terr. Atmos. Oceanic Sci.*, *15*, 727–741.

Lin, J. Y., S. K. Hsu, and J. C. Sibuet (2004), Melting features along the western Ryukyu slab edge (northeast Taiwan): Tomographic evidence, *J. Geophys. Res.*, *109*, B12402, doi:10.1029/2004JB003260.

Lin, S. C., L. Y. Chiao, and B. Y. Kuo (2002), Dynamic interaction of cold anomalies with the mid-ocean ridge flow field and its implications for the Australian–Antarctic Discordance, *Earth Planet. Sci. Lett.*, *203*, 925–935.

Ma, K. F., J. H. Wang, and D. Zhao (1996), Three-dimensional seismic velocity structure of the crust and uppermost mantle beneath Taiwan, *J. Phys. Earth*, *44*, 85–105.

Mallet, J. L. (1989), Discrete smooth interpolation, *Trans. Graph.*, *8*(2), 121–144.

Mallet, J. L. (2002), *Geomodeling*, 624 pp., Oxford Univ. Press, New York.

McGuire, J. J., and D. A. Wiens (1995), A double seismic zone in New Britain and the morphology of the Solomon plate at intermediate depths, *Geophys. Res. Lett.*, *22*, 1965–1968.

Pavlis, G. L., and J. R. Booker (1980), The mixed discrete-continuous inverse problem; application to the simultaneous determination of earthquake hypocenters and velocity structure, *J. Geophys. Res.*, *85*, 4801–4810.

Peacock, S. M. (2001), Are the lower planes of double seismic zones caused by serpentine dehydration in subducting oceanic lithosphere, *Geology*, *29*, 299–302.

Peacock, S. M. (2004), Thermal structure and metamorphic evolution of subducting slabs, in Inside the subduction factory, in *Inside the Subduction Factory, Geophys. Monogr. Ser.*, vol. 138, edited by J. Eiler, pp. 7–22, AGU, Washington, D. C.

Peacock, S. M., and K. Wang (1999), Seismic consequences of warm versus cool subduction metamorphism: Examples from southwest and northeast Japan, *Science*, *286*, 937–939.

Pysklywec, R. N., J. X. Mitrovica, and M. Ishii (2003), Mantle avalanche as a driving force for tectonic reorganization in the southwest Pacific, *Earth Planet. Sci. Lett.*, *209*, 29–38.

Ranero, C. R., J. Phipps Morgan, K. Mcintosh, and C. Reichert (2003), Bending-related faulting and mantle serpentinization at the middle America trench, *Nature*, *425*, 367–373.

Rau, R. J., and F. T. Wu (1995), Tomographic imaging of lithospheric structure under Taiwan, *Earth Planet. Sci. Lett.*, *133*, 517–532.

Schmalholz, S. M., and Y. Podladchikov (1999), Buckling versus folding: Importance of viscoelasticity, *Geophys. Res. Lett.*, *26*, 2641–2644.

Schnurle, P., C. S. Liu, S. Lallemand, and D. Reed (1998), Structural insight into the south Ryukyu margin: Effect of the subducting Gagua ridge, *Tectonophysics*, *288*, 237–250.

Seno, T., and S. Maruyama (1984), Paleogeographic reconstruction and origin of the Philippine Sea, *Tectonophysics*, *102*, 53–84.

Seno, T., and Y. Yamanaka (1996), Double seismic zones, compressional deep trench-outer rise events, and superplumes, in *Subduction: Top to Bottom*, *Geophys. Monogr. Ser.*, vol. 96, edited by G. E. Bebout et al., pp. 347–355, AGU, Washington, D. C.

Seno, T., S. Stein, and A. E. Gripp (1993), A model for the motion of the Philippine Sea plate consistent with NUVEL-1 and geological data, *J. Geophys. Res.*, *98*, 17,941–17,948.

Sibuet, J. C., et al. (1998), Okinawa trough back-arc basin: Early tectonic and magmatic evolution, *J. Geophys. Res.*, *103*, 30,245–30,267.

van der Hilst, R., and T. Seno (1993), Effects of relative plate motion on the deep structure and penetration depth of slabs below the Izu-Bonin and Marian island arcs, *Earth Planet. Sci. Lett.*, *120*, 395–407.

Waldhauser, F., and W. L. Ellsworth (2000), A double-difference earthquake location algorithm: Method and application to the northern Hayward fault, *Bull. Seismol. Soc. Am.*, *90*, 1353–1368.

Wang, K., and G. C. Rogers (1994), An explanation for the double seismic layers north of the Mendocino triple junction, *Geophys. Res. Lett.*, *21*, 121–124.

Wang, K., S. L. Chung, S. Y. O'Reilly, S. S. Sun, R. Shinjo, and C. H. Chen (2004a), Geochemical constraints for the genesis of post-collisional magmatism and the geodynamic evolution of the northern Taiwan region, *J. Petrol.*, *45*, 975–1011.

Wang, T. K., S. F. Lin, C. S. Liu, and C. S. Wang (2004b), Crustal structure of the southernmost Ryukyu subduction zone: OBS, MCS and gravity modeling, *Geophys. J. Int.*, *157*, 147–163.

Watts, A. B. (1978), An analysis of isostasy in the world's oceans: 1. Hawaiian-Emperor seamount chain, *J. Geophys. Res.*, *83*, 5989–6004.

Wiens, D. A., and S. Stein (1984), Intraplate seismicity and stresses in young oceanic lithosphere, *J. Geophys. Res.*, *89*, 11,442–11,464.

Wolfe, C., G. M. Purdy, D. R. Toomey, and S. C. Solomon (1995), Microearthquake characteristics and crustal velocity structure at 29°N of the Mid-Atlantic Ridge: The architecture of a slow spreading segment, *J. Geophys. Res.*, *100*, 24,449–24,472.

Wu, F. T., C. S. Chang, and Y. M. Wu (2004), Precisely relocated hypocenters, focal mechanisms and active orogeny in central Taiwan, in *Aspects of the Tectonic Evolution of China*, edited by J. Malpas et al., *Geol. Soc. Spec. Publ.*, *226*, 333–354.

Yamaoka, K., Y. Fuako, and M. Kumazawa (1986), Spherical shell tectonics: Effects of sphericity and inextensibility on the geometry of the descending lithosphere, *Rev. Geophys.*, *24*, 27–55.

Yamasaki, T., and T. Seno (2003), Double seismic zone and dehydration embrittlement of the subducting slab, *J. Geophys. Res.*, *108*(B4), 2212, doi:10.1029/2002JB001918.

L.-Y. Chiao, Institute of Oceanography, National Taiwan University, No.1, Sec. 4, Roosevelt Road, Taipei, 106 Taiwan. (chiao@ntu.edu.tw)

H.-C. Chou, S.-H. Hung, and Y.-M. Wu, Institute of Geosciences, National Taiwan University, P.O. Box 13-318, No.1, Sec. 4, Roosevelt Road, Taipei, 106 Taiwan. (d92224001@ntu.edu.tw; drymwu@ntu.edu.tw)

B.-Y. Kuo, Institute of Earth Sciences, Academia Sinica, No.128, Sec. 2, Academia Road, Nankang, Taipei, 115 Taiwan. (byk@earth.sinica.edu.tw)

D. Zhao, Geodynamic Research Center, Ehime University, 2–5, Bunkyo-cho, Matsuyama, 790-8577 Japan. (zhao@sci.ehime-u.ac.jp)

JOURNAL OF GEOPHYSICAL RESEARCH, VOL. 114, B12301, doi:10.1029/2008JB006192, 2009

Tomography of the westernmost Ryukyu subduction zone and the serpentinization of the fore-arc mantle

Han-Chiang Chou,[1,2] Ban-Yuan Kuo,[3] Ling-Yun Chiao,[4] Dapeng Zhao,[5] and Shu-Huei Hung[1]

Received 3 November 2008; revised 23 July 2009; accepted 5 August 2009; published 1 December 2009.

[1] Three-dimensional tomographic images of the subducting Philippine Sea slab and the fore-arc mantle beneath NE Taiwan and the westernmost Ryukyu were generated in this study. More than 5600 events recorded simultaneously by seismic networks in Taiwan and Japan were relocated for the inversion for variations in V_P, V_S, and V_P/V_S. Analysis of the trade-off between the data variance reduction and model variance helps to determine the appropriate strictness for regularization to avoid either overinterpretatioin or underinterpretation of data. The regularization parameters were also chosen to ensure suppression of artificial V_P/V_S anomalies. The subducting slab is characterized by high V_P, high V_S, and intermediate to low V_P/V_S. Notable in the mantle wedge is the high V_P/V_S anomalies that abut the surface of the subducting slab at depths of 30–80 km. The previously identified positive V_P/V_S channel connecting the slab and the arc volcano interpreted to be a melt pathway is not reproduced in this study. We convert V_S and V_P/V_S to perturbations of temperature and serpentinization of the mantle. The slab is cooled by 200°C–400°C relative to the mantle, in accord with the estimates from theoretical modeling of subduction. The serpentinization reaches ~15%, or 2% water content, at 50 km depth in the fore-arc mantle. We interpret the peak serpentinization as hydrated by the water released from the basalt-eclogite metamorphic reaction in the oceanic crust of the subducting Philippine Sea Plate. The spatial limitation of the present seismic networks in this region with respect to subduction zone events hinders a full description of the pattern of melting in much of the mantle wedge. Resolution tests of the tomographic inversion provide a basis to guide our interpretation to better resolved regions.

Citation: Chou, H.-C., B.-Y. Kuo, L.-Y. Chiao, D. Zhao, and S.-H. Hung (2009), Tomography of the westernmost Ryukyu subduction zone and the serpentinization of the fore-arc mantle, *J. Geophys. Res.*, *114*, B12301, doi:10.1029/2008JB006192.

1. Introduction

[2] The Philippine Sea Plate (PSP) is subducting obliquely beneath the Eurasian Plate along the Ryukyu trench with the western end underlying the island of Taiwan. This framework dictates the tectonics of the region. Not only has the PSP motion brought about the collision between the Luzon arc and the Asian continent [e.g., *Teng*, 1990], but also the subduction has nurtured the initiation of the Okinawa trough (OT) [e.g., *Lee et al.*, 1980; *Sibuet et al.*, 1987]. This nascent back-arc opening, in turn, is propagating westward into the NE corner of Taiwan, or the Yilan plain [*Yeh et al.*, 1989; *Sibuet et al.*, 1998] and interacting with the arc-continent collision in shaping the geology and landscape of northern Taiwan. The collision component of the oblique subduction puts the PSP subducting slab (thereby the Ryukyu slab) under an E-W compression state at lithospheric depths as manifested by earthquake focal mechanisms [*Kao et al.*, 1998]. Using data from both the Taiwan Central Weather Bureau (CWB) network and the Japan Meteorological Agency (JMA) network, *Chou et al.* [2006] relocated thousands of earthquakes and delineate the double seismic zone in the Ryukyu slab from Taiwan 200 km to the east. These authors also quantified the mode of deformation of the slab with folding of a viscoelastic plate under the horizontal compression.

[3] One of the most important elements of a subduction zone-mantle wedge system is the active volcanic front (VF) directly linked to the ongoing subduction process. At the northeastern end of the Ryukyu arc, the present-day VF can be clearly defined by tracing the active volcanoes in southern Kyushu, Japan, southwestward, below which the Wadati-Benioff zone (WBZ) reaches about 100 km depth. The spatial character of these volcanoes is consistent with the mantle-wedge dynamic and petrological paradigm [*Tatsumi and Eggins*, 1995]. However, the definition of the active VF in the westernmost Ryukyu arc is not obvious. The islands of Iriomote and Ishigaki, where JMA stations are located, are presently inactive and are only 60 km above the WBZ [e.g.,

[1]Institute of Geosciences, National Taiwan University, Taipei, Taiwan.
[2]Also at National Cing-Shuei Senior High School, Taichung, Taiwan.
[3]Institute of Earth Sciences, Academia Sinica, Taipei, Taiwan.
[4]Institute of Oceanography, National Taiwan University, Taipei, Taiwan.
[5]Department of Geophysics, Tohoku University, Sendai, Japan.

0148-0227/09/2008JB006192$09.00

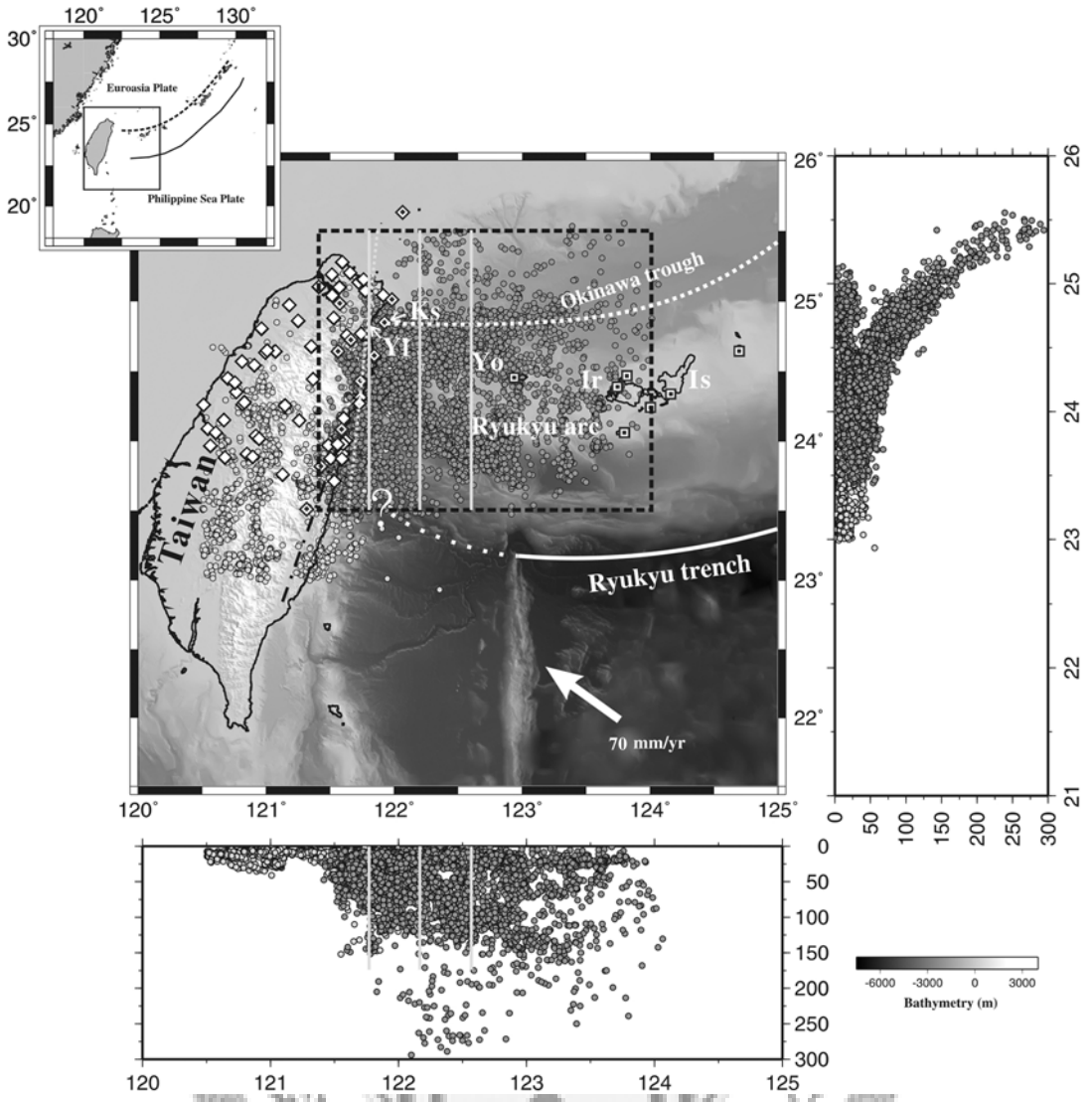

Figure 1. (top left) Index map for the studied region as outlined by the black dashed lines, with local bathymetry, stations, and events. (right) N-S and (bottom) E-W cross sections of seismicity to show subduction zone structures. Seismic stations from the CWB (diamonds) and the JMA (squares) networks form complementary coverage of the region. Filled symbols denote stations used in the joint network inversion. The PSP-Eurasia convergence of 70 mm/yr is shown by the arrow. The western extension of the Ryukyu trench (white line) is ambiguous. The white dotted line in the Okinawa trough indicates the position of the present-day volcanic front [*Chung et al.*, 2000]. Locations of the profiles are denoted as N-S white lines in Figures 1 (top left) and 1 (bottom). Profile 2 of *Lin et al.* [2004] crosses obliquely our 121.8E profile. Ks, Kueishantao; Yl, YiLan Plain; Yo, Yonaguni island; Ir, Iriomote island; Is, Ishigaki island.

Shinjo, 1999]. The present, active VF may lie along a cluster of submerged volcanoes north of these islands, underlain by the Ryukyu slab below ~100 km, with geochemical signatures affiliated with subduction [*Chung et al.*, 2000; *Shinjo*, 1999] (Figure 1). This VF lies mostly south of the axis of the OT, but merges with it when tracked westward to Kueishantao (KST), a 7 ka old andesitic volcano island ~10 km offshore from the coast of the Yilan plain [e.g., *Chung et al.*, 2000; *Chu*, 2005]. The location of the VF is a critical reference in interpreting the tomographic images of the Ryukyu mantle wedge.

[4] This study utilized the CWB-JMA traveltime data with events relocated by *Chou et al.* [2006] to image the slab and the mantle wedge using 3-D seismic tomography. Unlike in Japan where hundreds of land stations are favorably distributed above the subduction zone, most of the westernmost Ryukyu slab lie to the east of the high-density Taiwan network and is covered only by the JMA stations aligned along the Ryukyu arc. This event-station geometry is therefore not overly favorable for imaging the mantle wedge north of the arc. Nonetheless, the joint network approach offers significant advantages regarding offshore areas of Taiwan relative to previous efforts based on CWB alone. The Ryukyu subduction zone beneath northern Taiwan was first imaged with reasonably fidelity by *Rau and Wu* [1995]. Recently, *Lin*

et al. [2004] provided a new model for NE Taiwan using CWB data, while we show in this paper that a joint network approach, despite its uneven aperture toward the east, is helpful to better constrain the structure beneath the margin of the Taiwan network. In a follow-up effort, *Lin et al.* [2007] extended their model to offshore 124°E by incorporating JMA and 12-day OBS data. In addition to the difference in data set, this study differs from *Lin et al.* [2004, 2007] in the inversion strategy and interpretations.

[5] In addition to integration of currently available network data, we emphasize the necessity of achieving the appropriate strictness of the imposed regularization. Despite the impression that the variance reduction versus the model variance trade-off analysis is a routine practice, the discussions concerning the appropriate resolving power of the adopted data sets of regional tomographic studies tend to be downplayed by concealing the actual trade-off pattern. It is thus difficult to clarify whether critical features of a certain tomographic model are in fact effects of either overrepresentation or underrepresentation or interpretation. Examples of possible overinterpretation in previous studies are discussed.

2. Data and Methods

[6] The traveltime data used in this study are the same as that from *Chou et al.* [2006] and are described briefly here. To target the middle zone between Taiwan and Ryukyu, we first selected 11 CWB stations near the NE coast of Taiwan and 7 westernmost stations of JMA as the basis for traveltime data. Events with magnitude 4 or greater within the area from 23.5 to 26.0°N and from 121.5 to 124.0°E registered by at least two stations of each network were selected. This practice avoids overwhelming of the CWB over the JMA data and the potential complications resulting from the highly heterogeneous crust of Taiwan. The final data are selected arrival times reported by both agencies for stations of the joint network. In addition to the data mutually covered by CWB and JMA, a complementary subset of arrival times from the events well within the CWB network in northern Taiwan was also incorporated in the relocation procedure to help illuminate the westernmost edge of the subduction configuration. In all, the data set consists of 7672 relocated events with 74,403 *P* wave and 60,952 *S* wave arrival times.

[7] A preliminary joint inversion for the data set was first executed to determine the hypocentral parameters and the regional one-dimensional (1-D) V_P and V_S structures. The 1-D velocity structure inversion is undertaken by first invoking the projection operator technique that isolates the velocity structure from the hypocentral parameters [*Pavlis and Booker*, 1980]. The vertical velocity profile so obtained is then adopted in the subsequent double difference scheme [*Waldhauser and Ellsworth*, 2000] to relocate all the events. The relocated events better delineate a double-seismic zone, and reveal a fold-like, along-strike deformation of the slab at intermediate depths, possibly rising from impingement with the Eurasian lithosphere [*Chou et al.*, 2006]. The 1-D velocity model is employed as the reference background model for the subsequent 3-D tomography experiments.

[8] The regional traveltime tomography algorithm of *Zhao et al.* [1992] was adopted in this study. Within the area ranging from 23.0 to 26.0°N and from 120.4 to 124.0°E, we constructed a mesh with a horizontal spacing of 0.2° and a vertical spacing of 10 km from the surface to 100 km depth and 20 km from 100 to 200 km depth. We then invert the *P* and *S* traveltimes for V_P and V_S perturbations from the reference 1-D velocity models. Moreover, we sort through the data set and build a subset of travel times from the event-receiver pairs that provide both *P* and *S* arrivals. This subset, consisting of 80% and 98% of the original *P* and *S* sets, respectively, is utilized for the construction of the V_P/V_S model. Notice that

$$\frac{\delta(V_P/V_S)}{(V_P/V_S)} = \frac{V_S\delta V_P - V_P\delta V_S}{V_S^2}\cdot\frac{V_S}{V_P} = \frac{\delta V_P}{V_P} - \frac{\delta V_S}{V_S}. \quad (1)$$

That is, the V_P/V_S anomaly is simply the difference between the V_P and V_S anomalies in fractional form. In other words, robust patterns of $\delta(V_P/V_S)$ perturbations are obtained as long as the constraints invoked to invert for $\delta V_P/V_P$ and $\delta V_S/V_S$ are comparable. This is different from formulations that invert the *P* and *S*-*P* traveltime residuals for the product of $\delta(V_P/V_S)$ and the spatially varying V_P [e.g., *Walck*, 1988], which eventually involves taking ratios of the two inversions. To us, equation (1) can be grasped more intuitively and the algebraic summation of the results from two independent inversions, i.e., $\delta V_P/V_P$ and $\delta V_S/V_S$, is less prone to undesired amplification of the error in each variable than the ratio of two variables. In the Appendix, we devise experiments using the same raypath geometries but with travel times generated from known synthetic structures so that the spatial resolution can be evaluated.

[9] With extensive inversion experiments examining the variance reduction versus the model variance trade-off relation, appropriate damping factors are determined from the trade-off diagram (Figure 2a). The compromise between the model's ability to explain the data and the cost of such ability, i.e., the uncertainty of the model, is reached at the convex portion of the trade-off curves in Figure 2a. Next we test whether the combination of the optimal damping for V_P and V_S is also optimal for V_P/V_S. Figure 2 shows an input model that consists of +8% for a slab and −6% for the overlying mantle in both V_P and V_S. We generate synthetic *P* and *S* travel times for this model for the event-station pairs used in the V_P/V_S inversion, and carry out the inversion as for the real data. According to (1), the same amounts of V_P and V_S fractional anomalies yield a zero V_P/V_S anomaly. Figure 2 shows three combinations of damping all qualified to be "optimal" in the trade-off curves. Among the three examples, the combination in Figure 2d appears to suppress the V_P/V_S anomalies in the mantle more effectively, best matching the zero $\delta(V_P/V_S)$ input model. Less damping in V_P causes more severe a perturbation in V_P, leading to a positive $\delta(V_P/V_S)$, and vice versa, while overdamping of both automatically reduce $\delta(V_P/V_S)$, which is an advantage over the ratio approach. We use the combination in Figure 2d in the inversion and are confident that we will not overinterpret V_P, V_S, and V_P/V_S.

3. Tomographic Models

[10] The tomographic models resulting from the optimal damping indicate that the most predominant features within the area of interest are the high V_P and V_S anomalies associated with the subducting Ryukyu slab down to a depth

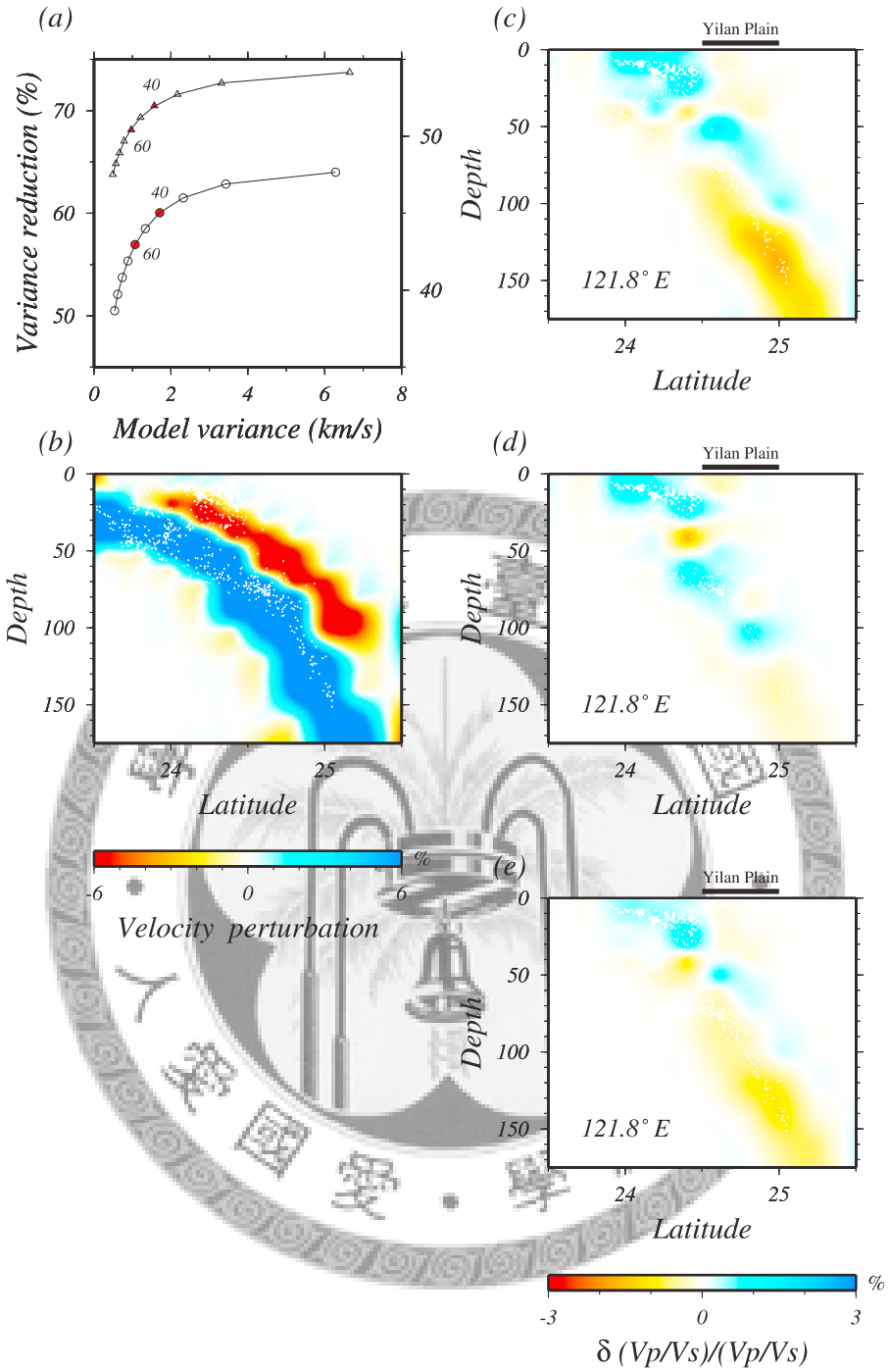

Figure 2. Trade-off tests for V_P, V_S and V_P/V_S. (a) Trade-off curves for V_P and V_S that show compromise between model variance and data variance reduction at the convex portion of the curves. The two values of damping shown are both optimal for individual velocity but may introduce artifact to the ratio of velocities. (b) Input synthetic structure that mimic an exaggerated subduction zone with known zero $\delta(V_P/V_S)$ in both slab and mantle wedge. Inversion outputs are shown with damping (c) 40–40, (d) 40–60, and (e) 60–60 for V_P and V_S, respectively. Artificial nonzero $\delta(V_P/V_S)$ anomalies are created for Figure 2c, and the combinations of the parameters for Figures 2d and 2e suppress the artifacts in both slab and mantle wedge better.

of 150–200 km (Figure 3). We plot the *R*25 line, which delineates the resolving power of 25% as defined in the Appendix, to confine our interpretation in the better resolved regime. Note *R*25 does not guarantee "correct" features, but it is an indicator for what features are worth further examination and what can be disregarded. In this sense only the subduction zone and the neighboring mantle wedge at shallow depths merit interpretation (Figure 3). In addition, the restoration tests in the Appendix show a resolvable scale

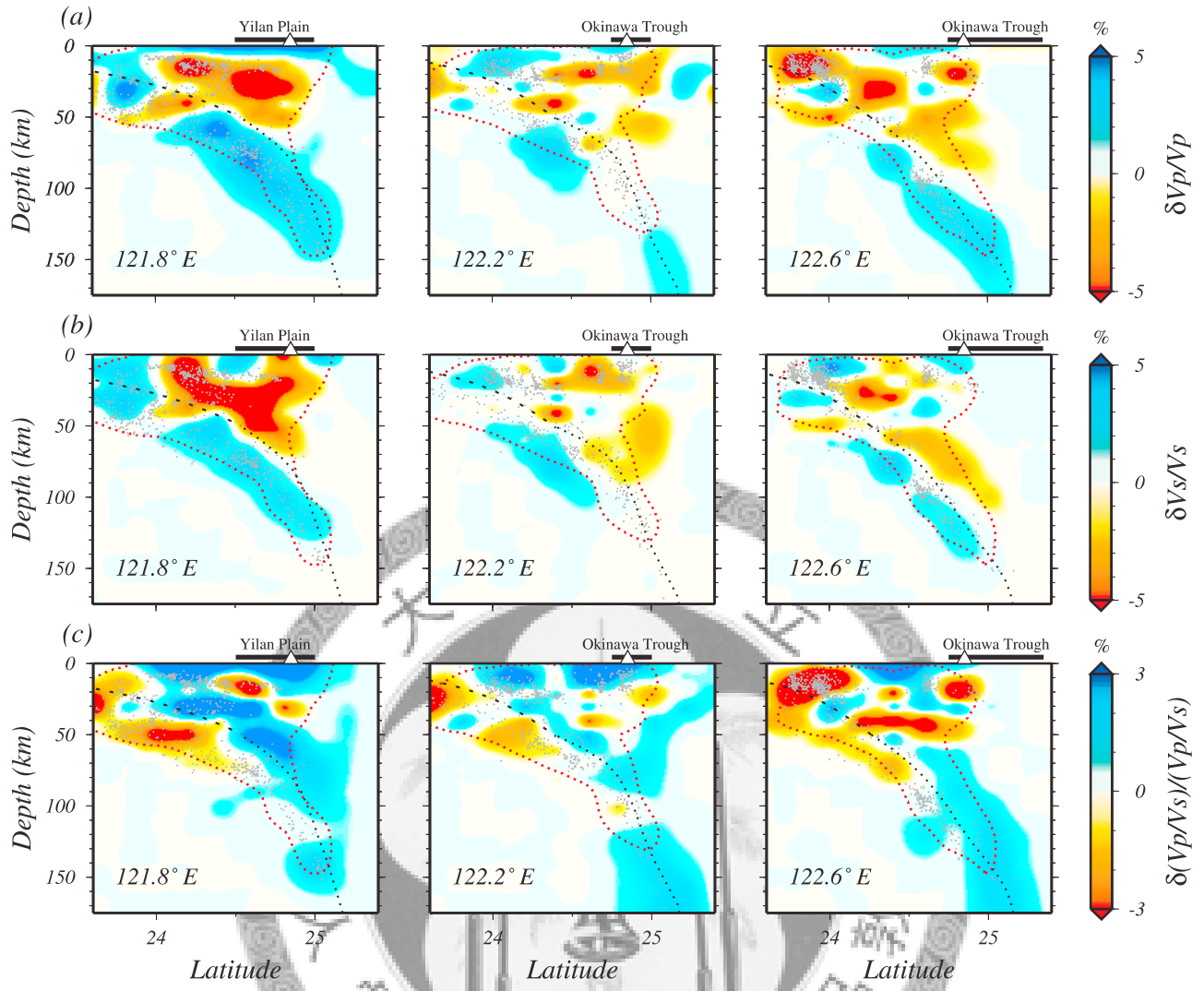

Figure 3. Tomographic images of (a) $\delta V_P/V_P$, (b) $\delta V_S/V_S$, and (c) $\delta(V_P/V_S)/(V_P/V_S)$ shown in three vertical cross sections along longitudes 121.8°E, 122.2°E, and 122.6°E, respectively. *R*25 for V_P is plotted (red dotted line) in each profile to illustrate possible limit of the acceptable recovery of the inversion. The black dotted line is the smoothed slab interface after *Chou et al.* [2006], and the short dashed line is the extrapolation of this interface to the Ryukyu trench at the surface. Locations of relevant tectonic elements are annotated on the top of each diagram. Small triangles represent the VF. Note the slab structure is well resolved only at 121.8°E.

of heterogeneity of 10–20 km in much of the mantle in the *R*25 regime.

[11] The three profiles in Figures 3a and 3b represent typical images of the subduction zone in our model. In the nearshore profile along 121.8°E the slab is resolved to be continuous at 2% perturbation from 50 to 100–150 km depths. Toward the east the slab image is either discontinuous or only continuous at very weak strength (<1%). The disruption of the slab image by neutral or low velocity anomalies below 100 km in the 122.2°E and 122.6°E profiles may result from errors due to uneven distribution of events and stations, and should not be interpreted as a physical break of the slab. Weakened, positive anomalies appear below 150 km, where events exist sparsely (Figure 1). In 121.8°E, there exists a negative anomaly cutting through the shallow segment of the slab at 40–50 km depth beneath 24°N. It is within a broad region of poor 10 km resolution (Figure A1), and the maximum is located near the slab surface in correlation with low seismicity. The strength of this anomaly was solved differently for V_P and V_S, leading to anomalies in V_P/V_S and the parameterized models in the next section. At present we do not have a complete understanding of the origin of this anomaly and we do not interpret it in this study.

[12] In general, the V_P and V_S anomalies in fractional form associated with the subduction zone are similar in amplitude, consistent with a thermal origin because the derivatives with respect to temperature of the two differ only moderately. In the 121.8°E profile, strong negative V_P and V_S anomalies are distributed beneath or close to the Yilan plain (Figures 3a and 3b), and the broad zone of anomaly is avoid of seismicity. As the opening of the OT is thought to propagate westward and has now reached beneath the Yilan plain [*Sibuet et al.*, 1987], the negative anomalies there together with the paucity of seismicity may imply the presence of the relatively hot lower

crust and uppermost mantle in response to the local extensional tectonics. Toward the east where the OT opening is more mature, the correlation of low velocities with the OT is instead not definitive. This is mainly because the OT and the VF progressively move outside the northern limit of the CWB-JMA effective coverage area (Figures 1 and 3).

[13] Because the subducting slab is supposed to be the dominant structure, a reliable model should present a reasonable slab image, and only when the slab is properly imaged do other features on the same profile merit interpretation. We thereafter focus on profile 121.8°E where the slab is resolved to be continuous with realistic velocity anomalies. The most systematic pattern of the positive V_P/V_S perturbation is its juxtaposition with the subducting slab (Figure 3c). It is striking that the dominant features shift from within the slab in V_P and V_S to outside the slab in V_P/V_S. As the synthetic test indicates (Figure 2), the choice of damping for V_P and V_S suppresses amplification of spurious V_P/V_S signature, and therefore the presence of such structure in the model seems warranted. Neutral to negative V_P and V_S with high, positive V_P/V_S anomalies in the mantle wedge have been documented in subduction zones in Japan [*Kamiya and Kobayashi*, 2000], Cascadia [*Zhao et al.*, 2001], and the Andes [*Graeber and Asch*, 1999] through tomographic imaging. *Lin et al.* [2004] also reported low velocities with high V_P/V_S underlying NE Taiwan in their model that bottoms at 60 km depth. High V_P/V_S, together with relatively low V_P and V_S, has been widely interpreted as indicative of hydration of the mantle or in situ melt retention. Water released from the oceanic crust during descending may be absorbed by adjacent mantle peridotite and transform it to serpentinite [*Hacker et al.*, 2003]. This serpentinized layer, if dragged down with the corner flow, will eventually be dehydrated and may trigger water-fluxed partial melting in the wedge [e.g., *Hattori and Guillot*, 2003]. If the wedge is hot enough, water discharged from the subducted crust may facilitate melting in the mantle without an intermediate step of serpentinization [*Arcay et al.*, 2005].

4. Serpentinization

4.1. Parameterization

[14] Our tomographic inversion outputs three types of anomalies, V_P, V_S, and V_P/V_S, with only two of them being independent parameters. V_P/V_S is a more effective indicator of the hydration or melting of a mantle wedge than V_P and V_S alone, and it is independent of either V_P or V_S, but not both. In this section we quantify the effects of hydration of the wedge mantle resulting from dehydration of the subducting crust and slab. Major hydrous minerals in peridotite include serpentine, chlorite, and amphibole. Among these, serpentine dominates the water budget of peridotite [*Schmidt and Poli*, 1998]. In this study, the hydration phenomenon in the fore-arc mantle was parameterized to be the degree of serpentinization of the parent peridotite, Θ. A 100% serpentinite (Θ = 100) has 15 wt% water [e.g., *Hacker et al.*, 2003], and $\Theta = 0$ represents dry peridotite. Water can be provided through subduction by (1) sediment compaction, usually at shallow depths, (2) metamorphic reaction of oceanic crust from blueschist/greenschist to eclogite facies, and (3) dehydration of the previously serpentinized slab mantle at greater depths [*Hyndman and Peacock*, 2003].

[15] We chose V_S and V_P/V_S as the two independent parameters. We take the laboratory measurements of seismic velocities for peridotite serpentinized to various degrees from *Christensen* [1966] and *Horen et al.* [1996]. *Christensen*'s [1966] 2 kbar measurements merge with *Horen et al.*'s [1996] room pressure data well, and the V_P, V_S, and V_P/V_S all display first order linear relationships with Θ. The derivative $d\ln V_S/d\Theta$ of -4.84×10^{-3} is adopted from *Horen et al.* [1996]. The derivative $d\ln(V_P/V_S)/d\Theta$ of 2.254×10^{-3} is determined from a regression of the combined V_P/V_S data provided by *Christensen* [1966] and *Horen et al.* [1996] with a correlation coefficient >0.8. These are one of the two sets of partial derivatives for the degree of serpentinization used in this study and are designated as set I parameters.

[16] *Christensen* [2004] noted that the velocities measured in previous work mainly represent lizardite serpentinite in lower crustal condition rather than antigorite serpentinite stable usually in the fore-arc mantle. Without having the exact data to do regression, we digitized *Christensen*'s [2004] Figure 8 and obtained the following partial derivative values for antigorite serpentinite: $d\ln V_S/d\Theta = -2.59 \times 10^{-3}$ and $d\ln(V_P/V_S)/d\Theta = 0.636 \times 10^{-3}$. Both coefficients were much reduced from their set I counterparts. These partial derivatives are categorized as set II.

[17] Another variable to which velocities are sensitive is temperature. The temperature derivatives are adopted as $d\ln V_S/dT = -1.00 \times 10^{-4}\ ^\circ\mathrm{C}^{-1}$ and $d\ln(V_P/V_S)/dT = 2.3 \times 10^{-6}\ ^\circ\mathrm{C}^{-1}$ [*Lee*, 2003]. All the coefficients are presumably functions of temperature and pressure, but these functions are not known with higher accuracy and we use their constant forms to transform the tomographic models to tectonically more meaningful variables. Conversion of V_S and V_P/V_S to δT and Θ can be done by solving the equation

$$\begin{bmatrix} \dfrac{\partial \ln V_S}{\partial T} & \dfrac{\partial \ln V_S}{\partial \Theta} \\ \dfrac{\partial \ln(V_P/V_S)}{\partial T} & \dfrac{\partial \ln(V_P/V_S)}{\partial \Theta} \end{bmatrix} \begin{bmatrix} \delta T \\ \delta \Theta \end{bmatrix} = \begin{bmatrix} \delta \ln V_S \\ \delta \ln(V_P/V_S) \end{bmatrix}. \quad (2)$$

The formulation of (2) assumes that temperature and serpentinization are two major independent factors that shape the seismic image of the subduction zone-mantle wedge regime. This is an oversimplification, as other factors, such as compositions and the presence of crack or melt also influence the velocities and ratio. Equation (2) can be considered a rotation of the parameter space such that two new parameters are formed by projection from the original two. Because (2) is an exact system, the matrix inversion will map all the errors in $\delta\ln V_S$ and $\delta\ln(V_P/V_S)$ onto δT and $\delta\Theta$.

[18] Figures 4a and 4b show δT and Θ along 121.8°E generated with the set I Θ parameters. As serpentinization only applies to peridotite and the temperature coefficients are typical of shallow upper mantle conditions, our discussion is restricted to the mantle portion of the model (e.g., >40 km). First, temperature accounts for most of the velocity variations related to the Ryukyu slab, and δT basically follow the pattern of V_S. Along the slab, δT falls into the range of −200°C to −400°C (Figure 4a), which is consistent with what simple subduction zone thermal modeling demonstrates in 100–200 km depth range.

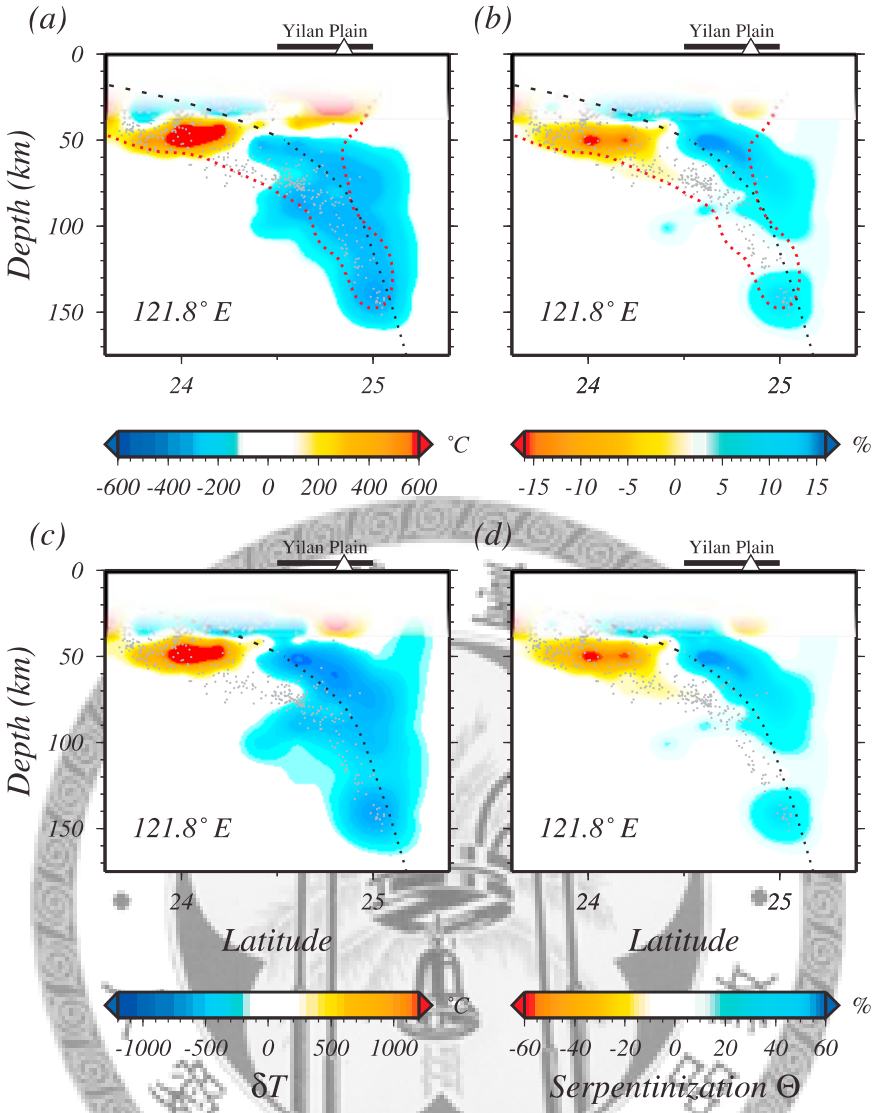

Figure 4. (a) Temperature variation and (b) degree of serpentinization in the mantle determined by equation (2) with set I Θ partial derivatives for 121.8°E. The slab is cooled by 200°C–400°C from the regional mean. The most significant serpentinization zone is in the fore-arc mantle above the slab interface. Models above 40 km depth are not meaningful and are made faded out to the surface. Negative anomalies at the shallow segment of the slab, roughly at 24°N, is unknown in origin. The red thin dotted line is *R*25. (c) Temperature and (d) degree of serpentinization the same as in Figures 4a and 4b, respectively except for set II Θ partials. The temperature minimum on the order of −1000°C in the fore arc is unreasonable.

[19] Serpentinization occurs mainly in the fore-arc mantle adjacent to the slab interface (Figure 4b), and those extending downdip to outside *R*25 are not discussed here. Without the serpentinization parameterization in (2), the fore-arc region with low V_P and V_S would be determined to be warm. Instead, it is now determined to be normal or low temperature. Although only positive Θ makes sense, all signs of Θ were transformed from the right-hand side of (2). An example is the negative Θ at 50 km beneath 24°N (Figure 3). As described above, we are uncertain about the velocity anomalies and therefore reserved about its significance in serpentinization. Strictly, (2) should only be applied to quantify the serpentinization in regions where serpentinization is considered realistic and confidently resolved.

[20] Application of the set II parameters yields different models of temperature and serpentinization (Figures 4c and 4d). Because of the quadruple reduction of the V_P/V_S partial from that in set I, Θ is increased by about fourfold, i.e., to ∼60%, in the fore-arc mantle. The temperature, however, exhibits a strong minimum in the fore-arc mantle where Θ is maximum, instead of within the slab. The extremely cold fore arc may be caused by too high a Θ which entails a V_S too low that requires decreased temperature to compensate for. Judging which set of parameters is correct is beyond the scope of this study, but the set I parameters seem to be preferable in terms of its capability to separate δT and Θ between the slab and the fore-arc mantle in a way consistent with our fundamental knowledge of subduction zones [e.g., *van Keken et al.*,

2002]. These two sets of serpentinization parameters should be tested with other tomographic models.

[21] The serpentinization interpretation for mantle wedge has been invoked elsewhere. In northeast Japan, receiver function images suggest the presence of a long serpentinite layer atop the Pacific slab from 90 to at least 130 km [*Kawakatsu and Watada*, 2007], while in central Japan local, high V_P/V_S are found abutting the surface of the slab at shallow depths [*Kamiya and Kobayashi*, 2000]. Judged from the location of the VF, positive Θ spreads out in the fore arc along the slab interface and reaches a maximum at roughly 50 km depths. This may be linked to the progressive breakdown of hydrous minerals, i.e., lawsonite, chlorite, zoisite, and amphibole in basalt during the basalt-eclogite metamorphic transformation that releases water to hydrate the mantle immediately above it [*van Keken et al.*, 2002; *Iwamori*, 2007]. This is reminiscent of the Cascadia mantle wedge where reflectivity evidence implies strong serpentinization in the fore-arc region at depths 30–50 km [*Bostock et al.*, 2002]. Geological evidence of the fore-arc serpentinization was also found in both oceanic and continental convergent margins [*Fryer et al.*, 1999; *Guillot et al.*, 2000]. In this study, we cannot argue whether serpentinization spreads along the arc because of the decreasing resolution of tomography toward the east.

4.2. Melting

[22] If the temperature is higher than the stability field of the hydrous minerals in serpentinite, serpentinization would not occur in the first place. The free water may facilitate water-fluxed melting at temperatures above water-saturated solidus, or escape upward at lower temperatures. This is an intricate dynamic process, which has been the subject of much numerical modeling effort [e.g., *van Keken et al.*, 2002; *Peacock et al.*, 2005; *Arcay et al.*, 2005]. Beneath NE Japan, low V_P, V_S, and high V_P/V_S anomalies subparallel to the slab in the mantle wedge were interpreted to be a melt signature [e.g., *Zhao et al.*, 2009] with a melt fraction ϕ of 1–2% [*Nakajima et al.*, 2005]. The serpentinized layer later detailed by *Kawakatsu and Watada* [2007] in the same region was localized between the melt zone and the slab. Technically, degree of melting can be estimated by replacing the partial derivatives for Θ with those for ϕ. Examination of the melt model of *Nakajima et al.* [2005] indicates that the signs of the partials of V_S and V_P/V_S with respect to ϕ are consistent with the signs of the partials with respect to Θ, implying that what can be converted to high serpentinization may be converted to a high melt fraction as well.

[23] However, we refrain from addressing the issue of melting based on two observations. First, the melt zone in NE Japan is in the hot core of the wedge beneath the VF and beyond, and is at least 50–100 km horizontally away from the slab interface. In contrast, in NE Taiwan and the westernmost Ryukyu, the well resolved high V_P/V_S signature is adjacent to the slab and at shallower depths localized in the fore arc. Although the mantle wedge here may be warmer near the edge, there are no present-day volcanic activities documented above the fore-arc region. Second, the VF here is small in magnitude compared with the abundant VF activities in NE Japan [*Sibuet et al.*, 1998; *Chung et al.*, 2000; *Tatsumi and Eggins*, 1995; *Tamura et al.*, 2002], implying probably low melt generation at least at present stage. On the other hand, the limited aperture of observation does not allow us to sample northward far into the wedge interior to fully depict the melt distribution. In the present work we attribute the low V_P, V_S, and high V_P/V_S anomaly atop the slab interface to serpentinization of the peridotitic mantle. The pattern and properties of melting in this region may only be defined in the future with a larger-aperture imaging incorporating an OBS array in the OT.

5. Discussion

[24] Unlike in Japan, Alaska, and Cascadia, the JMA part of the combined network provides limited aperture to constrain the mantle wedge north of the subduction zone. Our strategy is to present models that do not overrepresent and inflate what the data can possibly offer. The variance reductions of less than 70% and 60% for V_P and V_S, respectively, are low enough to suppress uncertain, secondary features in the model. We do not interpret anything outside the $R25$ limit, and within the $R25$ limit we are careful in not overinterpreting subtle features whose scale is less than the resolvable scale of heterogeneity. In practice, we are confident more in the profiles in which the subducting Ryukyu slab is resolved better, i.e., showing continuous high V_P and V_S anomalies. Profile 121.8°E is an example, and is the focus of the discussion in this study.

[25] In a recent tomographic effort, *Lin et al.* [2004] obtained a relatively high V_P/V_S channel rising from the slab interface at 40 km depth obliquely to the Yilan plain (with KST 15 km away). The presence of the channel is intriguing by itself, but its signature is weak against the average wedge mantle. With the integrated data sets of CWB and JMA and a carefully calibrated V_P/V_S inversion, we examine whether this feature is robust and worth further elaboration. Note the recoverable scale of heterogeneity is approximately 10 km in this part of the model and the grid spacing is 10 km, which is an adequate parameterization to resolve the melt pathway of *Lin et al.* [2004].

[26] Figure 5 compares the tomographic images of this study and *Lin et al.* [2004] in the same vertical slice shown in the latter. The slab is resolved much better in this study, lending credence to other images. We cannot see any features suggestive of a channel structure connecting the slab and the surface, crossing the corner of the mantle wedge. Throughout all the profiles, no features alike stand out as an obvious anomaly. We also test using different combinations of damping factors for V_P and V_S, i.e., taking models in the neighborhood of the optimums at the two trade-off curves in Figure 2a. One of them is a model with the V_P/V_S norm the same as *Lin et al.* [2004] in the 2-D slice. While the inclined high V_P/V_S layer overlying the slab largely remains, features suggesting a melt pathway claimed by *Lin et al.* [2004] cannot be reproduced. In their study, the primary structure of the Ryukyu slab is poorly resolved in the same profile where the secondary feature of melt is emphasized.

[27] In their most recent work, *Lin et al.* [2007] combined CWB, JMA, and OBS data to constrain the velocity structure in the region similar to that of this study but for the upper 60 km. Their OBS data, recorded over a period of 12 days, may provide additional constraints on the crustal structure of the OT. This advantage, if properly parameterized into the inversion, provides a potential for better imaging the fore arc

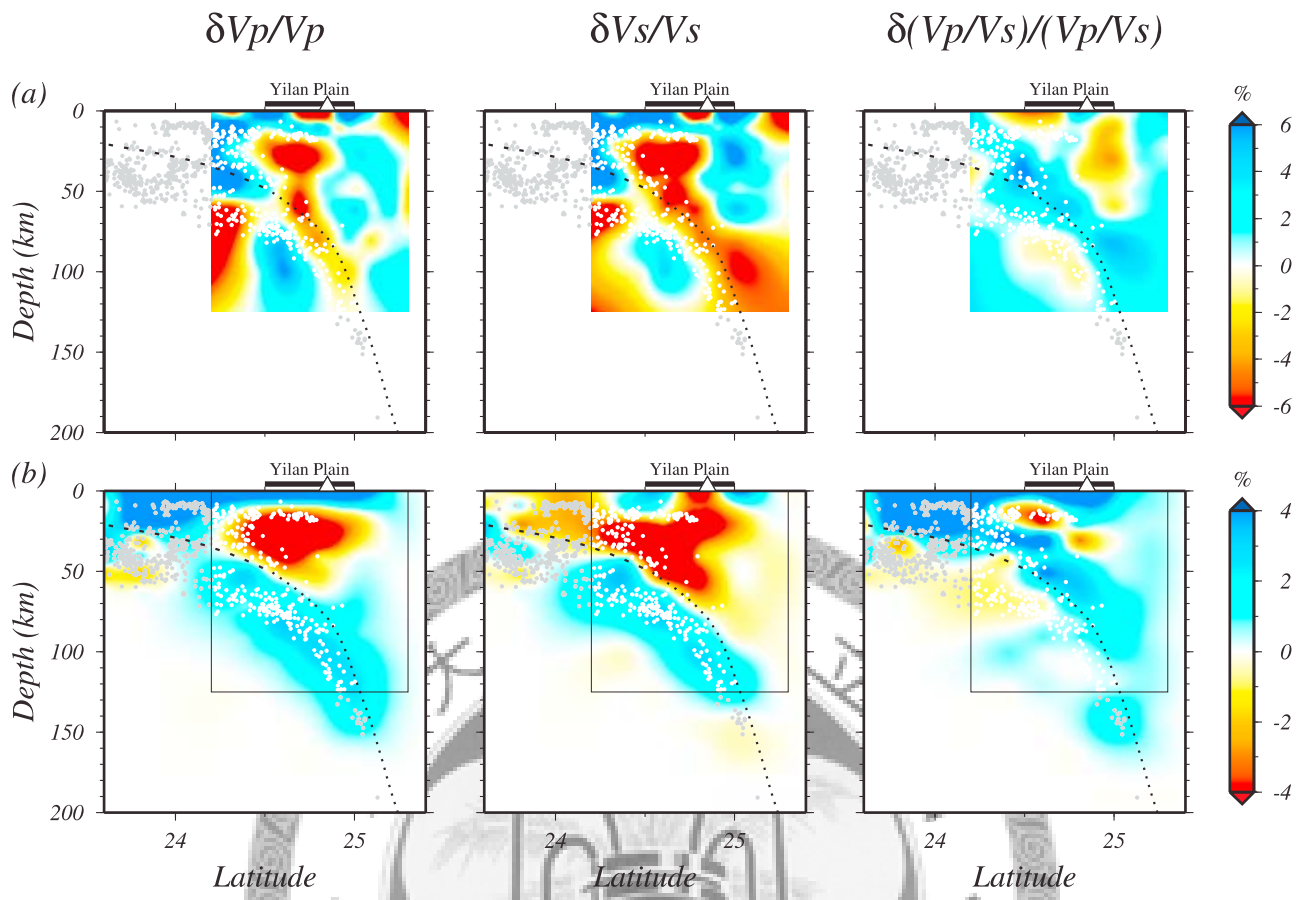

Figure 5. Comparison in V_P, V_S, and V_P/V_S between (a) *Lin et al.* [2004] and (b) this study, along profile 2 of the former. See position of profile in Figure 1. Note the primary feature such as the high V_P/V_S atop the slab is resolved in both studies despite different shapes, while the secondary feature, the weak, positive V_P/V_S anomaly extending obliquely from the slab to the surface in the study by *Lin et al.* [2004] is not resolved in this study. The slab as the most important structure is better expressed in this study than that in the study by *Lin et al.* [2004].

and the slab. *Lin et al.* [2007] reported the presence of more "channels" of melts that feed the VF or the back-arc axis from various parts of the slab along the strike. Yet a comparison between *Lin et al.*'s [2007] study and this study is not straightforward, because their "channels" are highly variable in 3-D and overly subtle, and are very likely beyond the resolution of our model. Here we do not attempt to trace and connect patchy anomalies into a seemingly continuous structure and attach significance to them.

[28] Our model shows that the serpentinization reaches 15% in the fore arc of the westernmost Ryukyu subduction zone. This is comparable to what is estimated from the V_P anomaly alone [*Zhao et al.*, 2001] and less than the local maximum Θ inferred from a reflectivity result [*Bostock et al.*, 2002] both in the Cascadia subduction zone. As serpentinite (Θ = 100) contains 15 wt% water [e.g., *Hacker et al.*, 2003], the maximum water content in the fore-arc mantle may be 2%, and locally the content may be greater because the tomography heavily damps the variations. This amount of bound water may be stable in between the serpentine chlorite dunite field (~6%) and the chlorite harzburgite field (~1.4%) at 50 km depths (~1.5 GPa) and between 500°C and 800°C [*Hacker et al.*, 2003]. As a reference, this temperature range is lower than the water-saturated solidus of peridotite, i.e., 900°C–1000°C at shallow mantle pressures [*Kawamoto and Holloway*, 1997; *Grove et al.*, 2006].

[29] A self-consistent scenario with the serpentinization hypothesis will be that significant water is liberated from basaltic crust at or below 50 km. This will require a temperature range in the oceanic crust which spans the breakdown of hydrous minerals that involve abundant water losses. However, the 500°C–800°C range mostly spans the low water content (<1%) eclogite field at 1.5–2 GPa (~50–65 km) [*Hacker et al.*, 2003]. A reasonable conjecture is that the temperature of the oceanic crust straddles the blueschist/greenschist-eclogite boundary, i.e., 400°C–500°C between 1.5 and 2 GPa [*Hacker et al.*, 2003] so that abundant water (~5%) can be expelled to hydrate the fore-arc mantle. The temperatures may increase from below 400 to above 500°C passing through this depth range. At 50 km or so, water-saturated solidus for basalt is ~650°C [*Lambert and Wyllie*, 1972]. Minor dehydration melting may occur upon zoisite-out reaction at ~700°C–750°C, but it is not until >900°C when amphibole breaks down that the crust melts significantly [*Vielzeuf and Schmidt*, 2001; *Hacker et al.*, 2003]. Although intensive melting seems unlikely, small amount of melting of the oceanic crust cannot be fully rejected.

[30] Geochemical evidence for crust melting in the western Ryukyu subduction zone has not been completely established. High-Mg andesites, considered as an indicator for slab melting, were reported at Iriomote, a previous VF 13 Ma in age now located at the fore arc, but their geochemical signature does not support a subduction zone origin [*Shinjo*, 1999]. However, the recent work on KST (VF) rocks indicated that some of the samples contain high-Mg components, implying some degree of slab melt contribution to the arc volcanoes [*Chu*, 2005]. The issue is still open and developments on this geochemical front should be closely watched. Numerical modeling, geochemical constraints, and seismological imaging need to be integrated to further the understanding of melting in the mantle wedge or slab beneath the westernmost Ryukyu.

[31] Can the fore-arc serpentinization be tested in the future against other observations? Tomography can be improved with OBS deployment in the OT, but the same velocity-based approach likely yields a pattern similar to that in this study. A critical test can be attained from a seismic attenuation tomography. The low attenuation, or high Q value, in the fore-arc mantle beneath Alaska and Cascadia constrained by array waveforms is thought to arise from low temperature, which agrees with the low heat flow measured at the surface [*Schurr et al.*, 2003; *Stachnik et al.*, 2004]. Both Q model and heat flow measurement across the OT are lacking at present and will critically test the serpentinization hypothesis in the future.

6. Conclusion

[32] By integrating CWB and JMA data we construct a tomographic model for the subduction zone and mantle wedge between the NE Taiwan and the westernmost Ryukyu with the best resolution near offshore Taiwan. In light of the relatively unfavorable network coverage, we take a conservative approach toward both regularizing the inversion and interpreting the results. The high V_P and V_S anomalies associated with the subducting Ryukyu slab dominates the tomographic images, while the high V_P/V_S signals above the slab characterize the mantle wedge. The high V_P/V_S channel depicted in a previous tomographic effort and interpreted to be a melt pathway feeding the Yilan plain from the slab cannot be reproduced in this study. The slab signature is consistent with a temperature anomaly of -200°C to -400°C. Significant anomalies of low V_P, V_S and high V_P/V_S appear in the fore arc of the mantle wedge, south of the present-day volcanic front. We interpret this signature as the hydration of mantle peridotites by the water discharged from the basalt-eclogite metamorphism in the subducted oceanic crust, and parameterize it as percentage of serpentinization using laboratory data. Peak serpentinization may reach more than 15%, or 2% water content, in the fore-arc wedge near NE Taiwan. This is a notable departure from previous views which emphasize the role of melts. To achieve a full imaging of the mantle wedge and the melt distribution, expansion of the array with OBSs in the future is critical.

Appendix A

[33] Nonuniform raypath coverage of most regional traveltime tomography studies results in obviously uneven spatial sampling of the velocity perturbations. A conventional approach is to perform restoration experiments on simple synthetic structures such that the spatially varying resolving power of the obtained tomographic model can be appraised.

[34] In addition to the test on V_P/V_S illustrated in Figure 2, we set up a restoration experiment as follow. A synthetic 3D checkerboard model with ±6%, fast and slow alternating velocity anomalies over the grids of our model, i.e., horizontal spacing 0.2° and vertical spacing 10 and 20 km above and below 100 km depth, respectively. As a comparison, a model with a grid spacing doubled is also performed. Traveltime residuals were generated from this model using the raypath sampling identical to the real data. Random errors with zero mean and 0.8 s standard deviation are blended in the synthetic traveltime residuals. Since the geometry of the raypath distribution is the same as in the real inversions, additional trade-off analysis is redundant. That is, we simply adopt the same damping parameters as the ones for the actual inversion (Figure 2a). Errors and damping are essential for conducting a checkerboard test, which are often missed in previous studies. It is clear that our damping parameters efficiently remove potential artifacts from poorly sampled areas at the expense of losing certain marginal resolving power. Figures A1 and A2 show restoration experiments for the two sets of grid spacing. Overall, 10 km resolution diminishes rapidly toward east, while 20 km is maintained better. In the near TW profile, resolvable scale of heterogeneity is 10 km in the crust, 10–20 km in the fore-arc mantle, and probably 20 km in the slab throughout. In the eastern profiles, 20 km variation is in general discernable, except degrading with depth in the slab. The resolution ranges from poor beneath the VF in most of the profiles to none deep in the wedge.

[35] The checkerboard analysis helps to determine the scale of heterogeneity a model can achieve. To quantify how closely to the true value each model parameter is resolved, one needs to establish the resolution matrix, defined as $R = G_g^{-1}G$, where G_g^{-1} is the generalized inverse of the G matrix in the inversion system $Gm = d$. If the system is solved with a singular value decomposition, R can be easily obtained. Usually, nonzeros in R spread over physically neighboring grids, ideally with a maximum value at the center grid. The grid with R value of 1 implies that this parameter is independently resolved and therefore the true model value is recovered, if no errors in data. The diagonal values of the R matrix therefore map out the resolvability at each grid of the tomographic model. In this study the values for the V_P model are used to represent the overall model resolvability. In Figures A1 and A2, most of the region above 50 km in the western end of the model has R values >0.5, where station control is the best. The V_S and V_P/V_S anomalies interpreted to be high serpentinization in the fore arc (Figure 3, 121.8°E profile) straddles the $R \sim 0.5$ contour. The mantle wedge immediately next to the slab and largely above 100 km makes the $R = 0.25$ requirement. We take $R = 0.25$ ($R25$) to be the limit of the resolvable part of the model and the limit of the region within which anomalies are worth an interpretation with caution. Because R is determined by the ray geometry a priori to the inversion, $R25$ should be considered a weak criterion, because structures within this limit could be affected by data errors.

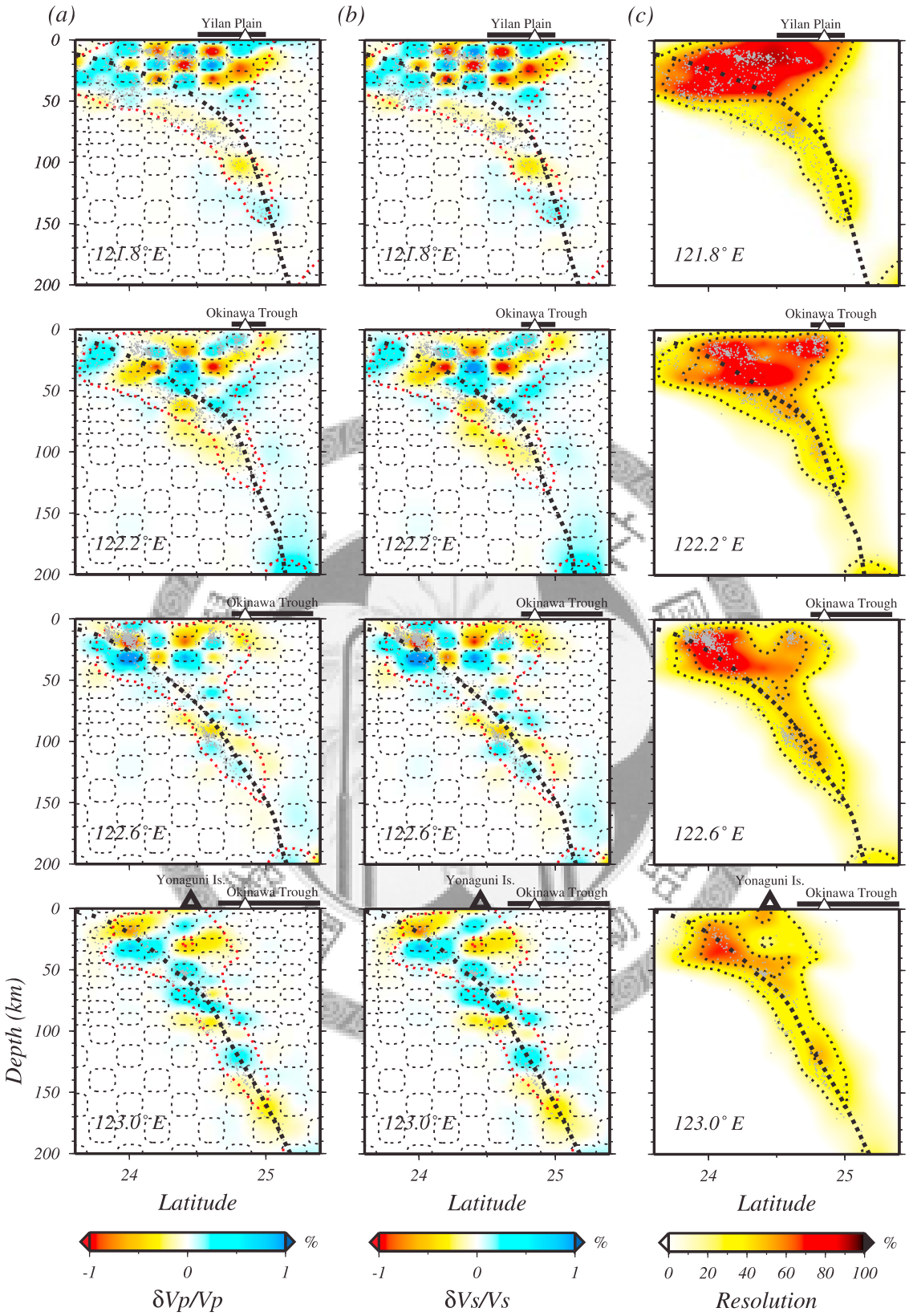

Figure A1. Checkerboard restoration test. (a and b) Velocities and (c) the values of the diagonal terms of the model resolution matrix R for V_P. Above 100 km, grid spacing is 0.2° by 0.2° by 10 km in depth, as outlined by the black dotted lines. Below 100 km, grid spacing is 0.2° by 0.2° by 20 km. The R values are contoured at 25% and 50% (Figure A1c), and the 25% contour is shown in the velocity Figures A1a and A1b ($R25$) as red dotted lines. Note the blurring or shifting of adjacent opposite anomalies in some of the profiles near the margin of the $R25$ region and in profiles to the east.

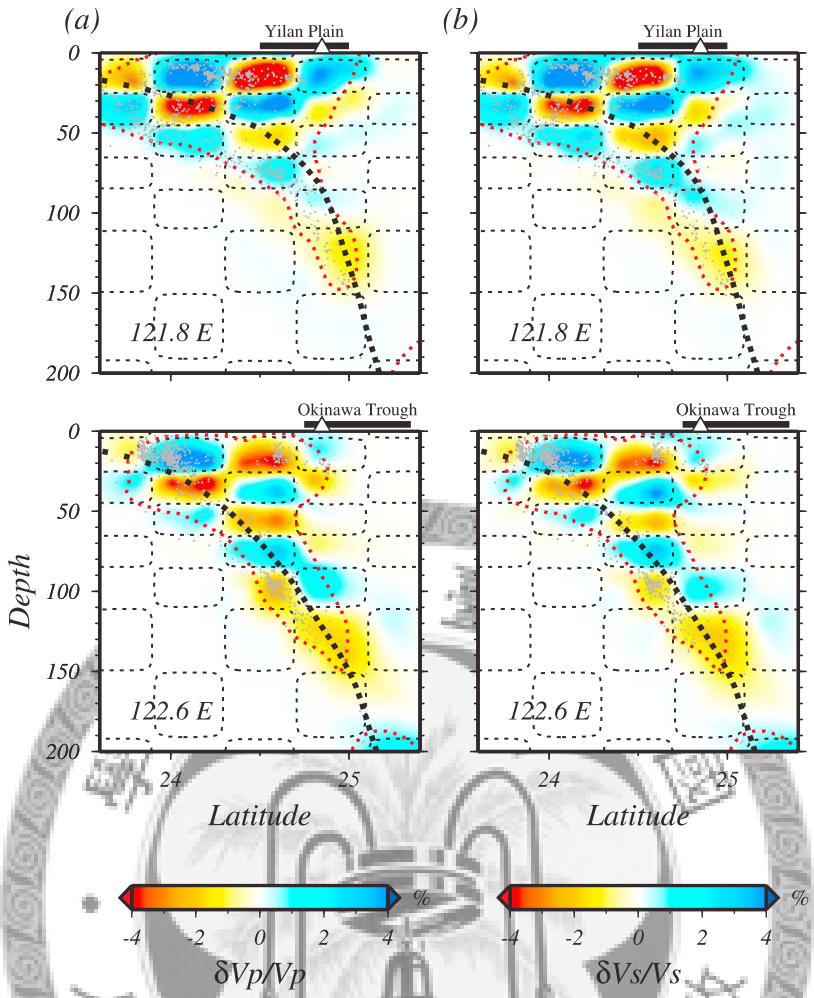

Figure A2. Checkerboard restoration test as in Figure A1 but with grid spacing grids doubled, shown for selected slices (a) for V_P and (b) for V_S. The model has adequate resolving power for this scale of heterogeneity within $R25$ (red dotted lines) in most of the depths and profiles, but the resolution still degrades to the east.

[36] **Acknowledgments.** We are grateful to K. L. Wang, who helped to clarify the geochemical background of this study. Discussions with W. T. Liang, S. L. Chung, and S. R. Song are also appreciated. All graphs were created using the Generic Mapping Tool package [*Wessel and Smith*, 1991]. This study is supported by the National Science Council of Taiwan, under the contract NSC 97-2745-M-001-012.

References

Arcay, D., E. Tric, and M. P. Doin (2005), Numerical simulations of subduction zones: Effects of slab dehydration on the mantle wedge dynamics, *Phys. Earth Planet. Inter.*, *149*, 133–153, doi:10.1016/j.pepi.2004.08.020.

Bostock, M. G., R. D. Hyndman, S. Rondenay, and S. M. Peacock (2002), An inverted continental Moho and serpentinization of the forearc mantle, *Nature*, *417*, 536–538, doi:10.1038/417536a.

Chou, H. C., B. Y. Kuo, S. H. Hung, L. Y. Chiao, D. Zhao, and Y. M. Wu (2006), The Taiwan-Ryukyu subduction-collision complex: Folding of a viscoelastic slab and the double seismic zone, *J. Geophys. Res.*, *111*, B04410, doi:10.1029/2005JB003822.

Christensen, N. I. (1966), Elasticity of ultrabasic rocks, *J. Geophys. Res.*, *71*, 5921–5931.

Christensen, N. I. (2004), Serpentinites, peridotites, and seismology, *Int. Geol. Rev.*, *46*, 795–816, doi:10.2747/0020-6814.46.9.795.

Chu, C. H. (2005), Generation of high-Mg andesites in the Kueishantao volcano, the southernmost part of the Okinawa Trough (in Chinese), Master's thesis, 99 pp., Natl. Taiwan Univ., Taipei.

Chung, S. L., S. L. Wang, R. Shinjo, C. S. Lee, and C. H. Chen (2000), Initiation of arc magmatism in an embryonic continental rifting zone of the southernmost part of Okinawa trough, *Terra Nova*, *12*, 225–230, doi:10.1046/j.1365-3121.2000.00298.x.

Fryer, P., C. G. Wheat, and M. J. Mottl (1999), Mariana blueschist mud volcanism: Implication for conditions within the subduction zone, *Geology*, *27*, 103–106, doi:10.1130/0091-7613(1999)027<0103:MBMVIF>2.3.CO;2.

Graeber, F. M., and G. Asch (1999), Three-dimensional models of P wave velocity and P-to-S velocity ratio in the southern central Andes by simultaneous inversion of local earthquake data, *J. Geophys. Res.*, *104*, 20,237–20,256, doi:10.1029/1999JB900037.

Grove, T. L., N. Ghatterjee, S. W. Parman, and E. Médard (2006), The influence of H_2O on mantle wedge melting, *Earth Planet. Sci. Lett.*, *249*, 74–89, doi:10.1016/j.epsl.2006.06.043.

Guillot, S., K. H. Hattori, and J. de Sigoyer (2000), Mantle wedge serpentinization and exhumation of eclogites: Insights from eastern Ladakh, northwest Himalaya, *Geology*, *28*, 199–202, doi:10.1130/0091-7613(2000)28<199:MWSAEO>2.0.CO;2.

Hacker, B. R., G. A. Abers, and S. M. Peacock (2003), Subduction factory: 1. Theoretical mineralogy, densities, seismic wave speeds, and H_2O contents, *J. Geophys. Res.*, *108*(B1), 2029, doi:10.1029/2001JB001127.

Hattori, K. H., and S. Guillot (2003), Volcanic fronts form as a consequence of serpentinite dehydration in the forearc mantle wedge, *Geology*, *31*, 525–528, doi:10.1130/0091-7613(2003)031<0525:VFFAAC>2.0.CO;2.

Horen, H., M. Zamora, and G. Dubuisson (1996), Seismic wave velocities and anisotropy in serpentinized peridotites form Xigaze ophiolite: Abundance

of serpentine in slow spreading ridge, *Geophys. Res. Lett.*, *23*, 9–12, doi:10.1029/95GL03594.

Hyndman, R. D., and S. M. Peacock (2003), Serpentinization of the forearc mantle, *Earth Planet. Sci. Lett.*, *212*, 417–432, doi:10.1016/S0012-821X(03)00263-2.

Iwamori, H. (2007), Transportation of H_2O beneath the Japan arcs and its implications for global water circulation, *Chem. Geol.*, *239*, 182–198, doi:10.1016/j.chemgeo.2006.08.011.

Kamiya, S., and Y. Kobayashi (2000), Seismological evidence for the existence of serpentinized wedge mantle, *Geophys. Res. Lett.*, *27*, 819–822, doi:10.1029/1999GL011080.

Kao, H., S.-J. Shen, and K.-F. Ma (1998), Transition from oblique subduction to collision: Earthquakes in the southernmost Ryukyu arc-Taiwan region, *J. Geophys. Res.*, *103*, 7211–7229, doi:10.1029/97JB03510.

Kawakatsu, H., and S. Watada (2007), Seismic evidence for deep-water transportation in the mantle, *Science*, *316*, 1468–1471, doi:10.1126/science.1140855.

Kawamoto, T., and J. R. Holloway (1997), Melting temperature and partial melt chemistry of H_2O-saturated mantle peridotite to 11 gigapascal, *Science*, *276*, 240–243, doi:10.1126/science.276.5310.240.

Lambert, I. R., and P. J. Wyllie (1972), Melting of gabbro (quartz eclogite) with excess water to 35 kilobars, with geological applications, *J. Geol.*, *80*, 693–708, doi:10.1086/627795.

Lee, C. S., G. J. Shor, L. D. Bibee, R. S. Lu, and T. W. C. Hilde (1980), Okinawa trough: Origin of a back-arc basin, *Mar. Geol.*, *35*, 219–241, doi:10.1016/0025-3227(80)90032-8.

Lee, C. T. A. (2003), Compositional variation of density and seismic velocities in natural peridotites at STP conditions: Implications for seismic imaging of compositional heterogeneities in the upper mantle, *J. Geophys. Res.*, *108*(B9), 2441, doi:10.1029/2003JB002413.

Lin, J. Y., S. K. Hsu, and J. C. Sibuet (2004), Melting features along the western Ryukyu slab edge (northeast Taiwan): Tomographic evidence, *J. Geophys. Res.*, *109*, B12402, doi:10.1029/2004JB003260.

Lin, J. Y., J. C. Sibuet, C. S. Lee, S. K. Hsu, and F. Klingelhoefer (2007), Origin of the southern Okinawa trough volcanism from detailed seismic tomography, *J. Geophys. Res.*, *112*, B08308, doi:10.1029/2006JB004703.

Nakajima, J., Y. Takei, and A. Hasagawa (2005), Quantitative analysis of the inclined low-velocity zone in the mantle wedge of northeastern Japan: A systematic change of melt-filled pore shapes with depth and its implications for melt migration, *Earth Planet. Sci. Lett.*, *234*, 59–70, doi:10.1016/j.epsl.2005.02.033.

Pavlis, G. L., and J. R. Booker (1980), The mixed discrete-continuous inverse problem; application to the simultaneous determination of earthquake hypocenters and velocity structure, *J. Geophys. Res.*, *85*, 4801–4810, doi:10.1029/JB085iB09p04801.

Peacock, S. M., P. E. van Keken, S. D. Holloway, B. R. Hacker, G. A. Abers, and R. L. Rergason (2005), Thermal structure of the Costa Rica-Nicaragua subduction zone, *Phys. Earth Planet. Inter.*, *149*, 187–200, doi:10.1016/j.pepi.2004.08.030.

Rau, R. J., and F. T. Wu (1995), Tomographic imaging of lithospheric structure under Taiwan, *Earth Planet. Sci. Lett.*, *133*, 517–532, doi:10.1016/0012-821X(95)00076-O.

Schmidt, M. W., and S. Poli (1998), Experimentally based water budgets for dehydrating slabs and consequences for arc magma generation, *Earth Planet. Sci. Lett.*, *163*, 361–379, doi:10.1016/S0012-821X(98)00142-3.

Schurr, B., G. Asch, A. Rietbrock, R. Trumbull, and C. Haberland (2003), Complex patterns of fluid and melt transport in the central Andean subduction zone revealed by attenuation tomography, *Earth Planet. Sci. Lett.*, *215*, 105–119, doi:10.1016/S0012-821X(03)00441-2.

Shinjo, R. (1999), Geochemistry of high Mg andesites and the tectonic evolution of the Okinawa Trough-Ryukyu arc system, *Chem. Geol.*, *157*, 69–88, doi:10.1016/S0009-2541(98)00199-5.

Sibuet, J.-C., et al. (1987), Back-arc extension in the Okinawa trough, *J. Geophys. Res.*, *92*, 14,041–14,063, doi:10.1029/JB092iB13p14041.

Sibuet, J.-C., B. Deffontaines, S. Hsu, N. Thareau, J. Le Formal, C. Liu, and the ACT Party (1998), Okinawa trough backarc basin: Early tectonic and magmatic evolution, *J. Geophys. Res.*, *103*, 30,245–30,267.

Stachnik, J. C., G. A. Abers, and D. H. Christensen (2004), Seismic attenuation and mantle wedge temperatures in the Alaska subduction zone, *J. Geophys. Res.*, *109*, B10304, doi:10.1029/2004JB003018.

Tamura, Y., Y. Tatsumi, D. Zhao, Y. Kido, and H. Shunkuno (2002), Hot fingers in the mantle wedge: New insights into magma genesis in subduction zones, *Earth Planet. Sci. Lett.*, *197*, 105–116, doi:10.1016/S0012-821X(02)00465-X.

Tatsumi, Y., and S. Eggins (1995), Subduction Zone Magmatism, 211 pp., Blackwell, Cambridge, U. K.

Teng, L. (1990), Geotectonic evolution of late Cenozoic arc-continent collision in Taiwan, *Tectonophysics*, *183*, 57–76, doi:10.1016/0040-1951(90)90188-E.

van Keken, P. E., B. Kiefer, and S. M. Peacock (2002), High-resolution models of subduction zones: Implications for mineral dehydration reactions and the transport of water into the deep mantle, *Geochem. Geophys. Geosyst.*, *3*(10), 1056, doi:10.1029/2001GC000256.

Vielzeuf, D., and M. W. Schmidt (2001), Melting relations in hydrous systems revisited: Application to metapelites, metagreywackes and metabasalts, *Contrib. Mineral. Petrol.*, *141*, 251–267.

Walck, M. (1988), Three-dimensional V_P/V_S variations for the Coso region, California, *J. Geophys. Res.*, *93*, 2047–2052, doi:10.1029/JB093iB03p02047.

Waldhauser, F., and W. L. Ellsworth (2000), A double-difference earthquake location algorithm: Method and application to the northern Hayward fault, *Bull. Seismol. Soc. Am.*, *90*, 1353–1368, doi:10.1785/0120000006.

Wessel, J. K., and H. F. Smith (1991), Free software helps map and display data, *Eos Trans. AGU*, *72*, 445–446, 441, doi:10.1029/90EO00319.

Yeh, Y. H., C. H. Lin, and S. W. Roecker (1989), A study of upper crustal structures beneath northeastern Taiwan: Possible evidence of the western extension of Okinawa trough, *Proc. Geol. Soc. China*, *32*, 139–156.

Zhao, D., A. Hasegawa, and S. Horiuchi (1992), Tomographic imaging of P and S wave velocity structure beneath northeastern Japan, *J. Geophys. Res.*, *97*, 19,909–19,928, doi:10.1029/92JB00603.

Zhao, D., K. Wang, G. C. Rogers, and S. M. Peacock (2001), Tomographic image of low P velocity anomalies above slab in northern Cascadia subduction zone, *Earth Planets Space*, *53*, 285–293.

Zhao, D., Z. Wang, N. Umino, and A. Hasegawa (2009), Mapping the mantle wedge and interplate thrust zone of the northeast Japan arc, *Tectonophysics*, *467*, 89–106, doi:10.1016/j.tecto.2008.12.017.

L.-Y. Chiao, Institute of Oceanography, National Taiwan University, P.O. Box 23-13, Taipei 10617, Taiwan.

H.-C. Chou and S.-H. Hung, Institute of Geosciences, National Taiwan University, No. 1, Sec. 4, Roosevelt Rd., Taipei 10617, Taiwan.

B.-Y. Kuo, Institute of Earth Sciences, Academia Sinica, 128 Academia Rd., Sec. 2, Taipei 11529, Taiwan. (byk@earth.sinica.edu.tw)

D. Zhao, Department of Geophysics, Tohoku University, 6-6 Aoba, Aramaki, Aoba-ku, Sendai 980-8578, Japan.